## Repository Istituzionale dei Prodotti della Ricerca del Politecnico di Bari

Waste valorization for sustainable advanced materials and catalysts

(Article begins on next page)

23 January 2025

# LIBERATORIA PER L'ARCHIVIAZIONE DELLA TESI DI DOTTORATO

Al Magnifico Rettore
del Politecnico di Bari

La sottoscritta Darya Nefedova nata a Taldykorgan, Kazakhstan il 13/06/1994 residente a Bari (BA) 70121 in via Michelangelo Signorile 2B e-mail darya.nefedova@poliba.it iscritto al 3° anno di Corso di Dottorato di Ricerca in RISCHIO, SVILUPPO AMBIENTALE, TERRITORIALE ED EDILIZIO ciclo XXXVII ed essendo stato ammesso a sostenere l'esame finale con la prevista discussione della tesi dal titolo: Waste Valorization for Sustainable Advanced Materials and Catalysts

## DICHIARA

1) di essere consapevole che, ai sensi del D.P.R. n. 445 del 28.12.2000, le dichiarazioni mendaci, la falsità negli atti e l'uso di atti falsi sono puniti ai sensi del codice penale e delle Leggi speciali in materia, e che nel caso ricorressero dette ipotesi, decade fin dall'inizio e senza necessità di nessuna formalità dai benefici conseguenti al provvedimento emanato sulla base di tali dichiarazioni;
2) di essere iscritto al Corso di Dottorato di ricerca RISCHIO, SVILUPPO AMBIENTALE, TERRITORIALE ED EDILIZIO ciclo XXXVII, corso attivato ai sensi del *"Regolamento dei Corsi di Dottorato di ricerca del Politecnico di Bari"*, emanato con D.R. n.286 del 01.07.2013;
3) di essere pienamente a conoscenza delle disposizioni contenute nel predetto Regolamento in merito alla procedura di deposito, pubblicazione e autoarchiviazione della tesi di dottorato nell'Archivio Istituzionale ad accesso aperto alla letteratura scientifica;
4) di essere consapevole che attraverso l'autoarchiviazione delle tesi nell'Archivio Istituzionale ad accesso aperto alla letteratura scientifica del Politecnico di Bari (IRIS-POLIBA), l'Ateneo archivierà e renderà consultabile in rete (nel rispetto della Policy di Ateneo di cui al D.R. 642 del 13.11.2015) il testo completo della tesi di dottorato, fatta salva la possibilità di sottoscrizione di apposite licenze per le relative condizioni di utilizzo (di cui al sito http://www.creativecommons.it/Licenze), e fatte salve, altresì, le eventuali esigenze di "embargo", legate a strette considerazioni sulla tutelabilità e sfruttamento industriale/commerciale dei contenuti della tesi, da rappresentarsi mediante compilazione e sottoscrizione del modulo in calce (Richiesta di embargo);
5) che la tesi da depositare in IRIS-POLIBA, in formato digitale (PDF/A) sarà del tutto identica a quelle **consegnate**/inviate/da inviarsi ai componenti della commissione per l'esame finale e a qualsiasi altra copia depositata presso gli Uffici del Politecnico di Bari in forma cartacea o digitale, ovvero a quella da discutere in sede di esame finale, a quella da depositare, a cura dell'Ateneo, presso le Biblioteche Nazionali Centrali di Roma e Firenze e presso tutti gli Uffici competenti per legge al momento del deposito stesso, e che di conseguenza va esclusa qualsiasi responsabilità del Politecnico di Bari per quanto riguarda eventuali errori, imprecisioni o omissioni nei contenuti della tesi;
6) che il contenuto e l'organizzazione della tesi è opera originale realizzata dal sottoscritto e non compromette in alcun modo i diritti di terzi, ivi compresi quelli relativi alla sicurezza dei dati personali; che pertanto il Politecnico di Bari ed i suoi funzionari sono in ogni caso esenti da responsabilità di qualsivoglia natura: civile, amministrativa e penale e saranno dal sottoscritto tenuti indenni da qualsiasi richiesta o rivendicazione da parte di terzi;
7) che il contenuto della tesi non infrange in alcun modo il diritto d'Autore né gli obblighi connessi alla salvaguardia di diritti morali od economici di altri autori o di altri aventi diritto, sia per testi, immagini, foto, tabelle, o altre parti di cui la tesi è composta.

Luogo e data   Bari 13/01/2025          Firma _____

La sottoscritto, con l'autoarchiviazione della propria tesi di dottorato nell'Archivio Istituzionale ad accesso aperto del Politecnico di Bari (POLIBA-IRIS), pur mantenendo su di essa tutti i diritti d'autore, morali ed economici, ai sensi della normativa vigente (Legge 633/1941 e ss.mm.ii.),

## CONCEDE

- al Politecnico di Bari il permesso di trasferire l'opera su qualsiasi supporto e di convertirla in qualsiasi formato al fine di una corretta conservazione nel tempo. Il Politecnico di Bari garantisce che non verrà effettuata alcuna modifica al contenuto e alla struttura dell'opera.
- al Politecnico di Bari la possibilità di riprodurre l'opera in più di una copia per fini di sicurezza, back-up e conservazione.

Luogo e data   Bari 13/01/2025          Firma _____

# D.R.S.A.T.E.

Doctor in Risk And Environmental, Territorial And Building Development

**POLITECNICO DI BARI**

**05**

2024

Coordinator: Prof. Vito Iacobellis

XXXVII CYCLE
Curriculum: CHEM-06/A

DICATECh
Department of Civil, Environmental,
Building Engineering and Chemistry

Darya Nefedova

## Waste Valorization for Sustainable Advanced Materials and Catalysts

Prof.ssa Maria Michela Dell'Anna

Department of Civil, Environmental, Building Engineering
and Chemistry DICATECh
Politecnico di Bari

Dott.ssa Matilda Mali

Department of Civil, Environmental, Building Engineering
and Chemistry DICATECh
Politecnico di Bari

Prof. Giuseppe Romanazzi

Department of Civil, Environmental, Building Engineering
and Chemistry DICATECh
Politecnico di Bari

Истина открывается в тиши тем, кто её разыскивает

Д.И. Менделеев

# EXTENDED ABSTRACT

The process of waste valorization, which involves converting trash materials into valuable resources, is particularly relevant in today's world, given the pressing environmental and economic challenges. Current research focuses on the valorization of diverse waste streams: steel slags from metallurgical production, cigarette butts, and invasive tunicates from aquaculture for producing cellulose.

Steel slags were utilized as support for copper and iron oxide catalysts, thanks to their alkaline features. The Cu/Steel Slags catalysts showed high activity in the reduction of nitroarenes in water in the presence of sodium borohydride as the reducing agent at room temperature. The FeOx/Steel Slags catalysts were employed in the catalytic transfer hydrogenation of nitrobenzene in the presence of isopropanol as the hydrogen source, without adding any external base, such as potassium or sodium hydroxide.

Concerning the valorization of cigarette butts, cellulose acetate was successfully recovered from them using inexpensive and sustainable solvents, such as water, NaCl solution and ethanol. An optimized purification protocol was developed, yielding high-purity cellulose acetate suitable for reuse in polymer applications.

Furthermore, in the framework of invasive tunicate valorization, an innovative and sustainable protocol for efficient extraction of cellulose from them was developed. The species under study, Clavelina oblonga, was subjected to acidic deep eutectic solvent (DES) treatment by using choline chloride and oxalic acid in 1:1 molar ratio under microwave irradiation obtaining purified cellulose having proprieties comparable to those observed by using conventional extractive procedures based on toxic and expensive reagents.

*Waste valorization, steel slags, catalysts, cellulose acetate, tunicates*

# INDEX

# SUMMARY

Nowadays, the accumulation of waste has reached unprecedented levels, giving rise to significant environmental, social and economic concerns. Waste valorization, as a crucial process in sustainable development, is gaining increasing attention as a solution to the mounting challenges associated with waste generation and resource depletion. This process transforms waste into valuable resources such as energy, chemicals or alternative materials, thereby minimizing environmental impacts and promoting a circular economy.

The **aim of the present work** is the valorization of three different kinds of wastes: industrial **steel slags**, municipal **cigarette butts** and natural wastes of **tunicates** to obtain valuable advanced materials and catalysts.

The first chapter provides an analytical review of the literature on waste valorization and a general characterization of wastes. Different types of wastes such as industrial (steel slag), municipal (cigarette butts) and natural (tunicates) trashes were considered as promising for valorization process to produce valuable recycled products. In particular, the use of steel slag as a catalyst is reviewed. Existing methods for the recovery of cellulose acetate from cigarette butts are also presented. In addition, methods for obtaining high quality nanocrystalline cellulose from invasive tunicate species are discussed.

Chapter 2 presents the study of steel slags, an industrial by-products of steel production. The study focuses on the characterization of the chemical and physical properties of steel slags in order to evaluate their potential as catalyst support material. Copper and iron oxide steel slag-based catalysts were synthesized by minimizing the reagents used. Characterization techniques such as X-ray diffraction (XRD), Fourier transform infrared spectroscopy (FT-IR) and scanning electron microscopy (SEM) were used to elucidate the elemental composition, phase structure and surface morphology of obtaining catalyst. The resulting steel slag-based catalysts were tested in the hydrogenation of nitroarenes, demonstrating the catalytic activity of steel slag, which can serve as an effective and sustainable alternative to traditional catalyst supports.

The third chapter is devoted to the development of cost-effective and green purification methods for recovering cellulose acetate from cigarette filters. Considering the toxicity of cigarette filters, the chapter highlights the potential of cellulose acetate recovery as a resource for materials applications. A multi-stage extraction and purification protocol using deionized water, sodium chloride (NaCl) and ethanol solutions were developed to systematically remove organic and inorganic contaminants. Characterization techniques, such as FT-IR and TGA, were used to verify the quality and purity of the recovered cellulose acetate. The study evaluated the effectiveness of different solvents and purification parameters to optimize cellulose acetate recovery.

Chapter 4 explores the extraction of cellulose from the invasive marine obsidians *Clavelina oblonga*, a unique animal source of nanocrystalline cellulose. Cellulose from tunicates is positioned as a promising material with superior properties for high performance applications, while addressing the environmental challenges posed by invasive tunicates species. The extraction method was based on the use of deep eutectic solvents (DES), an environmentally friendly alternative to conventional extraction methods. This chapter compares DES-based extraction with traditional alkaline and bleaching methods.

The final chapter 5 outlines the experimental protocols used in the synthesis, purification, and testing of the materials and catalysts discussed in previous chapters.

# 1. STATE OF THE ART

## *1.1. Circular economy and waste valorization*

The circular economy concept emerged and gained popularity in the late 1970s as a departure from the traditional linear economic model of "take, make, waste"[1]. Various authors have defined the circular economy. For example, the Ellen MacArthur Foundation described it as "an industrial economy that is restorative or regenerative by intention and design"[2], while Geng and Doberstein[3], focusing on the Chinese implementation, characterized it as the "realization of a closed-loop material flow in the entire economic system." Nevertheless, the current model aims to decouple economic growth from the consumption of finite resources, minimizing waste and maximizing resource efficiency through a closed-loop approach as depicted in Fig. 1.1. This involves three key principles: eliminating waste and pollution, keeping products and materials in use, and restoring natural systems[4]. Among all principles, the United Nations Economic Commission for Europe (UNECE) highlights waste valorization as a key factor in advancing the circular economy[5].



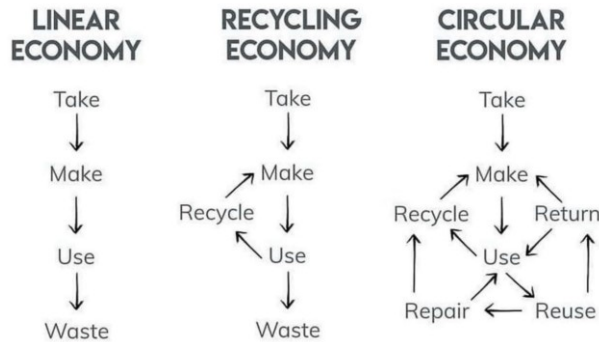Fig. 1.1 Schematic representation of different economies types

**Waste valorization** has gained prominence as an alternative to waste disposal and landfill, offering the potential to transform traditionally discarded waste into useful materials, energy, or products[6]. Waste valorization can be divided into **three main categories**, which represent different approaches to converting waste into valuable resources.

3

**Material recovery** is the extraction, reuse and recycling of materials from waste. It is the most direct form of waste valorization, where discarded materials are processed by mechanical processes and returned to the production cycle, thus avoiding the need for virgin raw materials. Material recovery focuses on the reuse of valuable components such as metals, plastics, paper and textiles [7]. As example, Barragan et. all successfully recovered high-purity copper from electronic waste through a combination of mechanical shredding and chemical leaching with a recovery rate of 96%, contributing to the efficient recycling of valuable metals from e-waste [8].

**Chemical valorization** refers to the conversion of waste materials into valuable chemicals or bio-based products through chemical reactions. This process is particularly useful for organic waste, plastic waste and other complex materials that are not easily recycled by mechanical processes. Chemical valorization often involves techniques such as pyrolysis, gasification and fermentation, which break down waste materials into simpler compounds that can be used as feedstocks for industrial processes or energy generation.

**Energy recovery** is the process of converting waste materials into energy, typically in the form of electricity, heat or biofuels. This category is particularly important for waste streams that cannot be easily recycled or valorized into materials or chemicals. Energy recovery technologies aim to extract the energy contained in waste materials, which would otherwise be lost, and return it to productive use [9].

However, despite its relevance and potential applications, the implementation of waste valorization is constrained by several obstacles. The implementation of an effective valorization system requires substantial investment in infrastructure, including the installation of sorting lines, processing plants, and logistics chains. Additionally, the prices of secondary raw materials can fluctuate, creating risks for investors and complicating long-term planning. Moreover, the production of products from virgin raw materials often remains more economically viable than from secondary raw materials due to established processing chains, readily available virgin resources, and higher quality. Effective waste valorization necessitates careful sorting aiming at separating different materials, which is challenging and costly, particularly in the presence of contaminants

and composites. It is not always possible to process all waste streams effectively using existing technologies. Overcoming these barriers requires a comprehensive approach, including the introduction of economic incentives, technological advancements, a strengthened legislative framework, and the promotion of circular economy principles.

One of the most important initiatives in waste management is the Waste Framework Directive (Directive 2008/98/EC)[10], which serves as the fundamental legal instrument governing waste management in the European Union. This directive establishes essential definitions such as waste, recycling and recovery, as well as defining basic principles designed to mitigate the negative impacts of waste generation and disposal on human health and the environment. The Waste Framework Directive (WFD) is based on the promotion of the circular economy paradigm, which views waste not simply as a by-product of consumption, but as a potential resource to be reintegrated into the production cycle.



Fig. 1.2 Waste management hierarchy in Waste Framework Directive [10]

The directive (Fig. 1.2) introduces the waste hierarchy, a system of priorities that includes waste prevention, followed by preparation for reuse, recycling, other recovery methods (e.g. energy recovery) and, only as a last resort, disposal. This hierarchical approach is designed to encourage waste reduction at the outset and improve resource efficiency.

## 1.2.    Steel slags

Steel slag is a complex by-product solution of silicates and oxides generated during the steelmaking process when impurities are separated during melting process of raw materials like iron ore, coke, and limestone in furnaces. During this process, impurities such as silica, alumina, and other oxides combine with fluxes to form slag, which floats on the surface of the molten steel and can be removed.

### 1.2.1 Classification of Steel slags

The chemical and physical properties of steel slag vary significantly depending on the specific steelmaking technology employed. These variations arise from the inherent differences in each process, resulting in types of steel slag with unique properties and corresponding applications. Steel slag can therefore be classified into 3 main categories (Fig.1.3): Basic Oxygen Furnace Slag (BOF), Electric Arc Furnace Slag (EAF) and Ladle Furnace Slag (LFS), each with its own characteristic composition and applications.
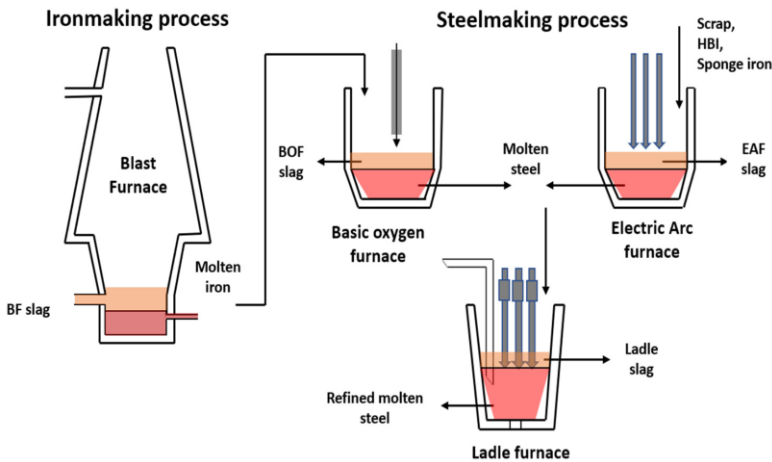


Fig. 1.3 Generation of various slags from the steel industry[11]

**Basic Oxygen Furnace (BOF) Slag** is produced during the primary steelmaking process where oxygen is blown into molten iron in the basic oxygen furnace to reduce carbon content and remove impurities. This type of slag is typically dense and highly alkaline, containing a large amount of calcium oxide (CaO) (Table 1.1). In addition, BOF slag generally contains significant amounts of iron oxides (FeO, $Fe_2O_3$) and silicon

dioxide ($SiO_2$), and less amounts of manganese, phosphorus, and sulphur compounds. The high compressive strength of BOF slag making it suitable for use in road construction, as an aggregate in asphalt and concrete, and in soil stabilization.

**Electric Arc Furnace (EAF) Slag** is generated during the steelmaking process in electric arc furnaces, where scrap steel is melted using electrical energy. This type of slag is more variable in composition, depending on the types of scrap used. EAF Slag is subdivided into 2 different categories: EAFC: (Electric Arc Furnace Slag from Carbon Steel production) and EAFS: (Electric Arc Furnace Slag from Stainless Steel production). EAF slag typically has a lower iron content than BOF slag but is still rich in calcium oxide and silicates, making it an excellent construction material, particularly in road bases and asphalt mixtures. Also it often contains higher levels of aluminum oxides ($Al_2O_3$) and magnesium oxides (MgO), which enhance its durability. Depending on the intended steel quality (carbon steel or stainless/high alloy steel)

**Ladle Furnace Slag (LFS)** is a by-product of the secondary steel refining process, where molten steel is further treated in a ladle furnace to adjust its chemical composition, removing impurities like sulphur and adjusting the alloy content. Ladle furnace slag tends to be more fine grained and contains higher levels of alumina ($Al_2O_3$), magnesium oxide (MgO), and calcium fluoride ($CaF_2$), which is used as a flux in this refining step. Due to its finer particle size and different mineralogy, LFS is often utilized in cement manufacturing as a raw material or clinker substitute. However, it is less frequently used in structural applications compared to BOF or EAF slag due to its higher flux content.

Table 1.1. Chemical Composition Range of Steel Slags[12]

| Components | Basic oxygen furnace | Electric arc furnace (carbon steel) | Electric arc furnace (alloy/stainless) | Ladle |
|---|---|---|---|---|
| $SiO_2$ | 8–20 | 9–20 | 24–32 | 2–35 |
| $Al_2O_3$ | 1–6 | 2–9 | 3.0–7.5 | 3–15 |
| FeO | 10–35 | 15–30 | 1–6 | 0.1–15 |
| CaO | 30–55 | 35–60 | 39–45 | 30–60 |
| MgO | 5–15 | 5–15 | 8–15 | 1–10 |
| MnO | 2–8 | 3–8 | 0.4–2 | 0–5 |
| $TiO_2$ | 0.4–2 | N/A* | N/A* | N/A* |
| S | 0.05–0.15 | 0.08–0.2 | 0.1–0.3 | 0.1–1 |
| P | 0.2–2 | 0.01–0.25 | 0.01–0.07 | 0.1–0.4 |
| Cr | 0.1–0.5 | 0.1–1 | 0.1–20 | 0–0.5 |

*Not available

The percentage of slag production is directly influenced by the steelmaking process. The average slag generation amounts to 110 kg/ton of steel for the Basic Oxygen Furnace (BOF), 70 kg/ton for the Electric Arc Furnace (EAF), and 40 kg/ton for the Ladle Furnace (LFS) processes [13]. Despite generating significantly more slag waste (>52% of the total), the BOF remains a prevalent steel production method in Europe (see Fig.1.4)



BOF
[52.3%]

EAF
(Carbon Steel)
[26.2%]

Others
[12.6%]

EAF
(High Alloy)
[8.9%]

Production of steel slag in 2018: 21.4 mililon tonnes
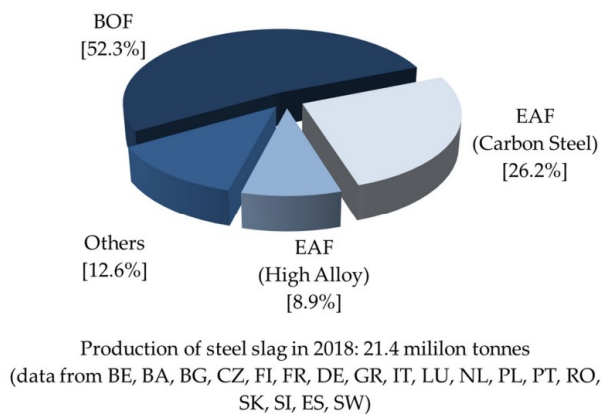(data from BE, BA, BG, CZ, FI, FR, DE, GR, IT, LU, NL, PL, PT, RO, SK, SI, ES, SW)

Fig. 1.4 Steel slag type distribution in European countries in 2018 [14]

## 1.2.2 Application of Steel Slags waste material

Recent study of Chandel et al. [13] shows that most of the steel slag finds its application in various fields (Fig.1.5). Approximately 48% of all slag is utilized in road construction, while 15% is used for internal storage. Other applications include cement production (6%), metal production (8%), and fertilizer (3%). A small percentage (1%) is employed in hydraulic engineering, and the remaining 6% is used for diverse purposes. However, a substantial portion of steel slag remains in internal storage (15%) and is ultimately destined for final disposal (13%).
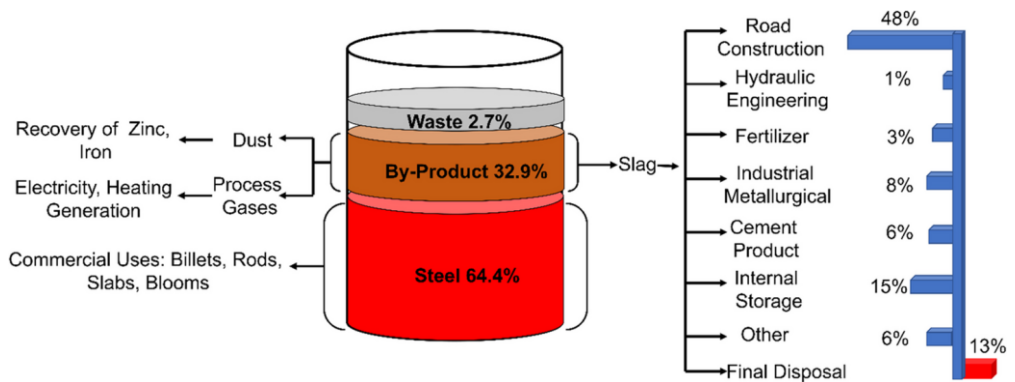


Fig.1.5 Schematic representation of steel and steel slag application in various sectors [13]

Despite its potential applications, steel slag poses significant environmental hazards if not managed responsibly (Fig.1.6). The primary negative impact stems from the leaching of heavy metals like chromium, lead, and zinc into soil and water, contaminating ecosystems and potentially entering the food chain, affecting both wildlife and human health[15]. Furthermore, steel slags are highly alkaline due to their high content of CaO and MgO. When leached into the groundwater, they can increase the pH value of the groundwater up to 10.4-11.8, increasing the levels of calcium, chromium, and fluoride [16]. Additionally, dust generated during the handling and processing of steel slag can contain harmful substances, contributing to air pollution.
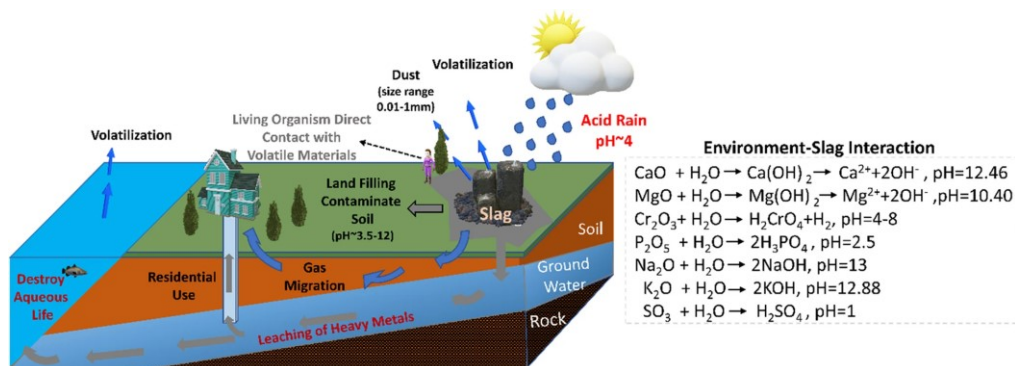
Fig.1.6 Schematic illustration of of landfilled steel slag effect on the environment, possible reaction and corresponding pH values [13]

### 1.2.3 Catalytical application of Steel Slags

Recent studies have demonstrated the significant potential of steel slag in catalysis, particularly after undergoing various modifications. Wang et al. [17] arranged these modifications into five categories: Acid modification, Alkali modification, High Temperature Activation Modification, Compound modification, and Physical modification. A detailed breakdown of this classification follows:

Acid modification involves the chemical reaction of steel slag with an acidic solution, resulting in the release of soluble salts. This process alters the structure of the steel slag, increasing its specific surface area and pore size, thereby enhancing the contact surface between the steel slag and the reactant, ultimately improving its catalytic performance.

Large amounts of CaO in the steel slag composition inhibit nucleation of the crystalline phase [17]. The addition of an alkali modifier can counteract the inhibitory effect owing to the formation of substances that are insoluble or slightly soluble in $Ca(OH)_2$, increasing the specific surface area, pore size, and number of catalytic active sites in the steel slag.

High-temperature activation modification involves heating the steel slag to elevated temperatures, which can decompose active components, producing finer and more catalytically active transition metal oxide grains. Thereby, this process can alter the crystal structure of the slag and modify its surface properties.

Compound modification involves mixing one or more materials with steel slag in specific proportions, followed by additional modification treatments.

Physical modification involves mechanical activation to grind steel slag into smaller particles, reducing its average particle size. This milling process can induce lattice distortion, local damage, and various defects within the steel slag, leading to an increase in its specific surface area and the number of catalytic active sites, ultimately enhancing its catalytic activity.

Regardless of the modification method, modified steel slags can effectively catalyze various chemical processes, including oxidation [18], biomass pyrolysis [19, 20, 21], catalytic cracking [22], and transesterification [23, 24]. For example, Okoye et al. [23] utilized LF slag modified with 1-15 wt.% NaOH (*Alkali modification*) to catalyze the transesterification reaction between glycerol and dimethyl carbonate, producing glycerol carbonate. $Ca(OH)_2$ from the slag reacted with glycerol to form calcium diglyceroxide and a small amount of water. Under reaction conditions of 75°C, a DMC-to-glycerol molar ratio of 2, and 3 wt.% catalyst, the LF slag modified with 10 wt.% NaOH achieved a glycerol conversion of 99% and a GC yield of 97%.

Kholkina et al. [21] utilized steel slag as a precursor for novel catalytic materials, modifying it with various structure-modifying agents *(alkali modification)*: sodium hydroxide (NaOH), ethylenediaminetetraacetic acid (EDTA), and tetraethylammonium hydroxide (TEAH). These modifications resulted in increased porosity and surface area, enhancing the catalytic performance of the steel slag. The resulting catalysts significantly influenced the yield and composition of bio-oil produced from pinewood pyrolysis. Guo et al. [25] employed steel slag calcined at 800°C as a catalyst for the reforming of biomass pyrolysis tar *(high-temperature activation modification)*, achieving a high conversion rate of 94.1% and a significant syngas yield.

Chen et al. [26] synthesized a Ni/steel slag catalyst using the impregnation method for sludge steam gasification *(compound modification)*. At 900°C, with a steam flow rate of 1.5 g/min and 20% Ni loading, the catalyst significantly increased hydrogen yield by 60.15% compared to raw sludge gasification, producing 45% hydrogen in the gas mixture.

Fusco et al. [27] deposited nanostructured Pd onto steel slag, composed solely of $CaAl_2O_4$ and $Fe_3O_4$, for photocatalytic conversion of $CO_2$ and water into hydrogen and methanol *(compound modification)*. The study successfully converted $CO_2$ into formic acid through photoreduction, followed by its decomposition into hydrogen and methanol under mild thermal conditions.

Recent studies have even demonstrated the potential of unmodified steel slag as a catalyst [22, 28, 29, 30]. Casiello et al. [29] employed steel slag as a heterogeneous catalyst in the transesterification of soybean oil (Fig.1.7), achieving a high yield of fatty acid methyl esters (FAMEs) under optimized reaction conditions without any pretreatment.
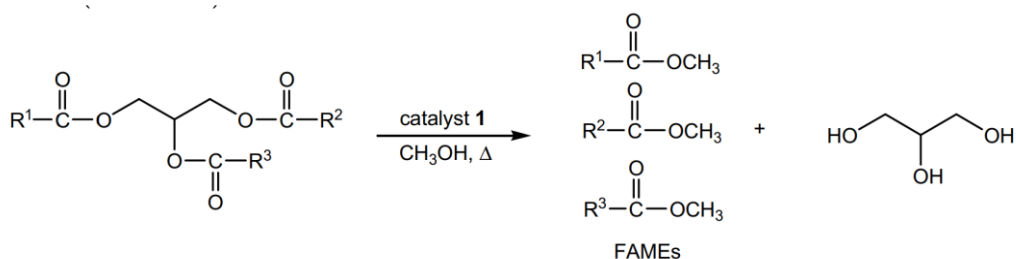


Fig. 1.7 Transesterification of triglycerides for the production of biodiesel (FAMEs) [29]

Kar et al. [22] utilized blast furnace slag (BFS) as a catalyst for the catalytic cracking of used frying sunflower oil. The rich metal oxide content of BFS effectively promoted the cracking process, giving yield of 82.53 wt.% in organic liquid product with excellent fuel properties comparable to diesel fuels. Roushdy et al. [30] investigated the use of electric arc furnace (EAF) steel slag as a heterogeneous catalyst for biodiesel production from waste sunflower cooking oil.  The researchers achieved a 94% biodiesel yield under the following conditions: a methanol-to-oil molar ratio of 20:1, a catalyst loading of 5%, and a reaction temperature of 55.5°C for a reaction time of 1 hour.

## 1.3.   Cigarette butts

Every year, an estimated 4.5 trillion cigarette butts (CBs) are discarded, making up 22-46% of visible litter in urban areas. This poses serious ecological risks due to their non-biodegradable composition and the leaching of toxic chemicals into the

environment [32, 33]. Firstly, CBs leach toxic substances, including nicotine, heavy metals such as Al, Ba, Cd, Cr, Cu, Fe, Pb, Mn, Ni, Sr, Ti, Zn, and polycyclic aromatic hydrocarbons (PAHs), into the surrounding soil and aquatic ecosystems, exacerbating environmental contamination [34]. Secondly, cigarette filters themselves contain a complex mixture of over 5,000 chemicals, including nicotine, metals, PAHs, benzene, phenols, pesticides, carbon monoxide, nitrogen oxides, ammonia, and aldehydes [37]. Among these, at least 150 compounds are recognized for their carcinogenic and mutagenic effects, with 44 commonly found in elevated concentrations [35].

Table 1.2. List of main identified pollutants in cigarette butts [36]

| Categories | Sample |
| --- | --- |
| Metals | Al, Br, Cd, Cr, Cu, Zn, Fe, Mn, Pb, Ni |
| Cyclic compounds | Floren, phenanthrene, anthracene, pyrene, chrysanthemum, benzoalphapyrene, benzobetafurane |
| Toxics | Nicotine, cyanide |
| Other compounds | Carbon and metal nanoparticles, radioactive elements such as $^{210}$Po |

Cellulose acetate (CA), a semi-synthetic polymer, has been widely utilized in the production of cigarette filters since 1950s [38]. Currently, cigarette filter contains approximately 95% of cellulose acetate fibers. This is dictated by good mechanical properties of the fine CA fibers which are bundled and bonded using triacetin (glycerol triacetate) as a plasticizer [39]. However, CA fibers also contribute to their environmental persistence, making them resistant to degradation by natural processes. For instance, the ultraviolet light can break down CA filters into smaller components, these components can persist in the environment for over a decade [40]. Consequently, the recovery of cellulose acetate from CBs represents a crucial environmental initiative to mitigate the pervasive problem of cigarette waste.

### 1.3.1 Cellulose acetate

The synthesis of cellulose acetate typically involves reacting purified cellulose with acetic anhydride in the presence of a catalyst, such as sulfuric acid or perchloric

acid [41]. This reaction results in the substitution of the hydroxyl groups in the cellulose molecule with acetyl groups (Fig. 1.8).
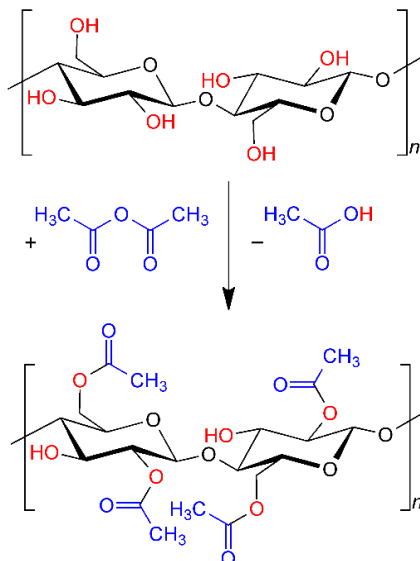
Fig. 1.8 Scheme of cellulose acetate synthesis

The degree of substitution (DS) can be controlled by adjusting the reaction conditions. Such as a higher DS indicates a greater number of acetyl groups per glucose unit in the cellulose chain, which in turn affects the solubility, melting point, and mechanical properties of the resulting cellulose acetate. For instance, cellulose acetate with a DS of 2-2.5 is soluble in organic solvents like acetone, dioxane and methyl acetate [42], higher acetylated types are soluble in dichloromethane [43] and lower DS (0.4–0.9) cellulose acetates may exhibit water solubility [44].

CA exhibits a glass transition temperature ranging from 180 °C to 200 °C and melting temperature within the range of 230–250 °C, which makes it suitable for thermoplastic processing. The material also possesses good tensile strength and flexibility, attributes that are advantageous for producing fibers and films. Biocompatibility of cellulose acetate's makes it suitable for various medical applications, including dialysis membranes, drug delivery systems, and tissue engineering scaffolds. For instance, dialysis membranes made from cellulose acetate are used in hemodialysis to remove waste products from the blood of patients with renal failure [45]. In drug delivery, cellulose

acetate can be applied into core–shell nanoparticles that control the release rate of therapeutic agents, enhancing the efficacy and safety of medications [46]. 3D printed tissue engineering scaffolds fabricated from cellulose acetate provide a supportive matrix for cell attachment and proliferation, aiding in the regeneration of damaged tissues [47].

### 1.3.2 Valorization of cellulose acetate from cigarette butts

Recycled cellulose acetate materials from cigarette butts can be used for different application as support material for bricks [48], modifier for asphalt concrete [49], sound absorbing material [50], and nonwoven material for surface water treatment [51]. Therefore, a lot of research on the valorization of cellulose acetate from cigarette filters has focused on destructive methods such as pyrolysis to produce carbon material [52], [53, 54]. In addition, other research works are devoted to obtaining nanofiltration membranes for selective separation from purified cellulose acetate [55, 56].

All the listed studies mainly refer to the production of materials and additives. Laurenza et al. [57] demonstrated the possibility of obtaining levulinic acid from cellulose acetate by means of a one-pot hydrothermal process carried out at 200 °C for 2 h and catalysed by phosphoric acid. Figure 1.9 represents the main reaction of the one-step synthesis, displaying the maximum yield of 43.9% in levulinic acid at 240 °C.
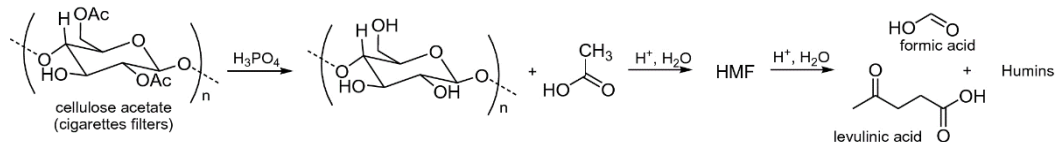


Fig.1.9 One-step synthesis of levulinic acid from cigarette filters [57]

### 1.3.3 Cellulose acetate recovering methods

Non-destructive methods for cleaning CA fiber typically involve multiple sequential cleaning in an aqueous solution, followed by washing in an organic solvent, most often ethanol. For instance, Ogundare et al. [58] extracted CA by washing in water, ethanol and subsequent bleaching. Separated from paper and tobacco CF have been soaked and washed with water, and extracted with ethanol 20 mL/g for 24 h at room

temperature. After obtained cellulose acetate was bleached using 1.25 w/v% NaOCl 10 mL/g for 6 h at room temperature.

Benavente et al. [59] studied the extraction of heavy metals from cigarette butts using aqueous solutions of 5% NaCl, 5% NaAc, and 0.02% $H_2SO_4$. After three extractions with absolute ethanol, the samples were further extracted three times with the less polar organic solvents diethyl ether and hexane. The results indicated that the acidic solution was most effective for extracting Al, Fe, Cu, Zn, Ba, and Pb, while the NaCl solution was most efficient for extracting Mn and Sr. In turn, De Fenzo et al. [60] suggested a method for extracting CA from cigarette butts involving washing them in hot water at 50°C for 60 minutes, followed by three cold water washes. To remove potential organic compounds, the butts were then washed twice in 99% ethanol. Finally, the obtained CA samples were dried in an oven at 60°C for 60 minutes. The authors concluded that the quality and properties of the extracted and purified CA were comparable to those of pure CA fiber.

The study of Arroyo et al. [61] showed the extraction of CA using a Soxhlet extraction process involving a 1:1 mixture of toluene and ethanol for 5 hours of reflux. This process effectively eliminated nicotine and other organic components.  The extracted CA was then dried and dissolved in acetone for 30 minutes at room temperature with stirring. The solution was subsequently precipitated in distilled water, filtered, and dried at 45°C. In a more recent study, De Cesaris et al. [62] proposed a simplified cleaning method for CA filters. This method involves washing the dirty CA with hot water at 90-100°C for 15 minutes, followed by washing in 96% ethanol at 58-68°C for another 15 minutes. Approximately 200 mL of each solvent was required for every 1.5 g of CA filters. The cleaned filters were then dried in an oven at 30°C for 1 hour.

## 1.4. Tunicates

Tunicates are marine invertebrates exhibiting a fascinating diversity of forms and functions belonging to the family Ascidiacea under the subphylum Urochordata, phylum Chordata. Tunicates with approximately 3000 recognized species worldwide play a crucial role in marine ecosystems [64].

Tunicates are classified into three primary classes: ascidiacea, thaliacea, and appendicularia. Ascidiacea are sessile organisms that attach to surfaces like rocks, shells, or man-made structures (Figure 1.10a). They can be solitary or colonial. Thaliacea, or salps, are pelagic tunicates known for their transparent, barrel-shaped bodies and rapid population growth in nutrient-rich waters, often forming long chains through asexual reproduction (Figure 1.10b). Appendicularia, also known as larvaceans, are small, free-swimming organisms that retain their tail and notochord throughout their lives. They are less diverse but widely distributed in the world's oceans, contributing to the formation of marine snow and the movement of organic matter through the water column (Figure 1.10c).
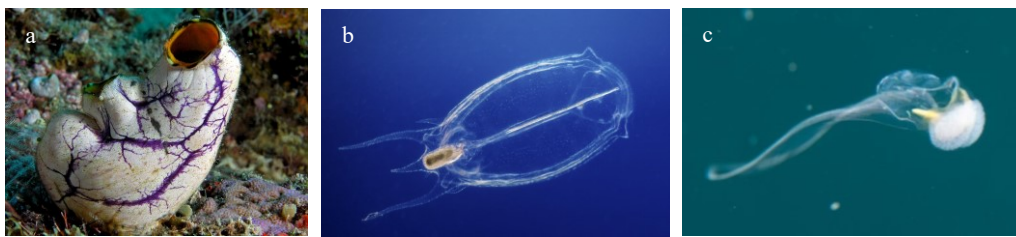
Fig. 1.10 Types of tunicates: a - Ascidiacea, b - Thaliacea, c - Appendicularia

All tunicates share a common body plan characterized by a sac-like structure wrapped in a tough outer covering called the tunic (Fig.1.11). Tunic is a hierarchical complex of cellulose and protein [69], consisting of a thin, dense outer layer and a thick inner layer of fibers. It consists of approximately 60% cellulose [70] approximately 40% protein and trace amounts of lipid components and ash.
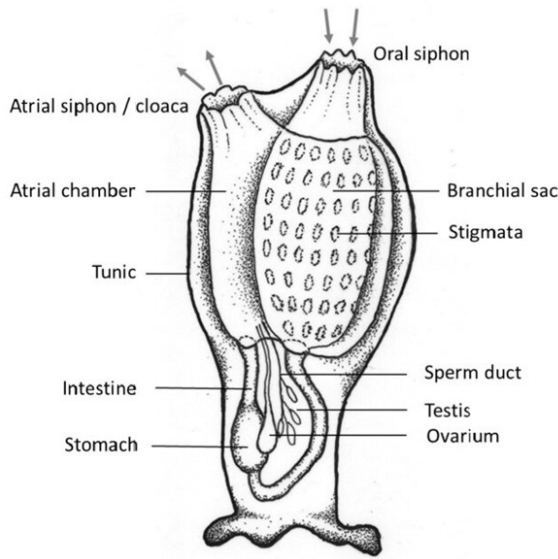
17

Fig. 1.11 General structure of ascidians [65]

Particularly invasive tunicate species (such as example *Styela clava*, *Ciona intestinalis*, *Botrylloides violaceus* and *Botryllus schlosseri*) pose a significant threat to local ecosystems and aquaculture, often introduced through shipping or aquaculture [66]. Such species disrupt the existing marine environment by competing with native species for resources. Therefore, this contributes to ecological imbalances (the biodiversity and sustainability of local fisheries) and poses significant challenges for marine industries (reduction of productivity and increase maintenance costs).

### 1.4.1 Clavelina oblonga

*Clavelina oblonga* is considered an invasive species in many parts of the world (Fig. 1.13) due to its ability to form large, dense colonies that can outcompete native species for space and resources. The genus *Clavelina* is distinguished by the elongated and tubular shape of its zooids, typically ranging from 1.5 to 3 cm in length, with a transparent tunic that reveals the internal anatomy of the organism [67] (Fig. 1.12). Such tunicate is widely distributed in subtropical and tropical marine environments, especially in shallow coastal areas, attaching to rocks, coral reefs, mangrove roots and

artificial substrates such as piers and ship hulls. It is commonly found in the western Atlantic, from the North Carolina coast to the Caribbean Sea, and populations have also been recorded in the Gulf of Mexico [71](Fig.1.13). However, recent decades *Clavelina oblonga* has been introduced in the Mediterranean (Ordóñez 2016) and in the Adriatic Sea [72], thereby adapting to lower temperatures.
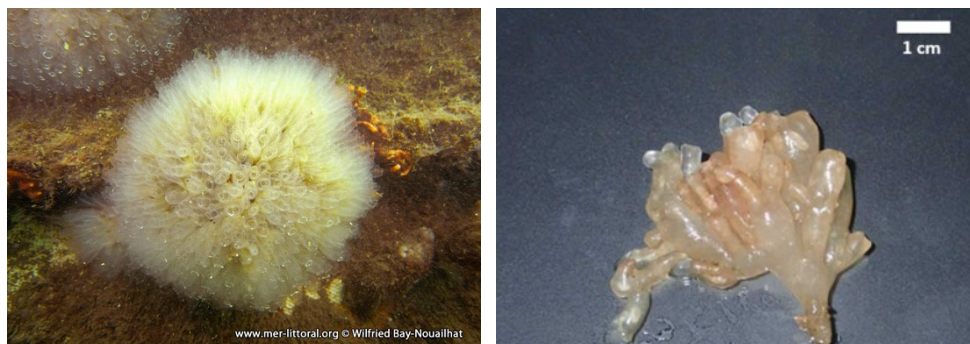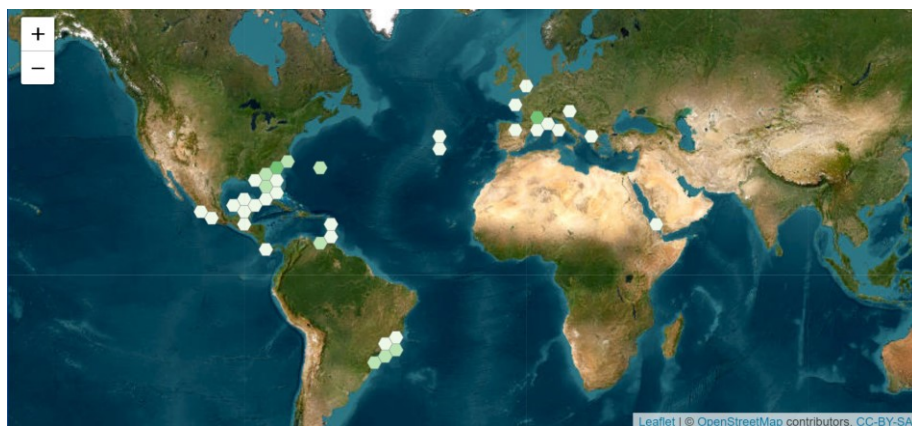


Fig. 1.12 Clavelina obolonga a)colonia [67] b) zood [72]



Fig. 1.13 Habitats of Clavelina oblonga tunicates [67]

### 1.4.2 Application of tunicates cellulose

Tunicates are the only known animal source of nanocrystal cellulose [68]. Moreover, crystallinity of tunicate cellulose is over 85%, which is higher than other cellulose sources (Table 1.3). Ascidian tunic is a hierarchical complex composed of cellulose and protein, composed of a thin, dense outer layer and a thick inner layer of

fibers. About 60 % of it is cellulose, roughly 40 % is protein and extremely small amounts of lipid components and ash [73]. The exact cellulose content depends on the tunicate species (Table 1.4).

Table 1.3. Differences of cellulose from different sources [75]

| Source | Length (nm) | Diameter (nm) | Crystal structure | Crystallinity |
|---|---|---|---|---|
| Cotton | 100–300 | 8–10 | Mainly $I_\beta$ | 80–85 % |
| Wood | 100–300 | 3–10 | Mainly $I_\beta$ | 43–65 % |
| Tunicate | 100–2000 | 10–30 | Nine-tenths $I_\beta$ | 85–100 % |
| Algae | 100–2000 | 10–20 | $I_\alpha$ | 70–80 % |
| Bacteria | 100–2000 | 5–10 | $I_\alpha$ | 75–95 % |

Among the studied shell types, the highest cellulose content is 57.67% in the outer tunic of *Styela plicata* tunicate. The cellulose content of *Halocinthia roretzi* species is also high at 52.59%, while *Ascidia sp*. and *Ciona intestinalis* contain only 37.57% and 37.29% cellulose, respectively.

Table 1.4. General chemical compositions of the outer shells of tunicate species [74]

| Tunicates Species | *Ciona intestinalis* | *Ascidia sp.* | *Ciona intestinalis* | *Halocynthia roretzi* |
|---|---|---|---|---|
| Crude protein (%) | 30.86 | 41.34 | 51.82 | 43.05 |
| Crude lipid (%) | - | - | - | - |
| Cellulose (%) | 57.67 | 37.57 | 37.29 | 52.59 |
| Lipids calculated by fatty acid (%) | 0.35 | 0.98 | 0.42 | 0.18 |
| Total sugar (%) | - | - | - | - |

Tunicate cellulose offers several advantages over traditional plant-derived cellulose, including higher crystallinity, superior mechanical properties, and smaller nanocrystal size, making it a sought-after material for various applications. Such properties of tunicate nanocellulose find application in important fields such as tissue engineering, drug delivery, optics, flexible electronics, etc (Table 1.5).

Table 1.5. Applications of tunicate nanocellulose [75]

| Application area | Specific application | Advantages |
|---|---|---|
| Biomedicine | Tissue engineering; Drug delivery; Wound healing | Provide an ideal microenvironment for cell adhesion, growth, reproduction and differentiation; Provide excellent encapsulation of specific cells |
| Energy and electronics | Flexible electronics; Fuel cell and ionic conductive materials; Responsive optical materials | Higher in-plane thermal conductivity; Better mechanical properties; Optical properties |
| Polymer reinforced materials | Enhancement of polyimide, poly (vinyl acetate), polyvinyl alcohol, *etc.* | Better mechanical properties, water absorption properties, barrier properties and thermal properties |
| Food packaging | Renewable and biodegradable green packaging materials | Better mechanical properties and thermal stability; Environmental protection and recyclable performance; High transparency and excellent oxygen barrier properties |
| Paper industry | Paper additive | Better tear index, tensile index, and breakage |
| Environmentally friendly materials | Porous fiber media to treat air | Better filtration efficiency |

Huang et al. [77] obtained tunicate cellulose nanocrystals (TCNCs) modified filter papers to efficiently separate oil/water mixtures and emulsions, exhibiting superhydrophilic/underwater superoleophobic surface and excellent stability. Zhang et al. [76] prepared highly flexible paper-like materials of polypyrrole (PPy) and tunicate cellulose nanocrystals (T-CNs) nanocomposites with high electrical conductivity values and good mechanical properties. These films have interesting properties that may find applications such as sensors, electronic devices, antistatic and anticorrosive nanocoatings and flexible electrodes. The study of Huang et al. reported [78] the top-down

fabrication of biodegradable multilayer tunicate cellulose films with controlled mechanical properties, providing a potential solution for environmental pollution caused by non-degradable waste plastics. The as-prepared MTCFs exhibited improved thermal stabilities, excellent mechanical properties, and good degradability in natural soil. Microbeads of alginate and tunicate cellulose nanofibrils (CNF) were prepared by Kjesbu et al [79]. Such beads can be used for the encapsulation of cells and hence have the potential for use in both cell therapy and tissue engineering applications. Cui et al.[80] designed hydrogel artificial muscles that can mimic the properties of natural muscles, with potential applications in biomedical fields. Tunicate cellulose nanocrystals (TCNCs) are incorporated into polymeric networks via host–guest interactions to reinforce the hydrogel. These hydrogel muscles exhibit a high actuation rate, large actuation strain, and shape memory property.

### 1.4.3 Extraction of cellulose from tunicates

Numerous studies [81, 82, 83, 84, 85, 86, 87] have explored the cellulose extraction from tunicates. They can be classified into two categories: two-step and three-step treatments. The two-step purification consists of an alkaline treatment (deproteination) step in the presence of NaOH or KOH and a bleaching step with the addition of $H_2O_2$, $NaClO_2$ or mixtures of $NaClO/CH_3COOH$ and $NaClO_2/CH_3COOH$. The three-stage purification consists of prehydrolysis in the presence of $H_2SO_4$, followed by kraft cooking with $NaOH/Na_2S$, and finally by bleaching in the presence of NaClO. Comparison of methods for purification of cellulose from tunicates was not possible because many authors did not specify yields and parameters of the purified product.

#### Two-step treatments

Yuan et al. [81] prepared cellulose whiskers from the mantle of tunicate *Halocynthia roretzi*. The mantle material was treated by 5% (w/w) NaOH and a mixture of 0.3%(w/w) $NaClO_2$ in 0.1 M acetate buffer (pH=4.5) with a ratio of 50:50(v/v) successively. Then the cellulose material was treated with 50% $H_2SO_4$ at 70 °C for 8 h.

Shanmuganathan et al. [82] obtained Cellulose Whiskers from *Styela clava* tunics. The tunicates separated from internal organs were washed thrice in 5% KOH solution

for 24 h at 80 $^{\circ}$C. Cellulose whiskers were washed in 5% KOH solution for 24 h at 80 $^{\circ}$C. Afterwards, the cellulose was bleached in the presence of sodium hypochlorite and acetic acid solution with hourly addition of fresh reagents until complete bleaching.

Zhang et al. [83] extracted cellulose from tunics of *Halocynthia roretzi Drasche* by alkaline treatment and bleaching process. Tunics has been washed in 5 wt% NaOH solution during 24 h at 80 °C. Subsequently, product was bleached using 4 wt% $H_2O_2$ solution for 3 h at 80 °C. Then cellulosic material was functionalised by hydrolysis using sulphuric acid.

Darpentigny et al. [84] also obtained Cellulose nanocrystals from the mantle of *Halocynthia roretzi* tunicate using a two-step treatment. Deproteinisation was carried out in 1N NaOH solution with further bleaching in 0.3% $NaClO_2$. The purified cellulose particles were further subjected to acid hydrolysis in 50 wt% sulphuric acid at 50 °C for 20 h with stirring. The obtained nanocellulose crystals had a high crystallinity of 94%.

### *Three-step treatments*

Dunlop et al. [85] extracted nanocrystal cellulose from *Styela clava*. The dried tunic powder has been treated in 5 wt. % NaOH at 80 °C for 24 hours (Fig. 1.13). Then cellulose material was bleached with $NaClO_2$ powder and glacial $CH_3COOH$ for 1 hour at 60 °C whereupon fresh reagents were added three times every 1 hour. Yield of cellulose after deproteinization procedure was 31%. Next bleached tunic powder was hydrolyzed to T-CNCs by adding five liters of 64 wt% $H_2SO_4$ for 2 hours at 45 °C.
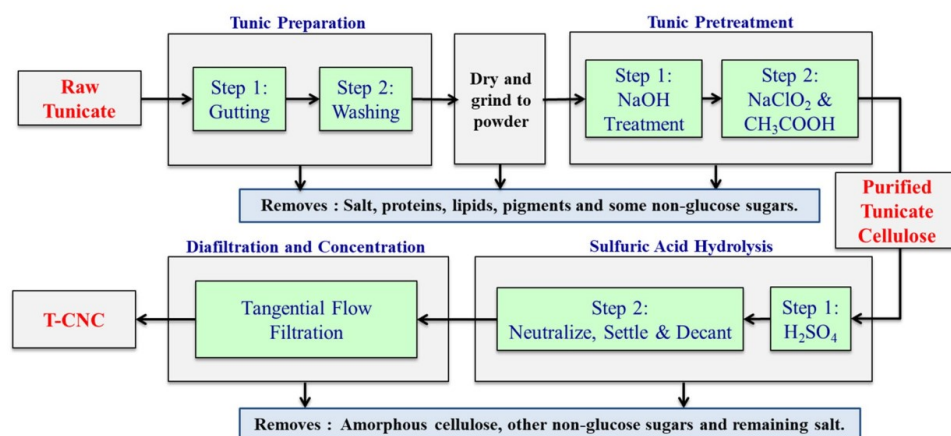


Fig. 1.13 Flowchart for isolation of cellulose nanocrystals from tunicates [85]

Zhao et al. [86] isolated cellulose from four types of tunicates: *Ciona intestinalis* (CI), *Ascidia sp.*(AS), *Halocynthia roretzi* (HR) and *Styela plicata* (SP). Separated tunics has been milled to powders and conducted 3 step treatment (fig. 1.14): prehydrolysis processed in 1% $H_2SO_4$ at 180°C with kraft cooking in mixture (9%/3%) of NaOH and $Na_2S$ at 180°C and final bleaching in 3% NaClO at 75°C. The production yields of chemically pure cellulose following the sequence were 12.35%, 2.54%, 20.99% and 23.92 % for CI, AS, HR and SP, respectively.
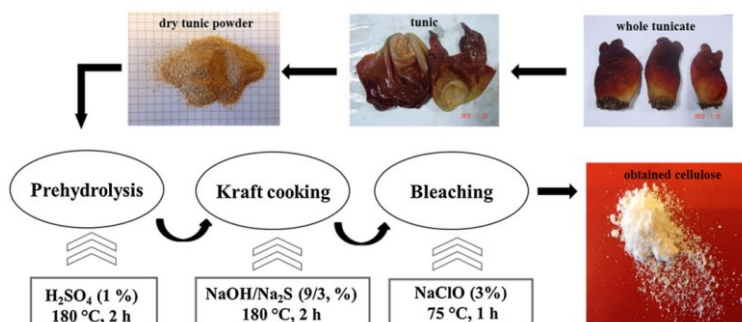


Fig 1.14 Scheme of the tunicate cellulose preparation [86]

Dunlop et al. [87] extracted Celulose nanocrystals (CNC) from invasive *Ciona intestinalis* and *Styela clava* tunicates by same prehydrolysis-kraft cooking-bleaching method as depicted on Fig.1.15. The average yields of CNC obtained are ~44% for *Ciona intestinalis* and ~32% for *Styela clava* tunicates.
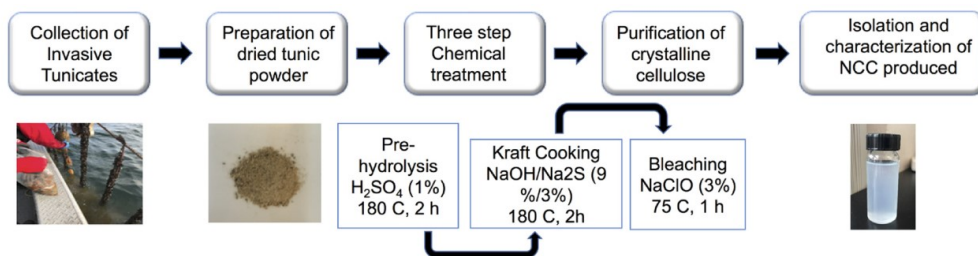


Fig 1.15 Producing nano crystals of cellulose from tunicates [87]

Despite the ability of the purification methods to yield high-quality cellulose, they all share a significant drawback: the need for manual separation of mantles from

the internal organs of tunicates. This limitation hinders the large-scale production of high-quality nanocellulose from tunicates.

## 1.5. Conclusions

Waste valorization, an essential process within the field of sustainable development, has received increasing attention as a solution to the growing challenges posed by waste generation and resource depletion. As global populations and consumption rates continue to rise, the accumulation of waste keeps increasing, leading to environmental, social, and economic implications. Waste valorization addresses these issues by transforming waste materials into valuable resources, such as energy, chemicals, or alternative materials, thereby minimizing environmental impact and promoting circular economies. Different types of wastes such as industrial (steel slags), municipal (cigarette butts) and natural (tunicates) were considered as promising for valorization process to high added value products.

Steel slags can be valorized in the field of catalysis due to their high metal content and their strong alkaline features, that can be employed to catalyze several organic reactions useful for the synthesis of chemicals and fine chemicals (intermediates to produce drugs, dyes, phytochemicals and so on).

Another noteworthy item in the framework of waste valorization concerns cigarette butts, which are composed of 95% cellulose acetate polymer. The significance of collecting and recycling this particular waste is largely attributed to the detrimental environmental impact of cigarette butts, including the leaching of toxic organic pollutants and metals, as well as microplastic contamination. Furthermore, the recovery of cellulose acetate through economically and environmentally sound treatment will result in a material suitable for a multitude of applications.

The production of high-quality cellulose from invasive types of tunicates, which are wastes from aquaculture farming, is also of interest in the field of waste treatment. Therefore, the current research challenge aimed to identify an efficient, environmentally friendly method for extracting valuable cellulosic material.

# 2.   STEEL SLAGS BASED CATALYSTS

## 2.1.   *Steel Slags characterization*

Sample of steel slag was collected from a waste disposal site at a steel plant *Acciaierie d'Italia* (Taranto, Italy). The original heterogeneous mixture of the steel slag (fig. 2.1a) was sieved through an 80-mesh sieve. A fraction of 0.177 mm size was subsequently used in experiments (Fig. 2.1b).
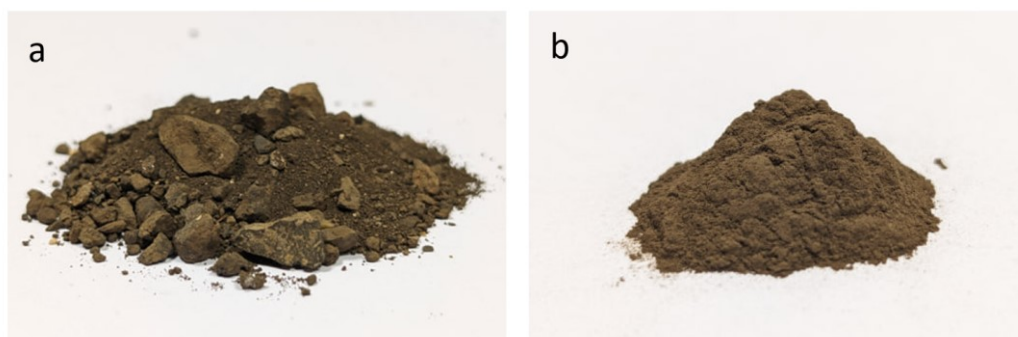


Fig. 2.1 Steel slag a) before sieving b) after sieving

### 2.1.1 Elemental analysis

The chemical composition of steel slag was determined by Portable X-ray fluorescence analysis (PXRF). As can be seen from Table 2.1, the main components of the slag are calcium (28.9%) and iron (17.6%), as well as small amounts of manganese (4.4%) and silicon (3.4%). In addition, minor contents (<1%) of chlorine, titanium and chromium were found.

Table. 2.1 Elemental analysis of steel slag by PXRF

| Element | Ca | Fe | Mn | Si | Cl | Ti | Cr |
|---------|------|------|------|------|------|------|------|
| Content, %$_w$ | 28.90 ± 2.22 | 17.62 ± 2.03 | 4.44 ± 0.45 | 3.36 ± 0.16 | 0.72 ± 0.06 | 0.14 ± 0.02 | 0.09 ± 0.01 |

X-ray diffraction analysis (XRD) was applied to determine the phase composition. The XRD pattern was done within the range of $2\theta=11$-80 deg. (Figure 2.2). It should be noted that the superimposition of the multiphase data based on Ca, Fe and

Si prevented the effective separation of the diffraction peaks to analyze data with quantitative results. Thus, the main phases within the Steel Slag were qualitatively determined as Larnite ($Ca_2SiO_4$), Brownmillerite ($Ca_2(Al,Fe^{3+})_2O_5$), Calcite ($CaCO_3$), Portlandite ($Ca(OH)_2$), Dolomite ($CaMg(CO_3)_2$). Moreover, a minor inclusions of Quarts ($SiO_2$) and Hematite ($\alpha$-$Fe_2O_3$) were also detected based on the low intensity within the XRD pattern.
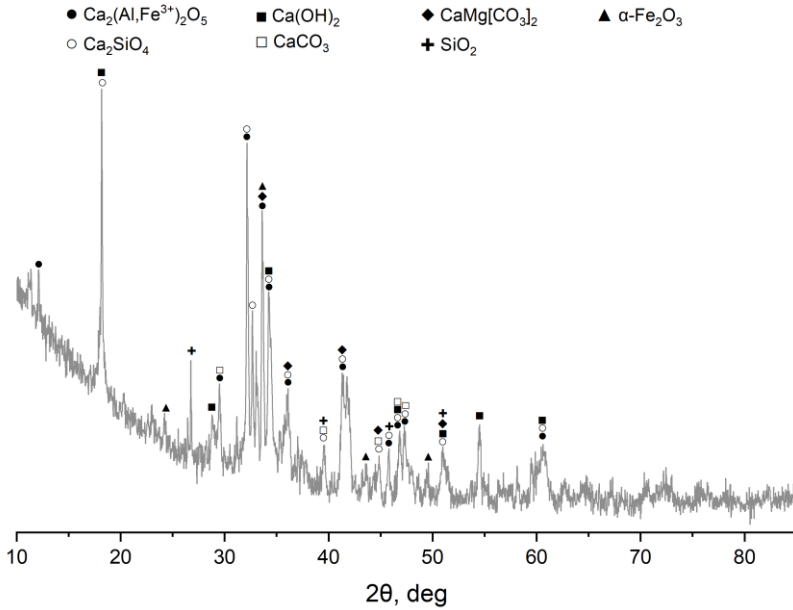


Fig. 2.2 XRD patterns of Steel slags waste material

Such phases like larnite, brownmillerite, calcite, dolomite and hematite formed during the initial formation and cooling of the slag material after a steel making process [88]. In contrast, the formation of portlandite was related to Steel Slag storage and weathering conditions since the typical form of calcium in steel slag is CaO [89, 90] (3.1).

These phases are likely formed due to the reaction:

$$CaO\ (s)\ +\ H_2O \rightarrow (CaOH)_2\ (s) \tag{3.1}$$
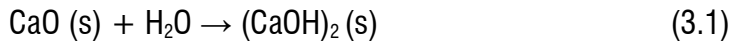
The FT-IR spectra of Steel Slags in the range of 400 to 4000 $cm^{-1}$ illustrated in Fig. 2.3 display hydroxyl stretching vibrations from calcium hydroxide within the first peak at 3640 $cm^{-1}$ [91]. Furthermore, the absorption band at 1417 $cm^{-1}$ is attributed to the

C—O bond. Peaks at 875 cm$^{-1}$ and 712 cm$^{-1}$ correspond to vibrations of the $CO_3^{2-}$ ion in calcite [91, 92].
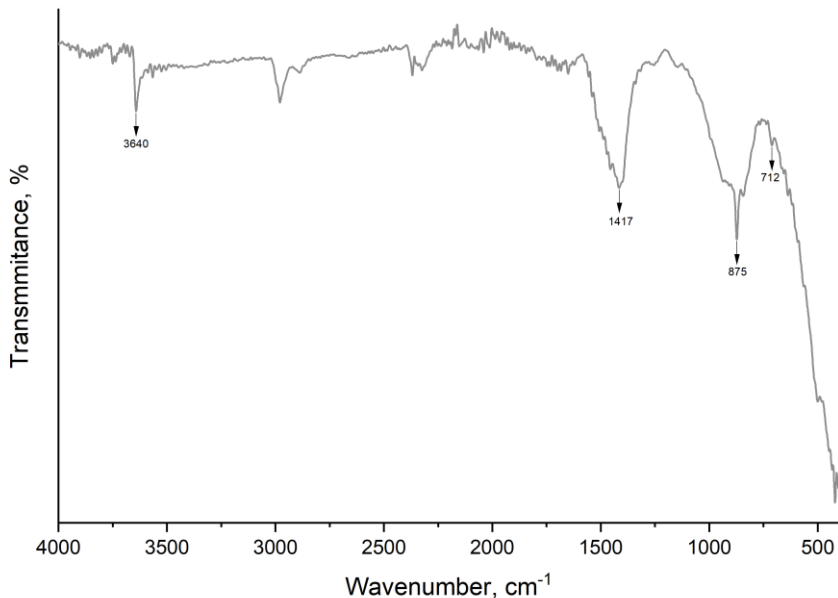


Fig. 2.3 ATR-FT spectra of Steel Slag

EDX-mapping technique was applied to analyze the distribution of the elements of Steel Slag and to identify the morphology of the present compounds (Fig. 2.4). The results showed that the slag particles based on calcium included irregular distribution of iron, silicon, manganese, magnesium, and aluminum inclusions on their surface. The distribution of oxygen follows that of calcium, indicating a prevailing volume of calcium-containing compounds, such as calcium carbonate or calcium oxide.
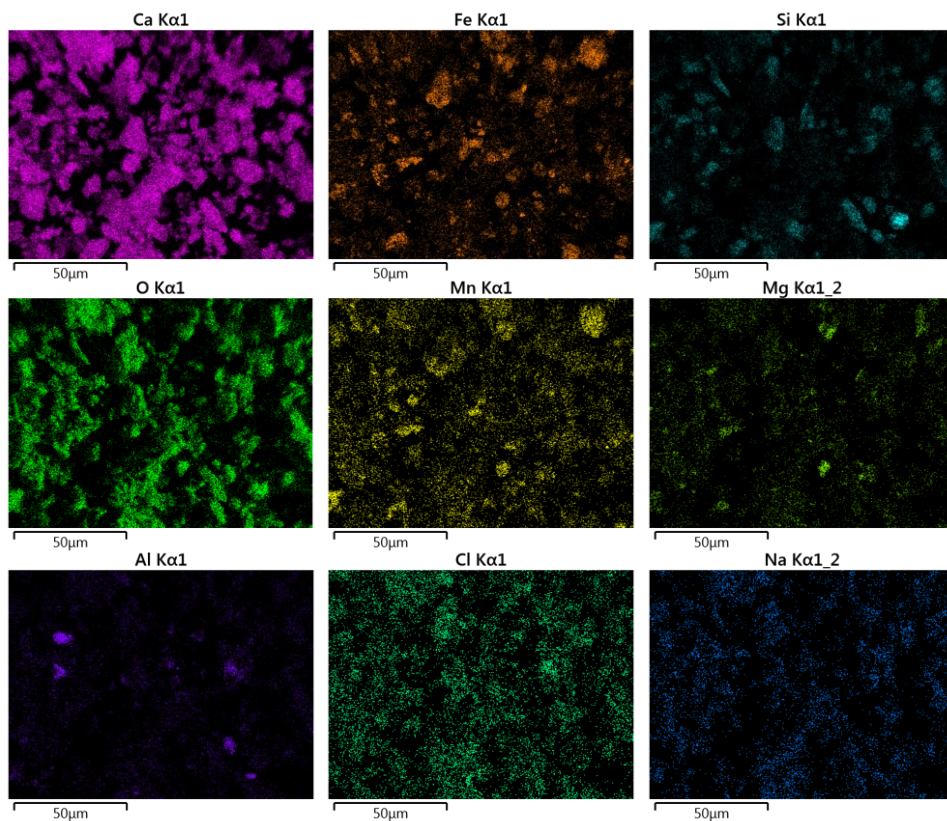
Fig. 2.4 EDX-mapping of Steel slags

TGA/DSC analysis of Steel slags were performed in nitrogen flow in temperature range from 25 to 1000 °C with ramp 10 °C/min. Typical TGA-DSC-DTG curves (Fig. 3.5) display four zones of mass loss corresponding to DTG peaks at temperatures of 105°C, 420°C, 625°C and 825°C. The first mass loss of 3.4% in range 25-380°C is attributed to the evaporation of sorbed moisture and interlayer/crystallized water). The most intense DTG peak at 420°C is related to the decomposition of the portlandite phase [93, 94] to calcium oxide (3.2) with 3% of mass loss. A minor mass loss of 1.54% was observed at 625 °C due to the decomposition of the $CaCO_3$ (3.3) [95, 96, 97]. The last peak at 825 °C with mass loss of 0.42% presented due to the decomposition of the sodium carbonate (3.4) [98].

$$Ca(OH)_2 \text{ (s)} \rightarrow CaO \text{ (s)} + H_2O \text{ (g)} \hspace{3cm} (3.2)$$

$$CaCO_3\ (s) \rightarrow CaO\ (s) + CO_2\ (g) \qquad\qquad (3.3)$$

$$Na_2CO_3 \rightarrow Na_2O + CO_2 \qquad\qquad (3.4)$$
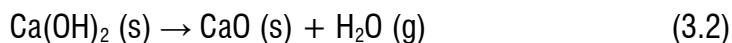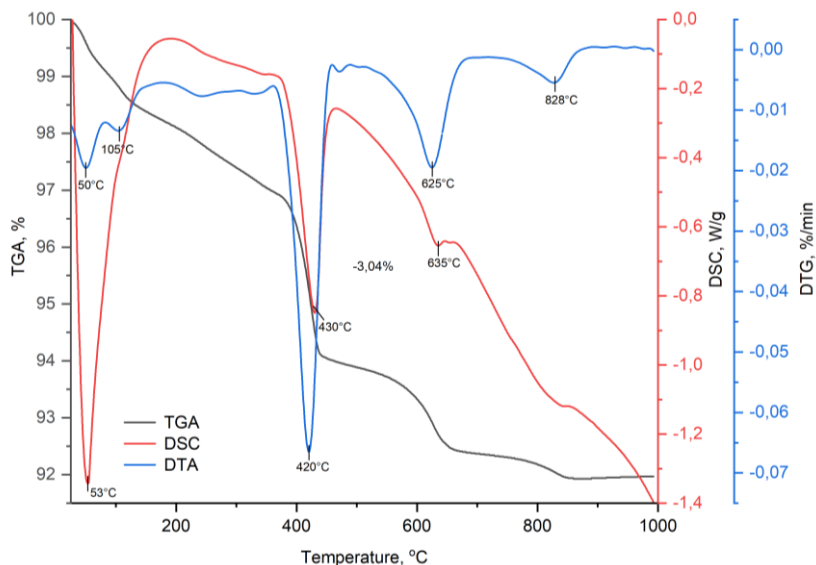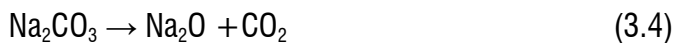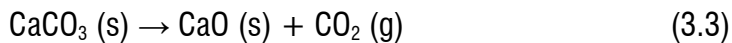


Fig. 2.5 TGA-DSC-DTG curves of Steel Slag

FESEM image of steel slag shows a heterogeneous Steel Slag structure with a wide range of particle sizes, as presented in Fig.2.6. The surface of Steel Slag is rough with the presence of a large loose porous structures. This structure is advantageous for a contact (adhesion) between reactants and Steel Slag, which in turn can improve the catalytic activity.
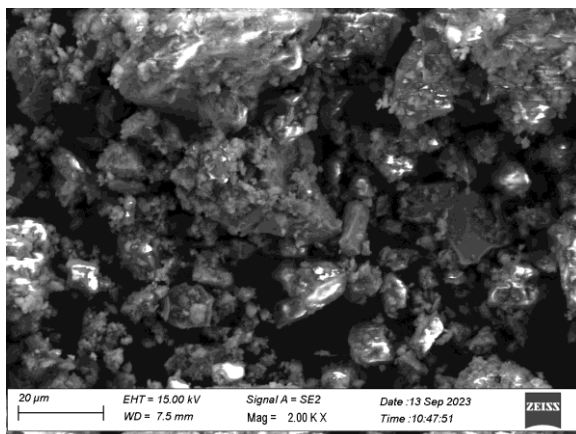


Fig. 2.6 FESEM micrographs of Steel slags waste material
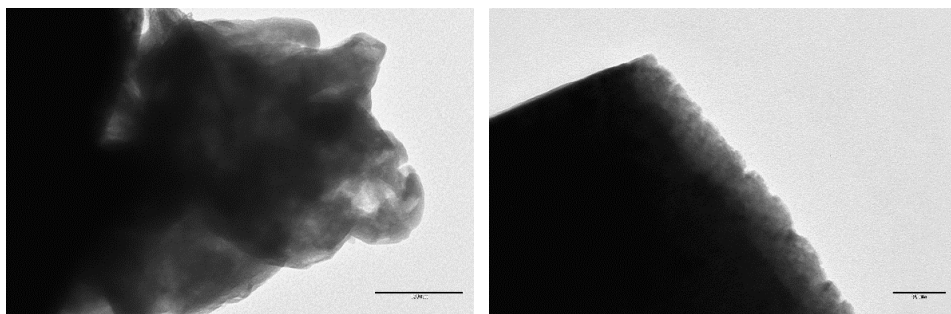
Fig. 2.7 TEM micrographs of Steel Slags waste material

## 2.2. Synthesis of Cu/SteelSlags catalyst

One of the common and simple methods for the synthesis of transition metal nanoparticles is mixing the metal salt with alkali to produce metal hydroxide and followed by reduction to metal. For instance, Q. M. Liu [99] reported that a method for the synthesis of copper nanoparticles is the addition of NaOH to the $CuSO_4$ solution until pH = 11 for obtaining copper hydroxide (3.5), which is easy to reduce to $Cu^0$ (3.6) by sodium borohydride ($NaBH_4$) water solution (3.7):

$$CuSO_4 + 2NaOH \rightarrow Cu(OH)_2 + Na_2SO_4 \qquad (3.5)$$

$$NaBH_4 + 2H_2O \rightarrow 4H_2 + NaBO_2 \qquad (3.6)$$

$$Cu(OH)_2 + H_2 \rightarrow Cu + 2H_2O \qquad (3.7)$$
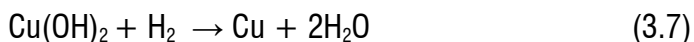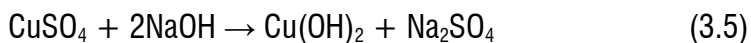
The present steel slag contains a high quantity of portlandite ($Ca(OH)_2$), which interacts with copper sulphate in an exchange reaction of $Ca^{2+}$ and $Cu^{2+}$ ions with formation of copper hydroxide and calcium sulphate (3.8). Therefore, the synthesis of copper nanoparticles on steel slag does not require any additional alkali.

$$Ca(OH)_2 + CuSO_4 \rightarrow Cu(OH)_2 + CaSO_4 \qquad (3.8)$$
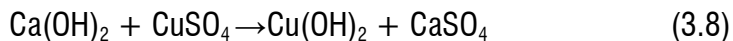
The Cu/SteelSlags catalysts precursors were synthesized by the impregnation method. Detailed synthesis conditions are described in the experimental part. Briefly, 80 mesh steel slag powder was mixed with aqueous solution of copper sulphate

pentahydrate and stirred intensively at 40°C for 2 hours After solid part was then separated by centrifugation, washed with deionized water and dried in oven at 80°C. A complete list of catalysts and synthesis conditions is given in Table 3.1.
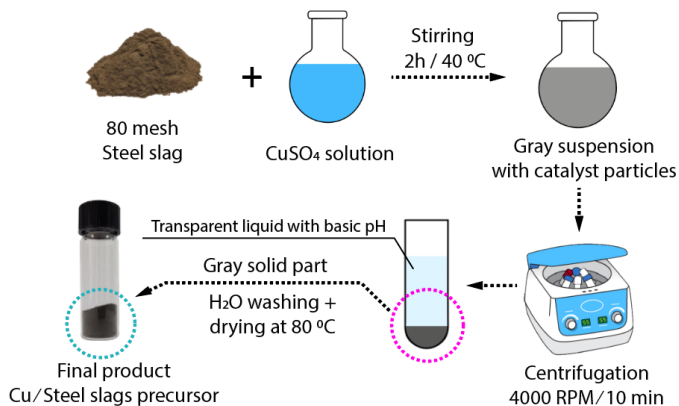


Fig. 2.8 Scheme of synthesis of Cu/SteelSlags precursor

Eleven catalysts were synthesized with variation of the following parameters: concentration of Cu on steel slag (10%, 15% and 20%), reduction of Cu method (without pre-reduction, $NaBH_4$ reduction and calcination in $H_2$), synthesis time (2 or 15 hours) and additional ultrasonic treatment (Table 2.2).

Table 2.2 Synthetized copper catalyst

| Sample name | Description |
|---|---|
| 10Cu/SS_pr | 10%Cu/SteelSlags precursor |
| 10Cu/SS_calc | 10%Cu/SteelSlags cat. reduced by calcination in $H_2$ at 300°C |
| 10Cu/SS_NaBH4 | 10%Cu/SteelSlags cat. reduced by $NaBH_4$ |
| 15Cu/SS_pr | 15%Cu/SteelSlags precursor |
| 15Cu/SS_calc | 15%Cu/SteelSlags cat. reduced by calcination in $H_2$ at 300°C |
| 15Cu/SS_NaBH4 | 15%Cu/SteelSlags cat. reduced by $NaBH_4$ |
| 20Cu/SS_pr | 20%Cu/SteelSlags precursor |
| 20Cu/SS_calc | 20%Cu/SteelSlags cat. reduced by calcination in $H_2$ at 300°C |
| 20Cu/SS_NaBH4 | 20%Cu/SteelSlags cat. reduced by $NaBH_4$ |
| 15Cu/SS_pr_15h | 15%Cu/SteelSlags precursor with mixing time 15h |
| 15Cu/SS_pr_u.s. | 15%Cu/SteelSlags precursor with ultrasonic pretreatment |

## 2.3. Catalytical tests of Cu/SteelSlags catalyst in hydrogenation of nitroarenes
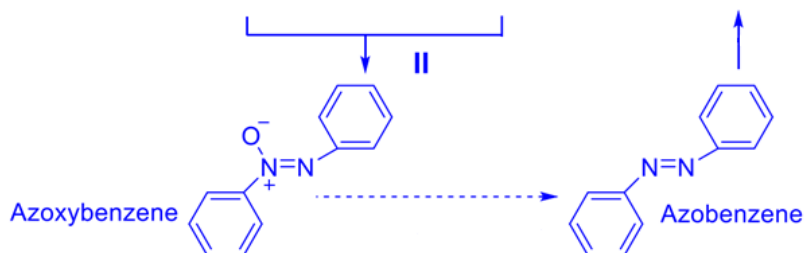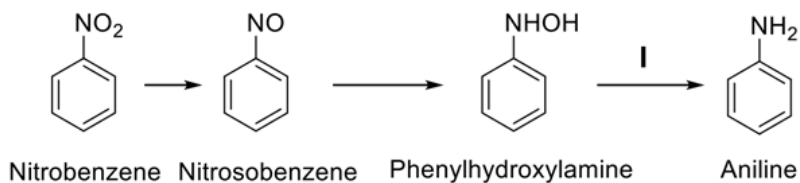
### 2.3.1 Hydrogenation of nitroarenes

Nitroarenes represent a versatile class of aromatic compounds characterized by the presence of one or more nitro groups ($-NO_2$) attached to an aryl ring. The reduction of nitroarenes to amines is a key step in the synthesis of numerous commercially important compounds. Aniline, the simplest aromatic amine, is a precursor of a variety of industrial chemicals, including polyurethane foams, dyes, and rubber processing chemicals. Additionally, more complex nitroarenes are used in the production of pharmaceuticals such as paracetamol (acetaminophen), which is synthesized from 4-nitrophenol via reduction to 4-aminophenol [100]. In agrochemicals, nitroarene reduction is used to synthesize herbicides and insecticides, while in the dye industry, aniline derivatives serve as the basis for a wide range of azo dyes, which are used to color textiles, leather, and plastics [101].

The reduction of nitroarenes can be achieved through various catalytic and non-catalytic processes, utilizing a variety of reducing agents (Scheme 2.1).
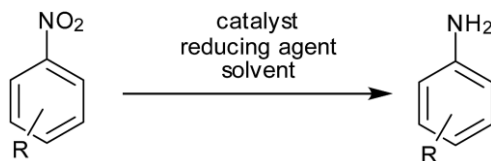


Scheme 2.1 General scheme of nitroarenes reduction

Nitrobenzene reduction can be proposed for two different routes (Scheme 2.2). In the direct route (black), the nitro compound is reduced to the corresponding nitroso, aryl/alkylhydroxylamine and finally aniline. In the condensation route (blue), the nitroso is condensed with N-aryl/alkylhydroxylamine species to give the corresponding azoxy intermediate. This is then converted to azo-, hydrazo- and finally aniline.

Scheme 2.2 Haber mechanism of nitrobenzene reduction:
black – direct route, blue – condensation route

An important element in the reduction of nitroarenes is the source of hydrogen, as used hydrogen gas, sodium borohydride ($NaBH_4$), silyl hydrides, hydrazine hydrate, and alcohols such as glycerol or isopropanol in combination with alkaline agents [102]. Sodium borohydride ($NaBH_4$) is a versatile and mild reducing agent which is also widely used to reduce nitro compounds to amines. Under aqueous or protonic solvent conditions, it slowly hydrolyses to form $H_2$ with the formation of non-toxic sodium borate as a by-product. Transition metal-based catalysts can greatly accelerate these reaction (3.6). $NaBH_4$ is preferred in reactions where sensitivity or selectivity is required as it operates under mild conditions [103].
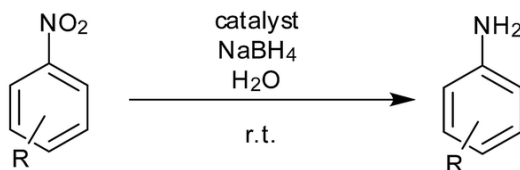


Scheme 2.3 Nitroarene reduction with $NaBH_4$ reducing agent

Noble metal catalysts, particularly those based on platinum [104], palladium [105], rhodium [106, 107] have been extensively used in the reduction of nitroarenes. These metals can activate molecular hydrogen ($H_2$) and facilitate its transfer to the nitro group.

However, the high cost and limited availability of noble metals such as palladium and platinum have driven interest in developing catalytic systems based on more abundant transition metals [108], such as iron [109], nickel [110], cobalt [111] and copper [112, 113, 114].

### 2.3.2 Preliminary catalytic tests

Preliminary catalytic tests were carried out on the reaction of nitrobenzene reduction at room temperature (RT) using 15Cu/SS_pr as catalyst and sodium borohydride ($NaBH_4$) as hydrogen donor. Three different solvents were also tested: diethyl ether ($Et_2O$), a 1:1 mixture of diethyl ether and deionized water ($Et_2O/H_2O$) and deionized water ($H_2O$). As it can be seen from Table 2.3, the reaction proceeds significantly faster in water due to the high solubility of sodium borohydride in polar solvents. For this reason, water was chosen as the solvent for the subsequent reactions.

Table 2.3. Preliminary catalytic tests for the reduction of nitrobenzene

| Entry | Catalyst weight, mg | Solvent | Volume, ml | $NaBH_4$, mmol | Time, h | Yield, % |
|-------|--------------------|---------|-----------|----------------|---------|----------|
| 1 | 100 | $Et_2O$ | 5 | 10 | 6 | 64 |
| 2 | 100 | $Et_2O$ | 5 | 10 | 12 | 98 |
| 3 | 100 | $Et_2O/H_2O$ | 5/5 | 10 | 6 | 73 |
| 4 | 100 | $Et_2O/H_2O$ | 5/5 | 10 | 12 | 95 |
| 5 | 100 | $Et_2O/H_2O$ | 2.5/2.5 | 10 | 6 | 98 |
| 6 | 100 | $H_2O$ | 5 | 10 | 6 | >99 |
| 7 | 100 | $H_2O$ | 5 | 5 | 3 | >99 |

Then catalyst and $NaBH_4$ loading were varied to determine the optimum reaction conditions (Table 2.4).

Table 2.4. Optimization of reaction conditions

| Entry | Catalyst weight, mg | NaBH₄, mmol | Time, h | Yield, % |
|-------|--------------------|-------------|---------|----------|
| 1 | 100 | 5 | 3 | >99 |
| 2 | 50 | 5 | 3 | >99 |
| 3 | 30 | 2 | 1 | 33 |
| 4 | 50 | 2 | 1 | 42 |
| 5 | 30 | 2 | 3 | 51 |
| 6 | 30 | 1 | 1 | 34 |
| 7 | 50 | 3 | 1 | 51 |
| 8 | 50 | 3 | 2 | >99 |
| 9 | 30 | 3 | 2 | 18 |
| 10 | 40 | 2 | 2 | 66 |
| 11 | 40 | 3 | 2 | 79 |

The optimal reaction conditions were established: 0.5 mmol of nitrobenzene reacted in presence of 50 mg of catalyst, 3 mmol $NaBH_4$ in 5 ml $H_2O$ during 2 h at RT.



$NO_2$ → $NH_2$

50mg Cu/SteelSlags prec.
3 mmol $NaBH_4$

5ml $H_2O$
RT, 2h
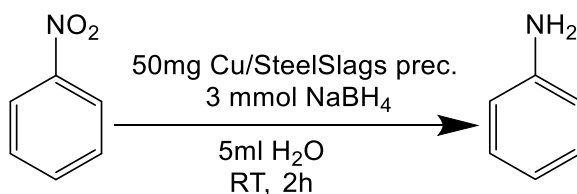
Scheme 2.4 Optimal reaction condition

After determining the optimal reaction conditions for 15Cu/SS_prec, the following catalysts were tested under the optimal condition.

Table 2.5. Catalytical test for different catalyst (reaction conditions reported in Scheme 2.4)

| Entry | Catalyst | Catalyst weight, mg | NaBH₄, mmol | Time, h | Yield, % |
|-------|----------|---------------------|-------------|---------|----------|
| 1 | Steel Slags | 50 | 3 | 2 | 0 |
| 2 | 10Cu/SS_pr | 75 | 3 | 2 | 59 |
| 3 | 10Cu/SS_calc | 75 | 3 | 2 | 64 |
| 4 | 10Cu/SS_NaBH₄ | 75 | 3 | 2 | 79 |
| 5 | 15Cu/SS_pr | 50 | 3 | 2 | >99 |

| Entry | Catalyst | Catalyst weight, mg | NaBH$_4$, mmol | Time, h | Yield, % |
|---|---|---|---|---|---|
| 6 | 15Cu/SS_calc | 50 | 3 | 2 | >99 |
| 7 | 15Cu/SS_NaBH$_4$ | 50 | 3 | 2 | >99 |
| 8 | 20Cu/SS_pr | 37.8 | 3 | 2 | >99 |
| 9 | 20Cu/SS_calc | 37.8 | 3 | 2 | >99 |
| 10 | 20Cu/SS_NaBH$_4$ | 37.8 | 3 | 2 | >99 |
| 11 | 15Cu/SS_pr_15h | 50 | 3 | 2 | 94 |
| 12 | 15Cu/SS_pr_u.s. | 50 | 3 | 2 | 43 |

As can be seen from the Table 2.5, Steel Slag doesn't demonstrate catalytic activity in the nitrobenzene reduction process. For samples containing different amounts of copper (10, 15 and 20 %), the mass of catalyst for the reaction was taken proportionally based on the calculated Cu content. For those catalysts containing 10% copper, the lowest activity was found, due to the pH being too high (>12) in the precursor synthesis process, thus affecting the formation of particles of the active component. Besides, increasing the synthesis time of the catalyst in case 15Cu/SS_pr_15h a bit decreased in activity, whereas pretreatment of the steel slag solution with ultrasound more significantly decreased the activity of the catalyst in the test reaction.

To determine the difference for catalysts with different concentrations, 10Cu/SS_pr, 15Cu/SS_pr and 20Cu/SS_pr catalyst precursors were additionally tested for one hour (Table 2.6).

Table 2.6. Catalytical test for catalysts with different concentrations (reaction conditions reported in Scheme 2.3)

| Catalyst | Catalyst weight, mg | NaBH$_4$, mmol | Time, h | Yield, % |
|---|---|---|---|---|
| 10Cu/SS_pr | 75 | 3 | 1 | 32 |
| 15Cu/SS_pr | 50 | 3 | 1 | 51 |
| 20Cu/SS_pr | 37.8 | 3 | 1 | 63 |

To evaluate the effect of reduction method on catalytic activity, precursor without pre-reduction, catalyst reduced in H$_2$ atmosphere at 300°C were tested in reaction for one hour. Thus, the yield of the aniline in the reaction with H$_2$ reduced catalyst was

only a bit higher compared to the sample without preliminary reduction. This is probably due to the formation of larger copper particles caused by the high temperature.

Table 2.7 Catalytical test for catalyst with different reduction method (reaction conditions reported in Scheme 1)

| Catalyst | Catalyst weight, mg | NaBH$_4$, mmol | Time, h | Yield, % |
|---|---|---|---|---|
| 15Cu/SS_pr | 50 | 3 | 1 | 47 |
| 15Cu/SS_NaBH$_4$ | 50 | 3 | 1 | 71 |
| 15Cu/SS_calc | 50 | 3 | 1 | 51 |

Since the difference in activity between the catalyst pre-reduced by NaBH$_4$ and the unreduced precursor is only 20%, the expense of time and sodium borohydride for pre-reduction was not justified. Based on the above results, 15%Cu/SteelSlags_prec. resulted the most effective among the series of catalysts synthesized. In further testing and characterization this sample will be referred to as Cu/SteelSlags precursor.

In the case of catalyst precursors, the reduction of $Cu^{+2}$ to the active form $Cu^0$ occurred under the presence of hydrogen produced by NaBH$_4$ in the reaction conditions. In this case, the visual change indicating the phase transition of the copper ions occurred in two stages (Fig. 2.9). In the first stage, the grey particles of the catalyst precursor changed the color of the solution to brown, associated with the formation of fresh $Cu^0$ particles [115, 116]. After some time, the particles agglomerated into larger particles with a color change to black and the reaction mixture became transparent again.
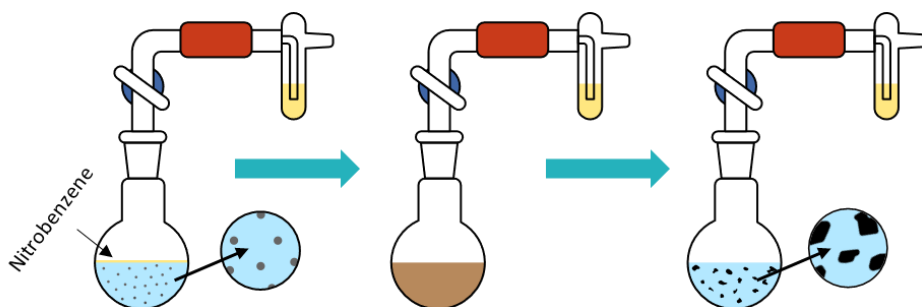


Fig. 2.9 Reduction of $Cu^{2+}$ to $Cu^0$ during reaction with Cu/SteelSlags catalyst precursor

### 2.3.3 Recyclability test

Recyclability test was carried out at room temperature in round flask equipped with a magnetic stirrer and a gas bubbler in the presence of 2.0 mmol of nitrobenzene, 6.0 mmol of $NaBH_4$, 200 mg of Cu/SteelSlags catalyst precursor and 10 ml of $H_2O$. After each cycle of reaction, the catalyst was washed 3 times with distilled water and methanol, and dried at 80°C and used for a subsequent run. As can be seen from the diagram (Fig. 2.10), the catalyst showed maximum product yield over two reaction cycles with a slight decrease in activity to 97% over the next three cycles.
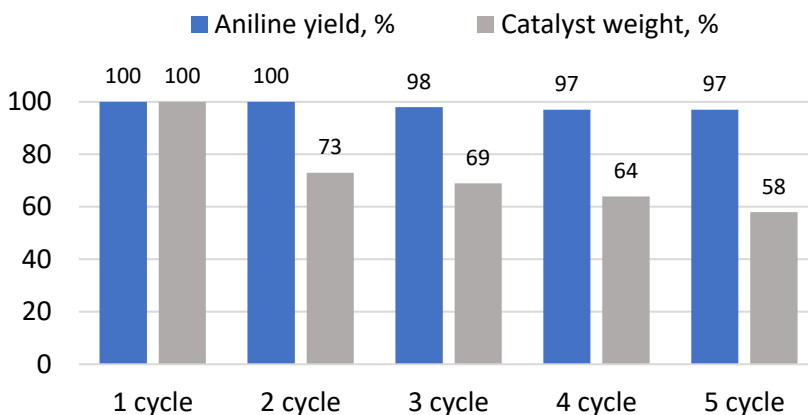


Fig. 2.10 Results of cycling test during 5 cycles of nitrobenzene reduction

The significant mass loss 27% after the first cycle is attributed to the process of copper reduction from hydroxides and carbonates. In addition, besides the active component, $NaBH_4$ is able to reduce sulphates in the catalyst precursor, which also reduces the mass of the catalyst. The subsequent mass reduction after each cycle was less significant and related to the recovery procedures.

### 2.3.4 Hydrogenation of nitroarenes
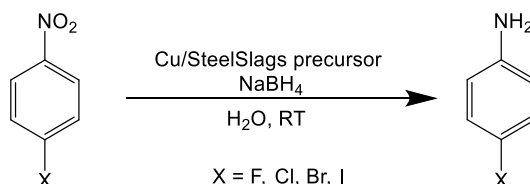


Scheme 2.5 Reduction of halo-nitoarenes catalyzed by Cu/SteelSlags precursor

Table 2.8 Reduction of halo-nitroarenes catalyzed by Cu/Steel Slags precursor

| Entry | Substrate | Product | Time, h | Yield, % |
|---|---|---|---|---|
| 1 | 4-Fluoronitrobenzene | 4-Fluoroaniline | 2 | >99 |
| 4 | 4-Chloronitrobenzene | 4-Chloroaniline | 3 | >99 |
| 3 | 4-Bromonitrobenzene | 4-Bromoaniline | 4 | >99 |
| 4 | 4-Iodonitrobenzene | Aniline | 2 | >99 |

The nature of the halogen has a significant effect on the reaction rate. For the most commonly iodinated nitroarenes, hydrodehalogenation is significantly more rapid than for Br, Cl or the less reactive F [108]. Therefore, the reduction of 4-iodonitrobenzene occurred significantly faster, but with low selectivity. Noticeable 4-Fluoronitrobenzene was also rather quickly reduced to the corresponding amine, which may be related to the liquid state of the substrate and, consequently, to the larger contact area in the two-phase system.

Furthermore, catalyst was tested in reduction reactions of various substituted nitroarenes (Scheme 2.6).
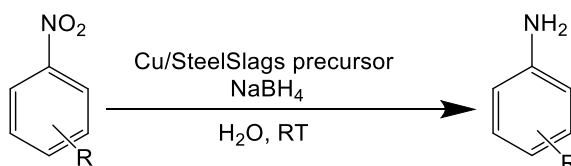


Scheme 2.6 Reduction of nitoarenes catalyzed by Cu/SteelSlags precursor

As can be seen from the Table 2.9, the Cu/Steel Slags precursor demon-strated high activity in the reduction of nitroarenes independent of the substituted group and its position.

Table 2.9 Hydrogenation of nitroarenes catalyzed by Cu/Steel Slags precursor

| Entry | Substrate | Product | Time, h | Yield, % |
|---|---|---|---|---|
| 1 | 2-Nitrotoluene | 2-toluidine | 1 | >99 |
| 2 | 3-Nitrotoluene | 3-toluidine | 2 | >99 |
| 3 | 4-Nitrotoluene | 4-toluidine | 2 | >99 |

| Entry | Substrate | Product | Time, h | Yield, % |
|-------|-----------|---------|---------|----------|
| 4 | 2-Nitroanisole | 2-anisidine | 2 | >99 |
| 5 | 3-Nitroanisole | 3-anisidine | 2 | >99 |
| 6 | 4-Nitroanisole | 4-anisidine | 2 | >99 |
| 7 | 1,2-Dinitrobenzene | 1,2-Diaminobenzene | 2 | 51 |

## 2.4. Characterization of Cu/Steel Slag catalysts

### 2.4.1 Elemental analysis

Elemental composition analyses of the steel slag, the Cu/steel slag precursor and the catalyst after the cycles were determined using the PXRF method. Table 2.10 demonstrates calcium content is almost halved (from 28.9% to 15.97%) during the synthesis of the catalyst precursor. It is related to the exchange and substitution reactions that occur during the interaction of steel slag and copper sulphate. In addition, the calcium content continues to decrease slightly during the use of the catalyst. This may be due to leaching of calcite during the reaction process. Significantly, the copper content increases slightly.

Table 2.10 Results of PXRF analysis

| Content, %w | Steel Slags | Cu/Steel Slags precursor | Cu/Steel Slags after 1 cycle | Cu/Steel Slags after 5 cycles |
|-------------|-------------|--------------------------|------------------------------|-------------------------------|
| Ca | 28.90 ± 2.22 | 15.97 ± 0.94 | 15.88 ± 0.16 | 10.45 ± 0.30 |
| Fe | 17.62 ± 2.03 | 14.06 ± 0.68 | 17.37 ± 0.22 | 17.64 ± 0.82 |
| Si | 3.36 ± 0.16 | 1.81 ± 0.17 | 2.89 ± 0.04 | 3.06 ± 0.02 |
| Mn | 4.44 ± 0.45 | 3.64 ± 0.20 | 4.39 ± 0.06 | 4.28 ± 0.15 |
| Cl | 0.72 ± 0.06 | 0.12 ± 0.01 | 0.08 ± 0.00 | 0.10 ± 0.00 |
| Ti | 0.14 ± 0.02 | 0.11 ± 0.01 | 0.15 ± 0.01 | 0.15 ± 0.01 |
| Cr | 0.09 ± 0.01 | 0.05 ± 0.00 | 0.08 ± 0.00 | 0.07 ± 0.00 |
| S | - | 5.87 ± 0.17 | 0.53 ± 0.03 | 0.20 ± 0.02 |
| Cu | - | 13.65 ± 0.75 | 14.13 ± 1.32 | 15.98 ± 1.19 |

### 2.4.2 FT-IR analysis

The FT-IR spectra of steel slags, the Cu/Steel Slags precursor, the Cu/Steel Slags catalyst after 1 cycle, and the Cu/Steel Slags catalyst after 5 cycles were analyzed in the range of 400 to 4000 cm-1 and are illustrated in Fig. 2.11.
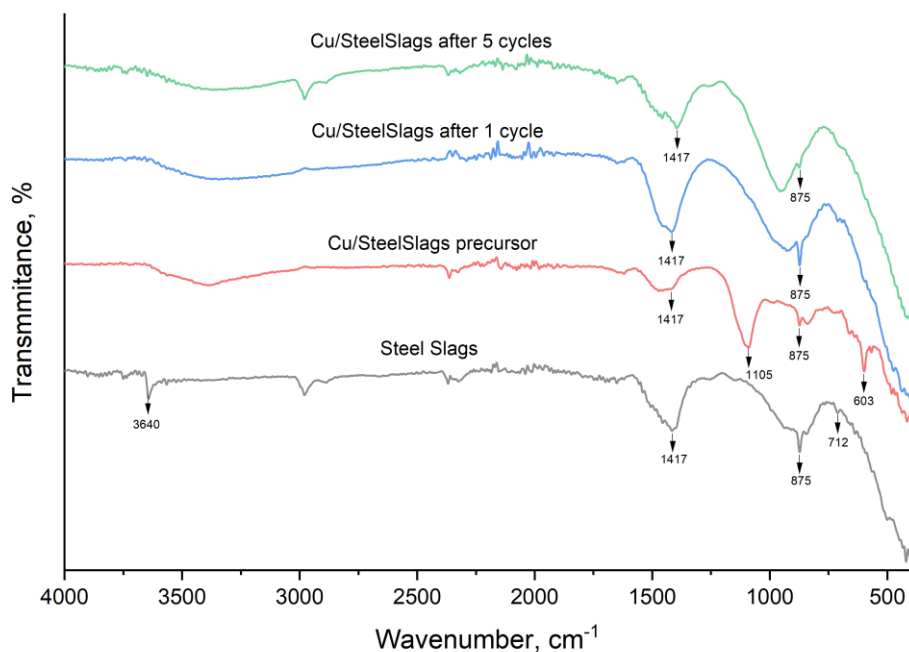


Fig. 2.11 Comparison of FT-IR spectra of Steel Slags (black), Cu/Steel Slags precursor (red), Cu/Steel Slags catalyst after 1 cycle (blue), Cu/Steel Slags catalyst after 5 cycles (green)

Peaks related to steel slag are described in detail in Chapter 2.1. For all four samples absorption band at 1417 cm$^{-1}$ is attributed to the C—O bond, and peak at 875 cm$^{-1}$and correspond to vibrations of the $CO_3^{2-}$ ion in calcite [91, 92]. In addition, two unique peaks observed for Cu/SS precursor. Intense peak at 1105cm$^{-1}$ applies vibration of S–O [117,118] to indicates the formation of a gypsum phase during the reaction (2.7). Second peak at 603 cm$^{-1}$ due vibration of Cu–O demonstrates the presence of the CuO phase [119, 120]. However, this peak is absent in samples after the catalytic reaction, which may indicate for full reduction of copper oxide to copper nanoparticles by $NaBH_4$ during the rection cycles.

42

### 2.4.3 Phase composition

The XRD diffractograms of Steel Slag, Cu/Steel Slags precursor and Cu/Steel Slags catalyst after 1 cycle are presented in Fig.2.12.
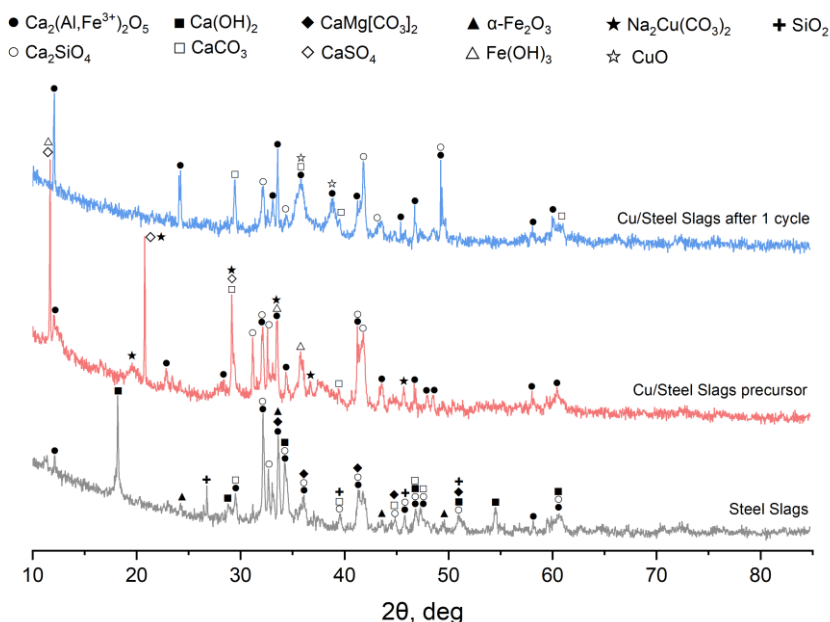


Fig. 2.12 XRD patterns of Steel Slags (black), Cu/Steel Slags precursor (red) and Cu/Steel Slags after 1 cycle (blue)

Larnite and Brownmillerite are the solid base of the catalyst and retained after the addition of Cu. However, diffractogram exhibits the absence of discernible peaks corresponding to crystalline $Cu^0$, CuO, and CuOH phases. This, coupled with a high degree of background noise, suggests these phases are present in an amorphous form. The amorphous nature of these phases is likely attributed to the significant concentration of CaO and CaOH within the steel slag matrix, which may hinder the formation of ordered crystalline structures. [121] In the case of the Cu/Steel Slags precursor, the formation of 3 new phases is observed.  Thus, the formation of gypsum ($CaSO_4$) occurs due to the reaction of sodium hydroxide with copper sulfate (2.7), which is also consistent with the FTIR results. A Juangodoyite ($Na_2Cu(CO_3)_2$) phase 2was also detected, which could have been formed during a complex reaction (2.9):

$$2NaOH + CaMg(CO_3)_2 + CuSO_4 \rightarrow CaSO_4 + Na_2Cu(CO_3)_2 + Mg(OH)_2 \qquad (2.9)$$
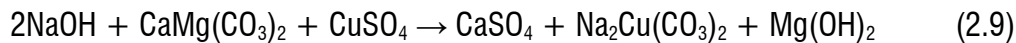
The phase composition of the three samples described above is summarized in Table 2.11.

Table 2.11 The presence of phases in the catalysts

| Phase | Formula | Steel Slags | Cu/SteelSlags precursor | Cu/SteelSlags after 1 cycle |
|---|---|---|---|---|
| Larnite | $Ca_2SiO_4$ | + | + | + |
| Brownmillerite | $Ca_2(Al,Fe^{3+})_2O_5$ | + | + | + |
| Calcite | $CaCO_3$ | + | + | + |
| Portlandite | $Ca(OH)_2$ | + | - | - |
| Dolomite | $CaMg(CO_3)_2$ | + | - | - |
| Quartz | $SiO_2$ | + | - | - |
| Hematite | $\alpha\text{-}Fe_2O_3$ | + | - | - |
| Gypsum | $CaSO_4 \cdot 2H_2O$ | - | + | - |
| Iron (III) Hydroxyde | $Fe(OH)_3$ | - | + | - |
| Juangodoyite | $Na_2Cu(CO_3)_2$ | - | + | - |
| Tenorite | $CuO$ | - | - | + |

### *2.4.4 EDX-mapping*

From the EDX mapping images it can be assumed that larnite is the main carrier, since the dislocation of copper particles coincides with the dislocation zones of Ca, Si and O. The Cu/SteelSlags precursor EDX images (Fig. 2.13) indicate the presence of sulfur, thus confirming the presence of the gypsum phase. However, no sulfur was detected for samples recovered after the first and fifth catalytic cycles, confirming the FTIR data on the transformation of copper sulfate to sodium sulfate (2.8), followed by removal during washing.
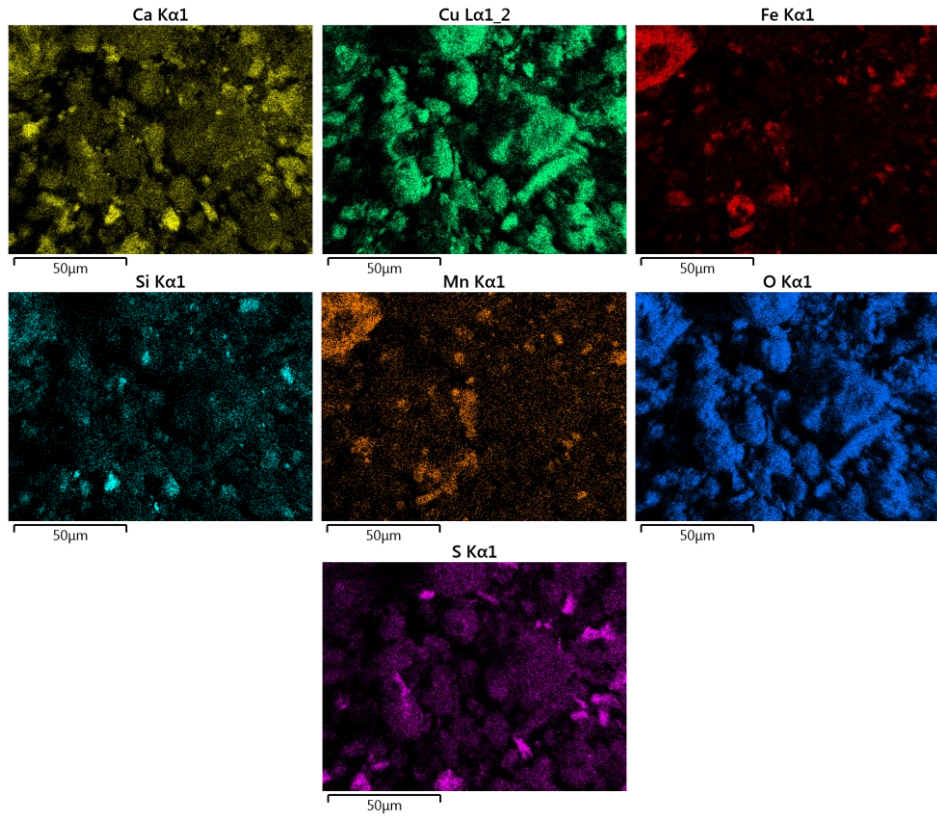
Fig. 2.13 EDX-mapping of Cu/Steel Slags precursor
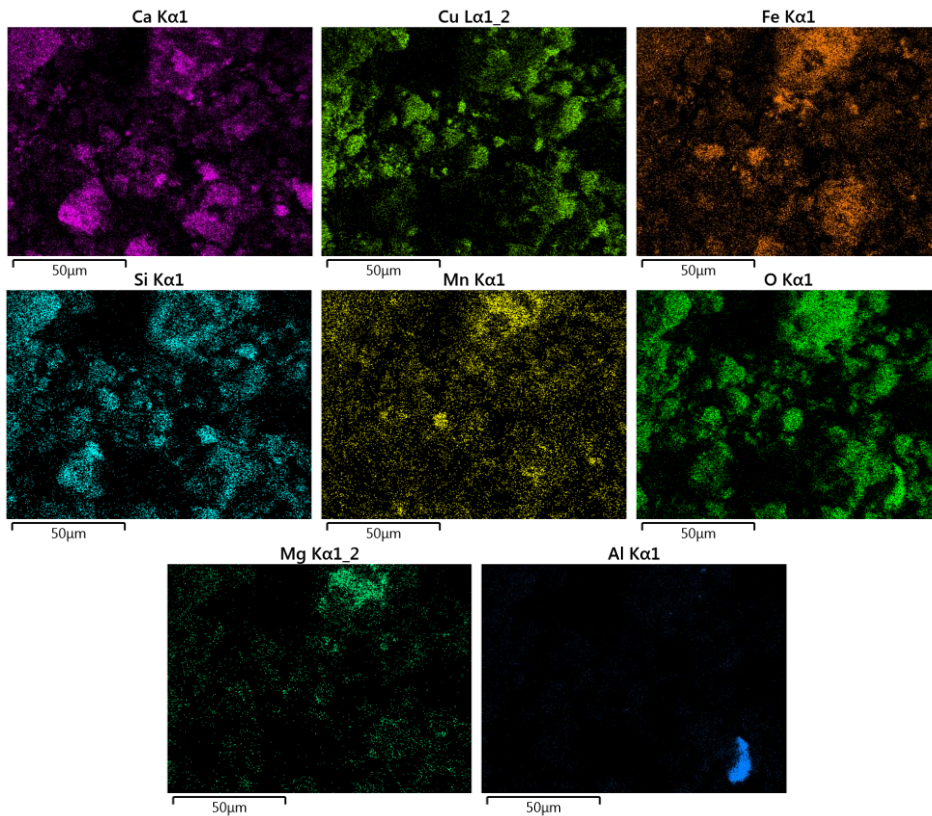
Fig. 2.14 EDX-mapping of Cu/Steel Slags catalyst after 1 cycle
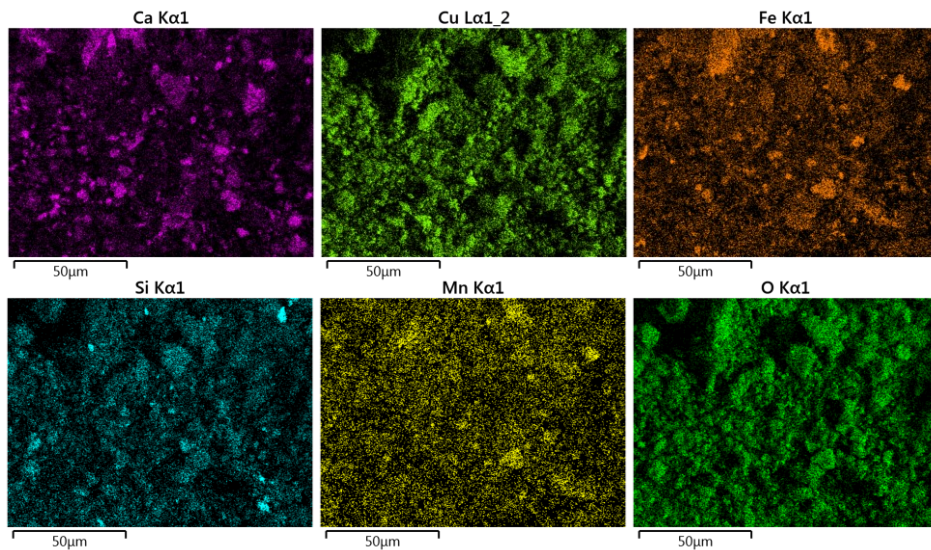


Fig. 2.15 EDX-mapping of Cu/Steel Slags catalyst after 5 cycles

*2.4.5 Thermogravimetric analysis*

The samples were analyzed by TGA under $N_2$ atmosphere at a temperature range of 25-1000°C and a heating rate of 10°C/min. In the TGA-DC-DTG curves (Fig. 2.16) of the Cu/SteelSlags precursor, five DTG peaks are clearly distinguished. The first DTG peak at 124°C corresponds to the dehydration of gypsum [122, 123] with a mass loss of 2%. Temperature peak at 209°C belongs to the conversion of $Cu(OH)_2$ to CuO [124, 125]. The weak peak at 362°C most likely represents the decomposition of $Mg(OH)_2$ [126, 127] formed during the reaction (2.9). The peak at 631°C is attributed to the decomposition of $CaCO_3$ [95, 96, 97] in reaction (2.3), confirming the FTIR and XRD data on the retention of the calcite phase after copper deposition. The peak at 748°C is probably related to the $Na_2Cu(CO_3)_2$ phase detected by XRD analysis. The last peak at 984°C indicates the transformation of the copper crystal lattice.

$$CaSO_4 \cdot 4H_2O \rightarrow CaSO_4 \cdot 0.5H_2O + 3.5H_2O \qquad (2.10)$$
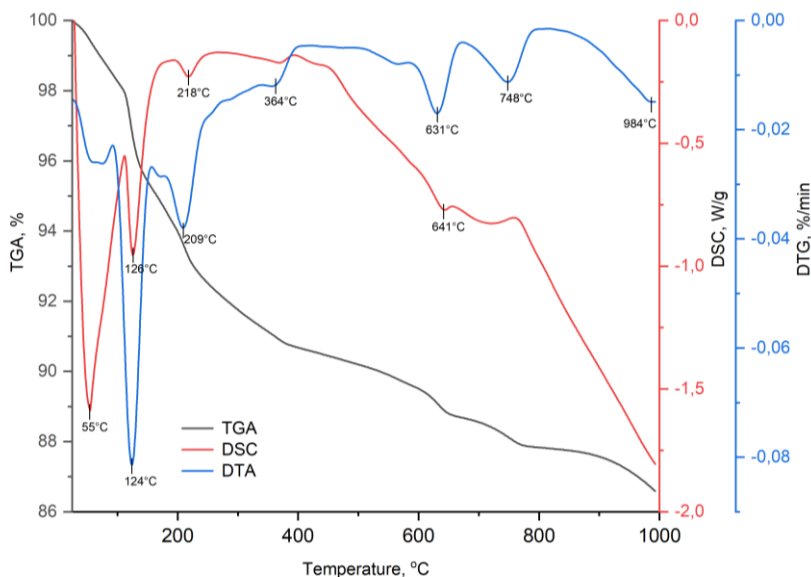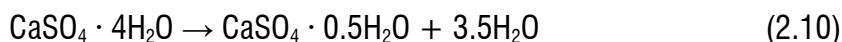


Fig. 2.16 TGA-DSC-DTG curves of Cu/Steel Slags precursor before reaction

Thermal analysis of the catalyst after one (Fig. 2.17) and five (Fig. 2.19) cycles shows a similar situation. After reduction of all hydroxides and sulphates by sodium

borohydrate, peaks corresponding to CaCO$_3$ at 630$^o$C and metallic copper at 984$^o$C are observed.
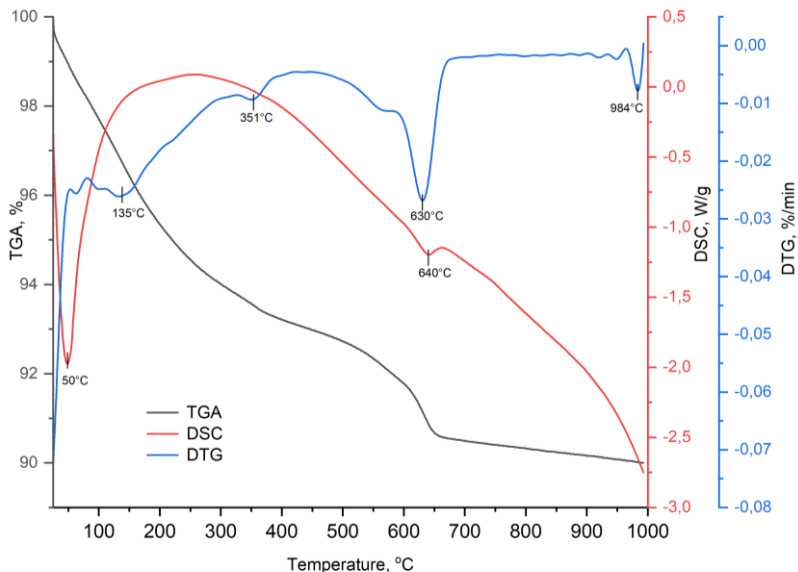


Fig. 2.17 TGA-DSC-DTG curves of Cu/Steel Slags catalyst after first cycle
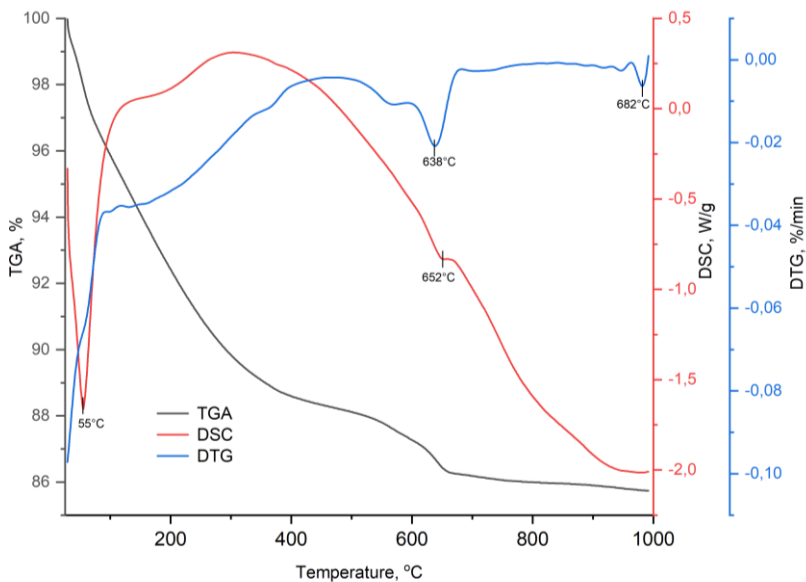


Fig. 2.18 TGA-DSC-DTG curves of Cu/Steel Slags catalyst after fifth cycle

## 2.4.6 Scanning electron microscopy

Based on the results of FESEM (Fig. 2.19), the Cu/SteelSlags precursor and catalysts after use in catalysis retain their morphology of heterogeneous material with wide range size of the particles covered white flat flakes, most probably calcite.
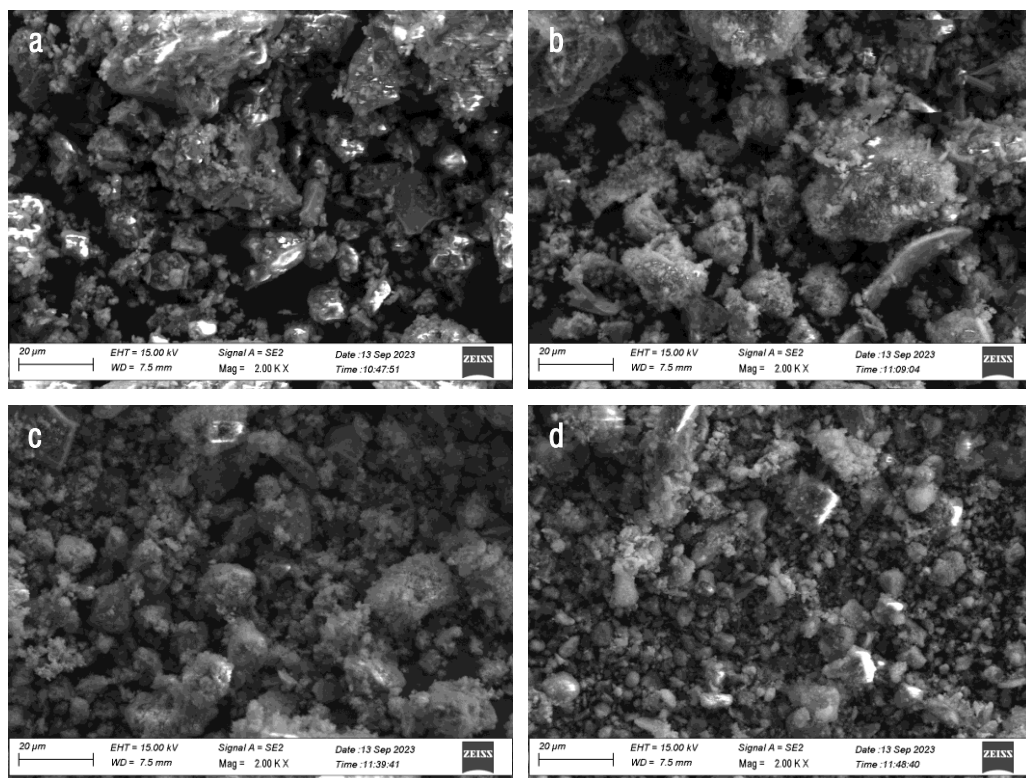


Fig. 2.19. FESEM graphs of a – Steel Slags, b – catalyst precursor before reaction, c – catalyst after first cycle, d – catalyst after fifth cycle

## 2.4.7 Transmission electron microscopy

Figure 2.20 illustrates transmission electron microscopy (TEM) images of the Cu/steel slags precursor (a, b), the Cu/steel slags catalyst after one cycle (c, d), and after five cycles (e, f). The images of the Cu/SteelSlag precursor demonstrate the formation of elongated particles, which are presumed to be Cu(OH)$_2$ or gypsum. During the reduction process under the specified reaction conditions, Cu nanoparticles are

formed and attached to the steel slag support (Fig. 2.18 c, d) and persist throughout the five cycles (Fig. 2.19 e, f).
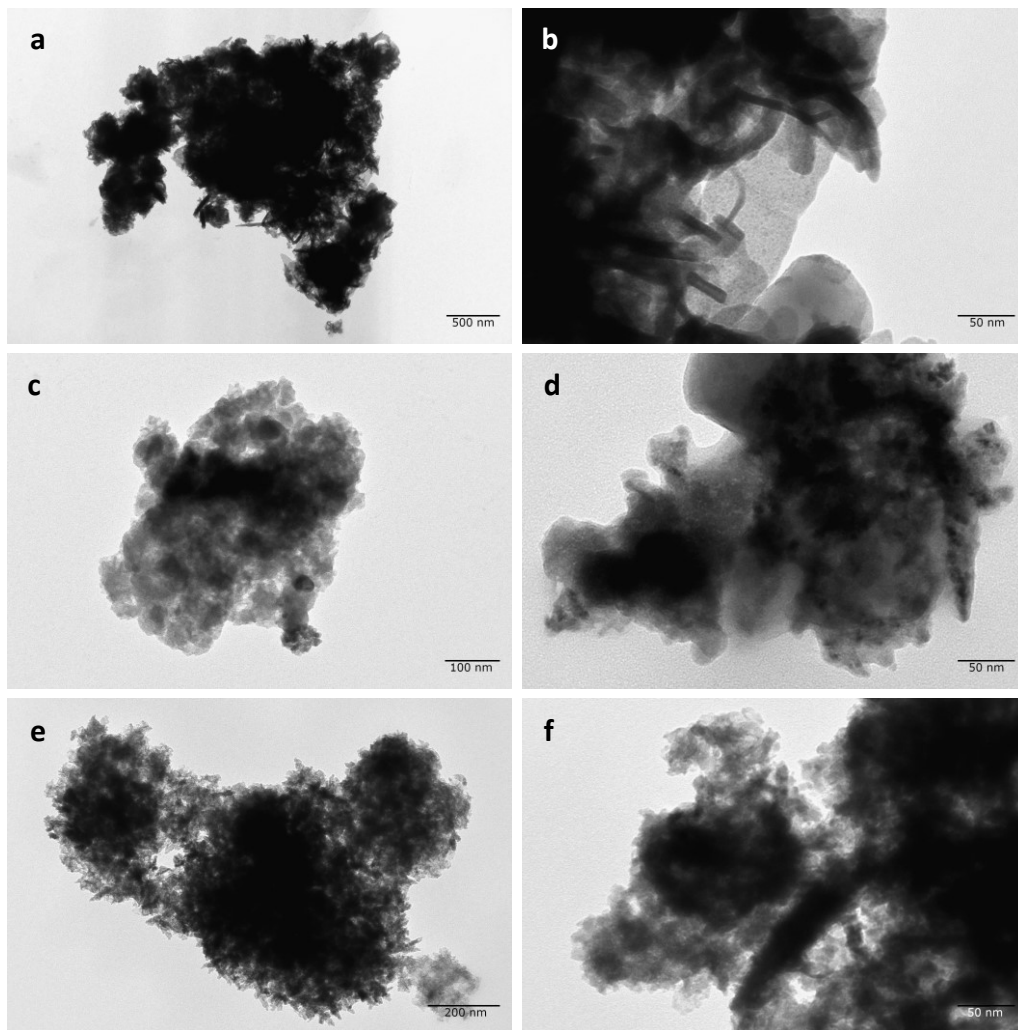


Fig.2.20 TEM micrographs of a, b – Cu/Steel Slags precursor; c, d - Cu/Steel Slags catalyst after first cycle; e, f - Cu/Steel Slags catalyst after fifth cycle

### 2.5. Synthesis Iron Oxides/Steel Slags catalyst

Iron oxides as an inexpensive and common catalyst also show catalytic activity in reduction of nitroarenes. The use of iron oxide catalysts in the reaction of transfer hydrogenation of nitroarenes in the presence of alkali/alcohol system is a perspective direction of research.

Alcohols (methanol, ethanol, isopropanol and glycerol) in combination with basic media are effective reducing agents in the reduction reactions of nitroarenes. Under certain reaction conditions, alkali/alcohol vapours are able to smoothly reduce nitroarenes to anilines in the absence of a catalyst, together with variable amounts of azo- and azoxyarenes [108]. A disadvantage of this hydrogen source is the amount of alkali component, which is molarly greater than the amount of nitro compound [128].

Isopropanol is adsorbed on the catalyst, resulting in the formation of an alkoxide, also known as an activated H-donor. Moreover, the coordination interaction of nitroarenes with the Lewis acid center enables the formation of a six-membered transition state, in which hydride transfer occurs (Scheme 2.7). Concurrently, the presence of base facilitates the transfer of the alkoxide hydride ion for substrate reduction [129].
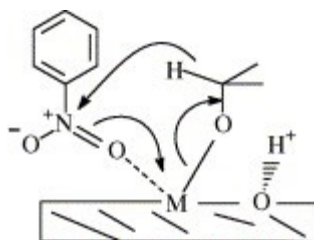


Scheme 2.7 Proposed catalytic pathway for the alkali/alcohol reduction system

Since steel slag and FeOx/SS catalysts are rich in components with alkaline properties, it is possible to use them in the transfer hydrogenation reaction without additional alkali additives, which makes the process more economically and environmentally efficient.

$FeCl_3 \cdot 6H_2O$ and $FeSO_4 \cdot 7H_2O$ were mixed in 2/1 molar ratio in 50 mL of deionized water and the obtained solution was added to 3.0 g of SS (80 mesh sieved) and kept under stirring for 5 h at 35 °C. Then, the solid constituted of steels slags supporting

iron hydroxides/oxides was separated by centrifugation at 4000 rpm, washed three times with deionized water and dried overnight at 80 °C. As a result, a series of iron oxide catalysts supported onto steel slags (FeOx/SS_1÷6) was synthesized. The total molar amount of added iron salts (as $FeCl_3 \cdot 6H_2O + FeSO_4 \cdot 7H_2O$) ranged from 2.0 mmol for FeOx/SS_1 to 16.7 mmol for FeOx/SS_6 (Table 2.12). The basicity of the resulting material decreased with the increase of the supported iron as summarized in Table 2.12.

Table 2.12 Synthesized iron oxides/Steel Slags catalysts

| Catalyst | $FeCl_3 \cdot 6H_2O + FeSO_4 \cdot 7H_2O$, mmol | pH* |
|----------|------------------------------------------------|------|
| FeOx/SS_1 | 2.0 | 12.4 |
| FeOx/SS_2 | 4.3 | 11.6 |
| FeOx/SS_3 | 6.9 | 10.8 |
| FeOx/SS_4 | 9.6 | 10.2 |
| FeOx/SS_5 | 13.0 | 6.5 |
| FeOx/SS_6 | 16.7 | 5.3 |

*pH of the catalyst was determined by analyzing the liquid separated after centrifugation

## 2.6. Catalytic test of Iron Oxides/SteelSlags catalyst in transfer hydrogenation of nitrobenzene

The catalysts listed in Table 2.12 were tested in the transfer hydrogenation of nitrobenzene, using *iso*-propanol as hydrogen source and without adding any external base. Reactions were carried out in an autoclave at 180 °C for 12 h by using 0.50 mmol nitrobenzene, 5 mL of *iso*-propanol and 250 mg of catalyst (Scheme 2.8). The main product was always aniline together with a small amount of azoxybenzene, suggesting the presence of the condensation route in the mechanism pathway (Scheme 2.2, blue route). Also trace amounts (<1%) of azobenzene were detected in all catalytic tests.
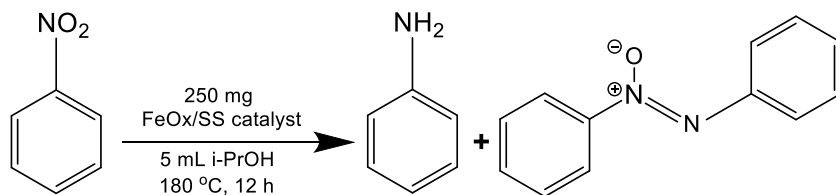
Scheme 2.8. Reaction of transfer hydrogenation of nitrobenzene

As-received steel slags, despite the high content of iron oxides and basic oxides, showed low activity in the reaction. In the series of the analyzed catalysts, the catalytic activity increased with the increase of the iron content passing from FeOx/SS_1 to FeOx/SS_3 (Fig. 2.21). In fact, the maximum conversion (88%) of nitrobenzene was observed for FeOx/SS_3. By analyzing the catalytic results of FeOx/SS_4 to FeOx/SS_6 catalysts, the higher the iron content in the material the lower the activity. A rationale for this behavior may reside in the increasing acidity of the material that renders it unable to support the transfer hydrogenation system.
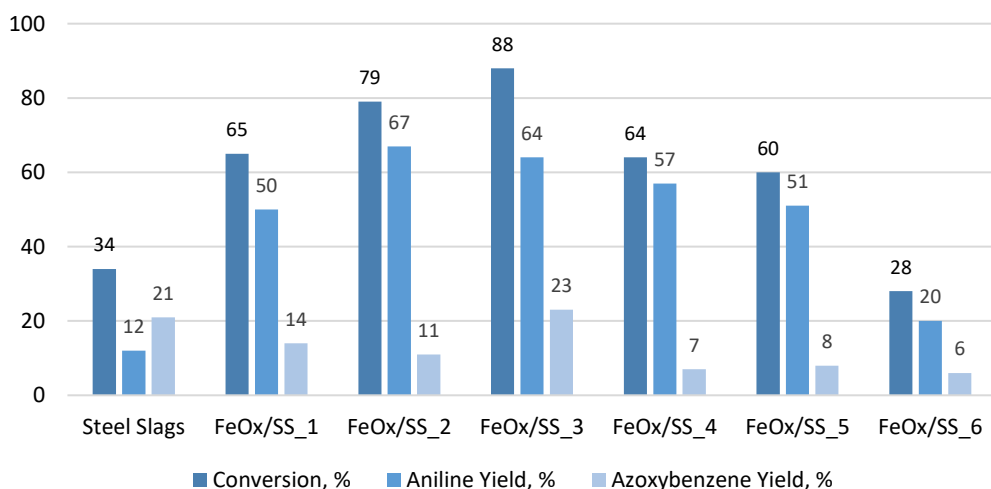


Fig. 2.21 Catalytical activity of FeOx/SS catalysts in transfer hydrogenation of nitrobenzene

The most efficient catalyst was tested prolonging the reaction time to 24 h. The conversion of nitrobenzene increased from 88% to 93%, while the yield of azoxybenzene decreased from 23% to 11% (Figure 2.22), indicating that doubling the reaction time only slightly improved the catalytic results.
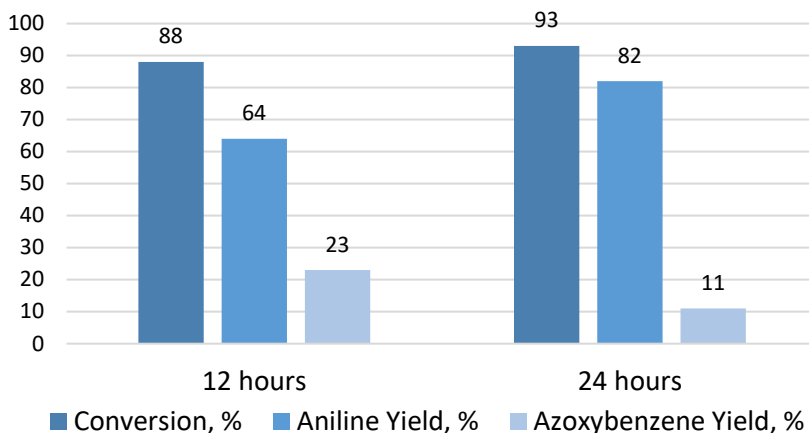
Fig. 2.22 Catalytical activity of FeOx/SS_3 catalyst during 12 and 24h of reaction

## 2.7. Characterization of Iron Oxides/SteelSlags catalyst

### 2.7.1 FT-IR analysis

The steel slag sample and a series of synthesized FeOx/SS catalysts were analyzed by FT-IR spectrometry in wavenumber range of 550 to 4000 $cm^{-1}$. As indicated by the FT-IR spectra (Fig. 2.23), the ratio of iron salts to steel slag and the subsequent pH during synthesis exert a significant influence on the formation of the catalyst. The steel slag peak at 1417 $cm^{-1}$, attributed to the C—O bond, and the peak at 875 $cm^{-1}$ correspond to vibrations of the $CO_3^{2-}$ ion in calcite [91, 92] are also observed in the four catalyst samples from FeOx/SS_1 to FeOx/SS_4 catalyst. In addition, a new peak at 1105 $cm^{-1}$ related to S-O vibrations [117, 118] is observed for the three catalyst samples with deposited iron oxides from 5% to 15%, with the peak intensity decreasing with increasing iron oxide content in the composition.
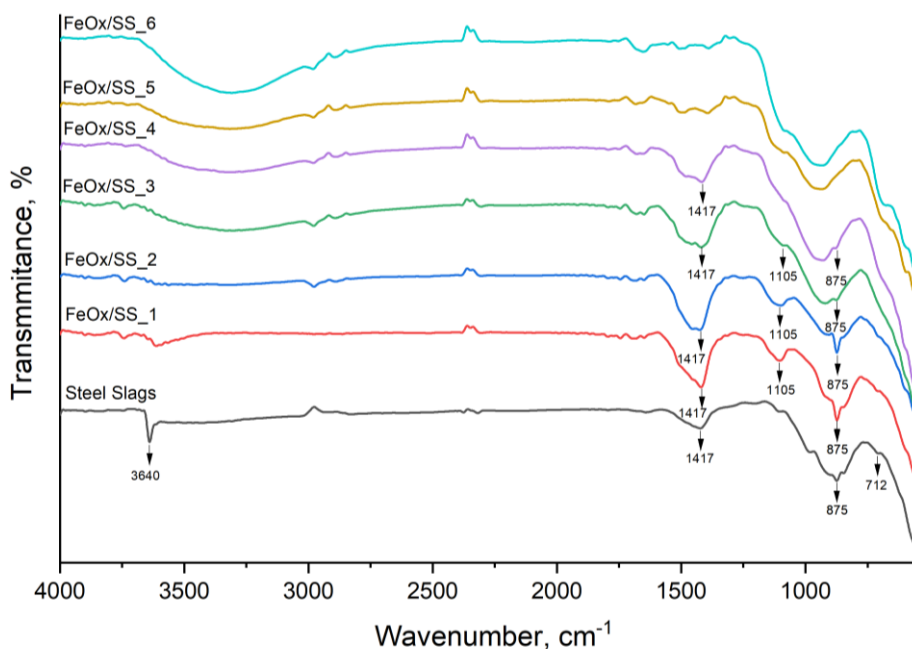
Fig. 2.23 FT-IR spectra of Steel Slags and FeOx/SS catalyst

## 2.7.2 Elemental analysis

The most active catalyst in the transfer hydrogenation reaction resulted FeOx/SS_3 because represented a good compromise between iron content and basicity features. Therefore, it was analyzed more deeply with respect to the other FeOx/SS catalysts. The elemental content of FeOx/SS_3 was determined by X-ray fluorescence analysis (Table 2.13). The percentage of iron content in the catalyst sample increased by 13.6% upon deposition of iron oxide, which corresponds to the calculated values. In addition, a half decrease in calcium concentration due to the dissolution and subsequent loss of portlandite $Ca(OH)_2$ during synthesis process was observed.

Table 2.13 Results of PXRF analysis of steel slags and FeOx/SS_3 catalyst

| Content, %$_w$ | Steel Slags | FeOx/SS_3 |
|---|---|---|
| Ca | 28.90 ± 2.22 | 14.24 ± 0.11 |
| Fe | 17.62 ± 2.03 | 31.24 ± 0.24 |
| Si | 3.36 ± 0.16 | 3.38 ± 0.09 |
| Mn | 4.44 ± 0.45 | 4.13 ± 0.05 |
| Cl | 0.72 ± 0.06 | 0.19 ± 0.01 |
| S | - | 1.25 ± 0.04 |

### 2.7.3 Phase composition

The XRD diffractograms of FeOx/SS_3 catalyst before and after use in catalysis are presented in Fig. 2.22. As in the case of Cu/Steel Slags catalysts, larnite ($Ca_2SiO_4$), brownmillerite ($Ca_2(Al,Fe^{3+})_2O_5$) and calcite ($CaCO_3$) as the base of steel slag (Fig. 2.2) are present in all analyzed samples. Furthermore, wüstite (FeO) can be identified in the FeOx/SS_3 diffractograms before and after use in catalysis. XRD analysis suggests that the composition of the catalyst was retained during the catalytic cycle.
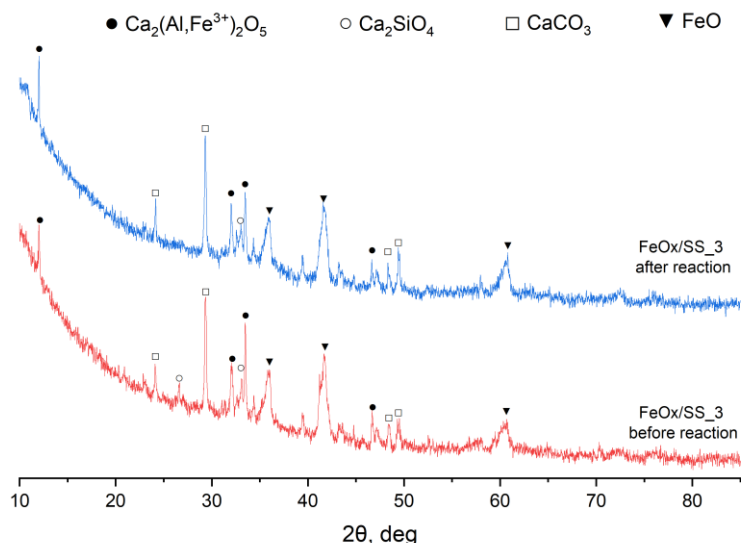


Fig. 3.24 XRD patterns of FeOx/SS_3 before reaction (red) and FeOx/SS_3 after reaction (blue)

## 2.8. Conclusions

A series of copper and iron oxide catalysts based on steel slag were synthesized in order to valorize the industrial steel slag waste.

The Cu/Steel Slags system demonstrated high activity in the reduction of nitroarenes in an aqueous medium, with the presence of sodium borohydride as the reducing agent. Notably, the reduction of nitrobenzene to aniline without the presence of additional impurities occurs within a two-hour period at RT. It resulted that the catalyst precursor did not require prior reduction, and that the conversion of $Cu^{2+}$ to $Cu°$ in the active form occurred "in situ" under reaction conditions. Furthermore, the catalytic system gave high yield into the desired product over five reaction cycles.

Iron oxides deposited onto waste steel slags were synthesized and employed in the catalytic transfer hydrogenation of nitrobenzene in the presence of isopropanol as the hydrogen source. This kind of reaction is challenging because it works with a green hydrogen source, but it usually requires the addition of toxic sodium or potassium hydroxide. Some of the materials prepared were able to successfully catalyze the reaction without adding any external base thanks to the high basicity of their inorganic support (steel slags).

# 3. RECOVERY OF CELLULOSE ACETATE FROM CIGARETTE BUTTS

## 3.1. Cigarette filters characterization

The waste cigarette butts were collected in special containers placed in the smoking areas of DICATECh department in Politecnico di Bari. Regular cigarette filters with the size of 15x7.5 mm (Smoking Filters, Spain) were used as a comparison sample to verify the cleaning efficiency.

### *3.1.1 FT-IR analysis*

Fig. 3.1 illustrates the results of FT-IR analysis of both fresh (black line) and used (red line) cigarette filters (CF), with a wavenumber range of 550 $cm^{-1}$ to 4000 $cm^{-1}$.
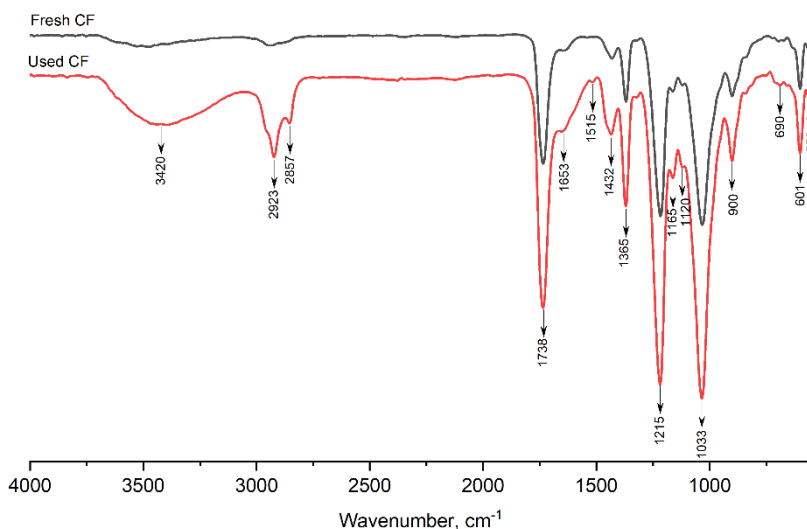


Fig. 3.1 FT-IR spectra of cigarette filters (CF): black line – fresh cigarette filter, red line – used cigarette filter

The broad absorption band observed at 3420 $cm^{-1}$, characteristic of O-H stretching in alcohols and/or N-H stretching in amines, is more pronounced in the used CF compared to the fresh CF. Such behavior suggests the introduction or enhancement

of hydroxyl groups, likely due to increased water content. The peaks at 2923 cm$^{-1}$ and 2857 cm$^{-1}$ correspond to C–H stretching vibrations, commonly found in aldehydes or hydrocarbons. The stronger absorption in these regions in the used CF spectrum compared to the fresh CF, indicates increased aliphatic hydrocarbon content or potential oxidation processes during burning of tobacco. A peak around 1738 cm$^{-1}$ corresponds to the C=O stretching of carbonyl groups is evident in both samples, but intensity for used sample quite bigger, due to growing of esters or ketones amount. In 1653 cm$^{-1}$ region, indicative of C=C stretching in alkenes, both spectra show similar intensity, indicating minimal changes in the unsaturated components. Small peak at 1515 cm$^{-1}$ for N=O stretching in nitro compounds is present just in used filter, which indicates degradation of nitro-containing compounds. The peak at 1365 cm$^{-1}$, corresponding to S=O stretching in sulphonamides or sulphates, appears slightly more intense in the used CF.

Noticeable changes between the fresh and used samples are evident withing the peaks at 1215 cm$^{-1}$ and 1033 cm$^{-1}$. This phenomenon primary associates with C–N symmetric stretching in amines and C–O stretching in esters. However, the increased intensity in the used CF could point to the formation esters or amines as a result of tobacco combustion. Lower wavenumber regions, such as 900 cm$^{-1}$ (C=C bending) and 601 cm$^{-1}$ (C–N–S bending), also display differences after using of CF. Moreover, the region around 556 cm$^{-1}$, characteristic of C-X stretching in alkyl halides, exhibits minimal variation.

Table 3.1 Transcript of ATR-FT spectra of used cigarette filters [130]

| Wavenumber, cm$^{-1}$ | Assignment |
|---|---|
| 3490–3250 | O–H in alcohols and N–H stretching in amines |
| 2960–2910 | N–H stretching in amine salts |
| 2857 | C–H stretching in aldehyde (doublet) |
| 1738 | C=O stretching in cyclopentane |
| 1685 | C=O stretching in conjugated ketone |
| 1653 | C=C stretching in alkene (vinyldiene) |
| 1515 | N–O stretching in nitro-compounds |
| 1432 | C–H bending in methyl group |

| Wavenumber, cm$^{-1}$ | Assignment |
|---|---|
| 1365 | S=O stretching in sulphonamide, sulphonate, sulphate, suphonyl chloride |
| 1215 | C–N symmetric vibrations in amines |
| 1165 | C–O stretching in ester |
| 1120 | C–O stretching in tertiary alcohol |
| 1033 | S=O stretching in sulphoxide |
| 900 | C=C bending in alkene (vinyldiene); C–H bending in tri, disubstituted compounds |
| 705–685 | C=C bending in cis-disubstitued alkene |
| 601 | Presence of C–N–S bending vibrations |
| 557-480 | C-X stretch in alkyl halides |

### 3.1.2 Thermogravimetric analysis

Thermogravimetric analysis and differential scanning calorimetry of samples of fresh (fig. 3.2) and used (fig.3.3) cigarette filters were carried out in nitrogen atmosphere in the temperature range of 25-800°C at a heating rate of 10°C/min. For both samples 4 zones of mass loss were observed.

For the fresh filter sample (Fig. 3.2) in the temperature range of 25-100°C the mass loss is 4.8% for the loss of external moisture. The mass loss of 12.5% at 100-300°C is attributed to thermal decomposition of plasticizers. The main mass loss in the range of 300-400°C with a peak DTG of 349°C refers to the thermal decomposition of cellulose acetate [131] and it is 67%. The fourth stage, occurring at 400°C, is characterized by the formation of ash and carbon residue [132], accompanied by a mass loss of 3.6%.
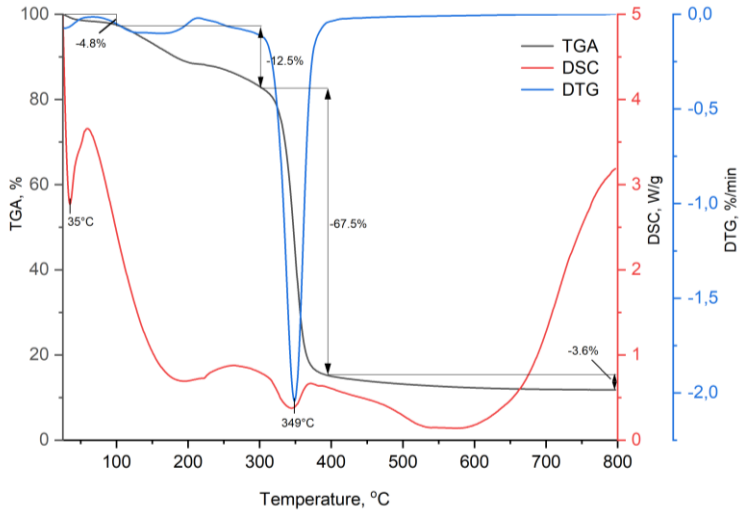
Fig. 3.2 TGA-DSC-DTG curves of fresh cigarette filter (black line – TGA,
red line – DSC, blue line - DTG)

In the case of the used filter, the mass loss observed in the initial stage is 3.0%. In the second stage, the mass loss is also approximately twofold that of the pure sample, equating to 29.3%, attributed to presence of tobacco combustion products. The primary mass loss 50.3% resulting from the decomposition of cellulose acetate.
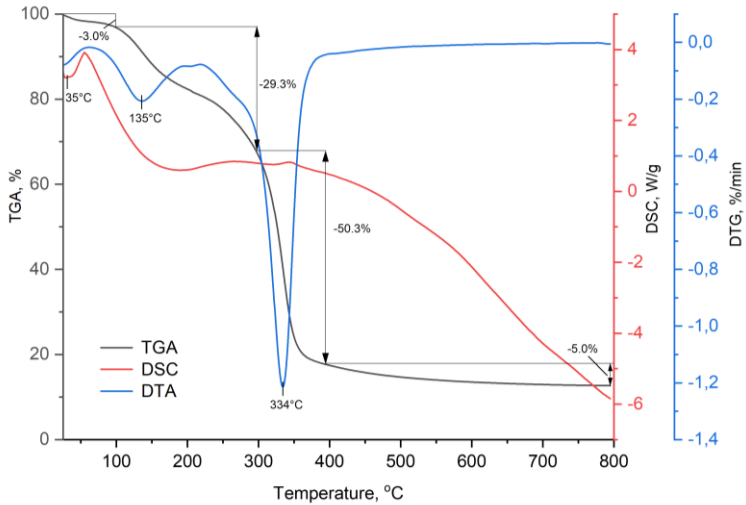


Fig. 3.3 TGA-DSC-DTG curves of used cigarette filter (black line – TGA,
red line – DSC, blue line - DTG)

61

### 3.1.3 Scanning electron microscopy

The field emission scanning electron microscopy (FESEM) technique was used to investigate the structure of the cigarette filter fibers before and after use. The images show that the fiber structure does not change during the use of the filter while smoking, being composed of microfibrils in both cases (before and after use).
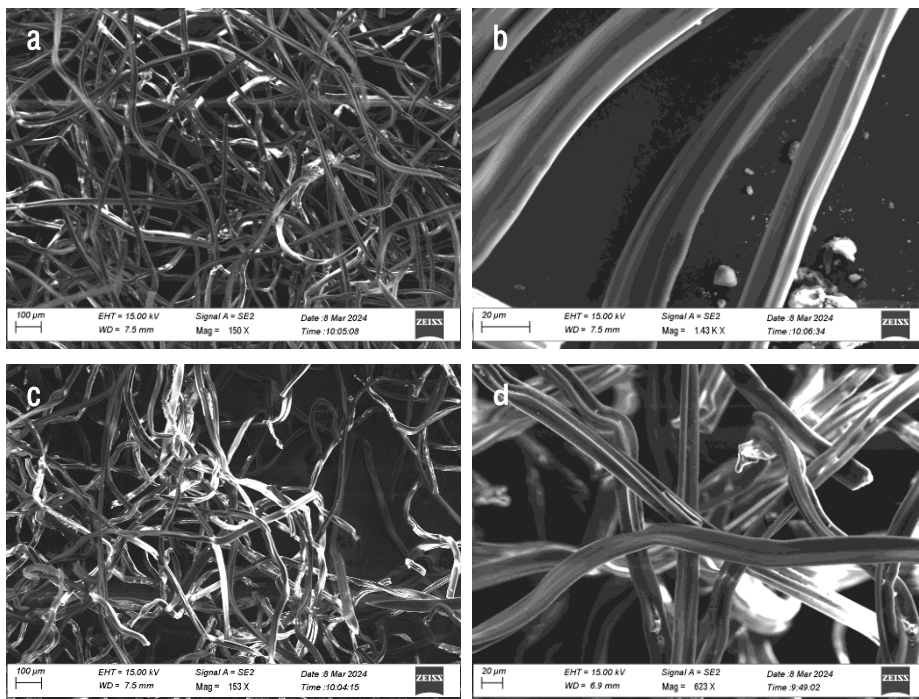


Fig. 3.4 FESEM graphs of fibers from: a, b – fresh cigarette filter; c, d – used cigarette filters

## 3.2. Recovering of cellulose acetate

Cellulose acetate was extracted from cigarette filters using a multi-stage process (Fig. 3.5). Initially tobacco residue, ash, wrapping paper and burnt filter fragments were removed manually using tweezers and a scalpel. The composition of cigarette filters and the content of organic matter and heavy metals accumulated in the filters vary with the brand of cigarettes [130] and factors like filter size, smoking duration, storage and collection conditions. Therefore, the filters were shredded and homogenized using a blender. Subsequently, the homogeneous fiber was subjected to a series of washing processes utilizing a range of solvents, as detailed in Table 3.2.
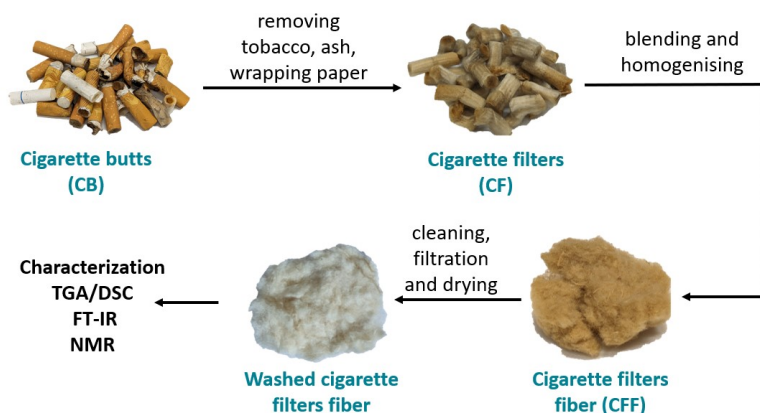
Fig. 3.5 Steps to recover cellulose acetate from cigarette butts

To evaluate the efficiency of each solvent, 500 mg of cigarette filter fiber and 50 ml of solvent (Table 3.2) were placed in a round-bottomed flask and stirred with a magnetic stirrer for 30 minutes. In some cases, the flask was placed in an oil bath to maintain the required temperature (Table 3.3). The fiber was then separated from the solvent by filtration through a Buchner system with filter paper, washed with 25 ml of deionized water (3 times) and dried at 85°C in oven for 3 hours. The resulting material was cooled and stored in an exicator. The characterization of the purified samples was carried out using Fourier-transform infrared spectroscopy in attenuated total reflectance modality (ATR-FTIR) and thermogravimetric analysis.

An important aspect of purification is the preservation of the acetate groups on the surface of the cellulose, since a large amount of acetic anhydride is used to acetylate the cellulose (approximately 1:1 mass of anhydride to mass of cellulose at a degree of substitution of 2.5). For this purpose, the safest and most non-destructive solvents were chosen as cleaning solvents: deionized water, sodium chloride solution and ethanol.

Table 3.2 Cleaning solvents and parameters

| № | Solvent | Variable extraction parameters |
|---|---------|-------------------------------|
| 1 | Deionized water | Temperature 20, 40, 60 and 80 °C |
| 2 | Sodium chloride (NaCl) water solution | Concentration 1, 3.5, 5, 10, 15% |
| 4 | Ethanol (EtOH) | Concentration 25, 50, 75, 96 and 99.8% |

### 3.2.1 Purification with deionized water

The choice of deionized water is due to the use of water as the solvent for primary washing cigarette filters in most studies [58, 59, 60]. The aqueous medium has been reported to remove solid impurities as well as water-soluble compounds from the surface of the cellulose acetate, while preserving its structure. In works of De Fenzo [60] and Afroz [133] washing has been carried out in water at 50 and 70 Celsius degrees. Aiming at assessing the effect of temperature on the quality of purification, in the present study cellulose acetate was treated with deionized water at temperatures of 20, 40, 60 and 80°C.

As illustrated in the images reported in Figure 3.6, water is an ineffective bleaching agent for organic resins. Consequently, the appearance of the samples after washing with water is nearly identical to that of the unwashed fiber.



CF used    H$_2$O 20 °C    H$_2$O 40 °C    H$_2$O 60 °C    H$_2$O 80 °C
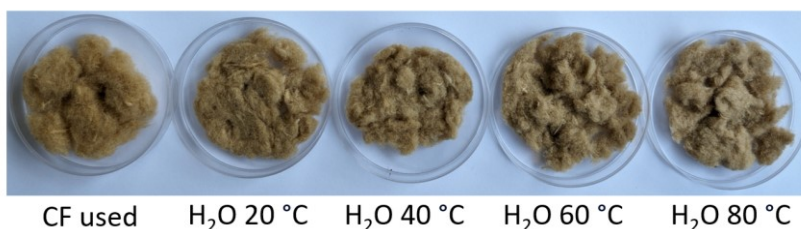
Fig. 3.6 Cellulose acetate fiber after purification by water at different temperatures

The effect of temperature increasing is clearly visible in the FT-IR spectra. Thus, the peaks at 1738 cm$^{-1}$, 1215 cm$^{-1}$ and 1033 cm$^{-1}$ show a significant loss of intensity with increasing water temperature, indicating a decrease in the concentration of amines and esters during the washing process (Fig. 3.7).
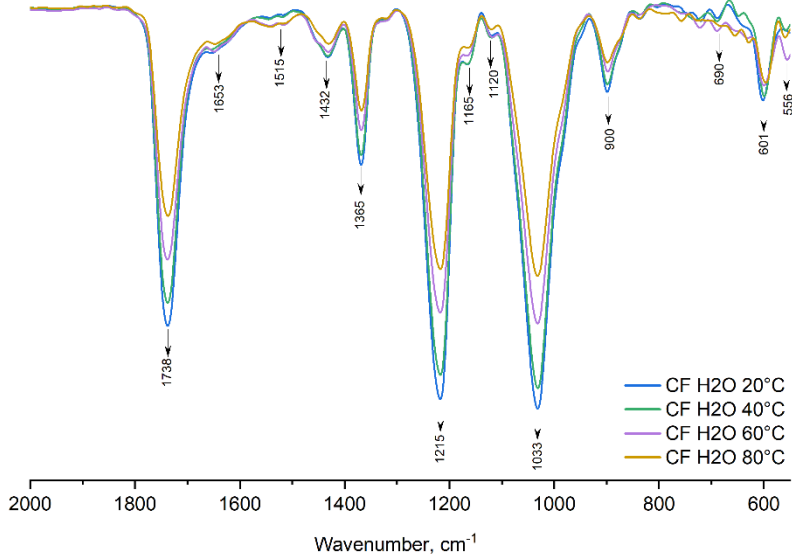
Fig. 3.7 FT-IR spectra of samples after purification by water at different temperatures

TGA curves also confirm the improvement of the purification degree with rising temperature (Fig. 3.8). Moreover, for all samples, mass loss was not observed in the range of 100-300°C during plasticizer decomposition, which is present in both fresh and used filter samples.
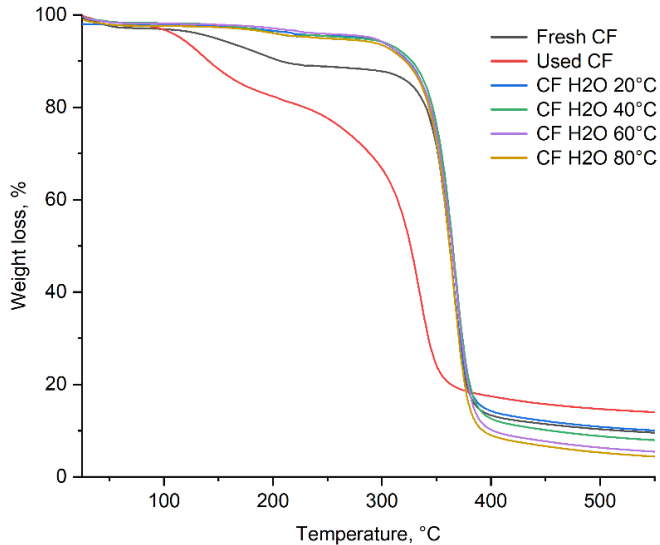


Fig. 3.8 TGA curves of samples after purification by water at different temperatures

*3.2.2 Purification with NaCl solution*

Sodium chloride (NaCl) solution is of interest as another green solvent for pre-cleaning in the recovery of cellulose acetate from cigarette filters. It is established that a 5% NaCl solution is an effective solvent for extracting metals from the surface of cellulose acetate cigarette filters [59]. Sodium ions Na⁺ can displace heavy metal ions from adsorbents, facilitating their removal. Nevertheless, the impact of NaCl and its concentration on the extraction of organic contaminants has not yet been studied. To evaluate this effect, cigarette filter fibers were washed according to the protocol in solutions of 1%, 3.5%, 5%, 10%, 15% NaCl.

The residual tobacco tar remained on the acetate cellulose fibers after the cleansing process conducted with sodium chloride solutions (Fig.3.9), as it was already observed in the samples cleaned with deionized water (Fig. 3.6).



CF used      NaCl 1%      NaCl 3,5%      NaCl 5%      NaCl 10%      NaCl 15%
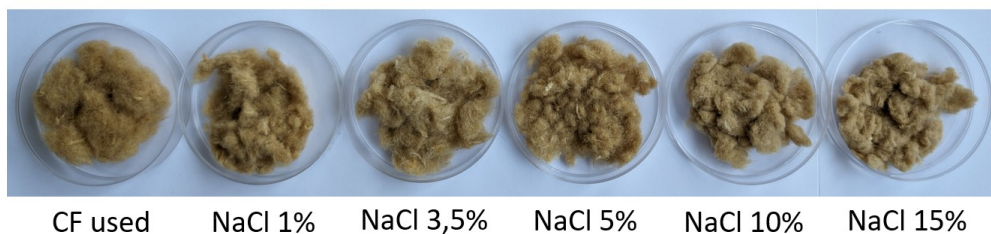
Fig. 3.9 Cellulose acetate fiber after purification by NaCl solutions of varying concentrations

FT-IR spectra of cellulose acetate after purification in aqueous sodium chloride solutions (Fig. 3.10) show a decrease in the intensity of the impurity peaks with decreasing NaCl concentration in the solvent. Thus, the best purification performance is observed for samples treated in 1% and 3.5% NaCl solutions.
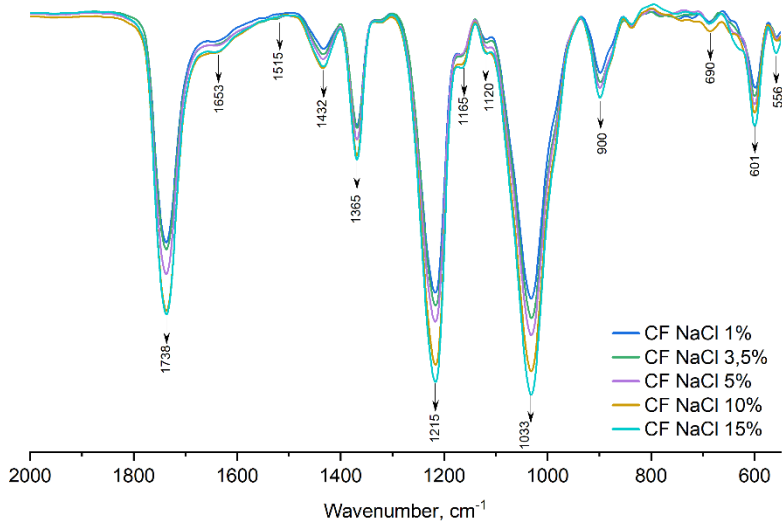
Fig. 3.10 FT-IR spectra of samples after purification by NaCl solutions of varying concentrations

Contrary to the TGA curves of samples purified with water, samples purified with a NaCl solution show loss of mass due to plasticizer decomposition in the temperature range of 150-350°C. At the same time, solutions with a lower concentration demonstrate the removal of a higher amount of plasticizer during the purification process, as evidenced by a lower loss of mass.
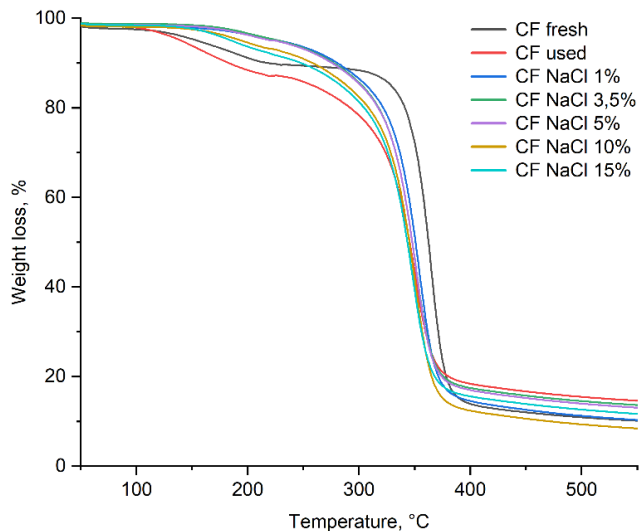


Fig. 3.11 TGA curves of samples after purification by NaCl solutions of varying concentrations

### *3.2.3 Purification with ethanol*

Among organic solvents, ethanol is regarded as the most cost-effective and environmentally friendly option for the extraction of cigarette filter contaminants, given the potential for obtaining it from renewable plant raw materials. The majority of research studies have demonstrated the high efficiency of cleaning with absolute ethanol with multiple (2-3 cycles) washing runs. Additionally, it has been established that the solubility of organic compounds in ethanol is significantly influenced by the volume fraction of ethanol in the washing solvent [134]. Based on these findings, in the present study cigarette filter fibers were cleaned in ethanol/water mixture with ethanol volumes of 25%, 50%, 75%, 96% and absolute ethanol, in order to ascertain the most effective cleaning solution.

The visual effect of ethanol concentration in the solvent is illustrated in Figure 3.12. The use of a 75% ethanol solution for cleaning has been found to be highly effective in removing a considerable quantity of resin and other impurities from the surface of the filter fiber, in comparison to solvents that contain a higher proportion of ethanol solvents.



CF used    EtOH 25%    EtOH 50%    EtOH 75%    EtOH 96%    EtOH abs.
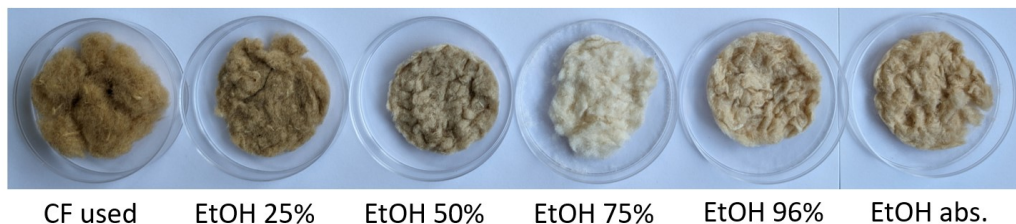
Fig. 3.12 Cellulose acetate fiber after purification by ethanol of varying concentrations

The FT-IR analysis data also confirms the visual result of the purification (Fig. 3.13). The highest peak intensities of amines and esters are observed for the fiber after cleaning with 25% (blue line) and 50% ethanol (green line), followed by approximately the same results for 96% (light blue line) and absolute (yellow line) ethanol. The sample washed with 75% ethanol (purple line) has the lowest intensity, indicating the removal of the biggest amount of contaminants.
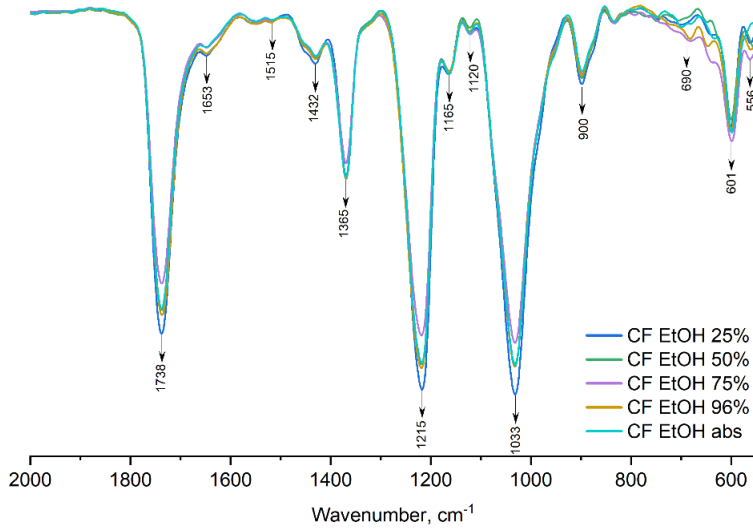
Fig. 3.13 FT-IR spectra of samples after purification by ethanol of varying concentrations

The TGA curves (Fig. 3.14) demonstrate a high degree of ethanol purification for all samples. A slight difference is noticeable in the 200-350°C range where the sample washed with 75% ethanol (purple curve) illustrate better removal of contaminants and plasticizers.
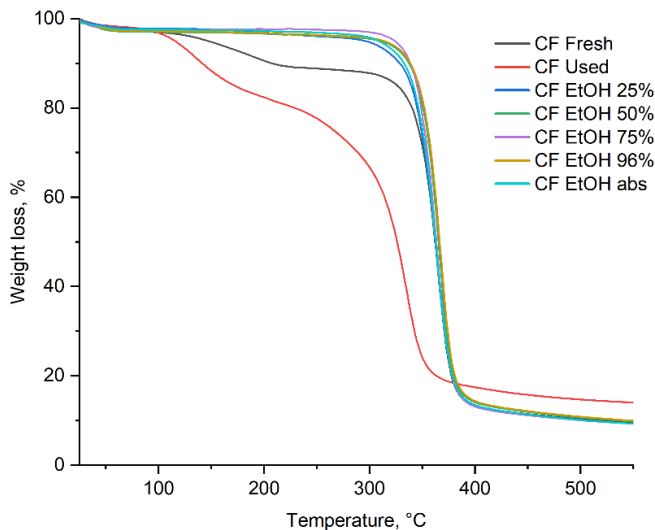


Fig. 3.14 TGA curves of samples after purification by ethanol of varying concentrations

The FESEM graphs of the contaminated used filter (Fig. 3.15a) and the filter after 75% purification (Fig. 3.15b) demonstrate that the fiber morphology remains after the cleaning process.
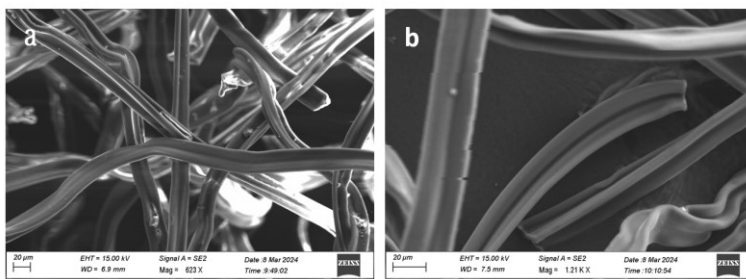


Fig. 3.15 FESEM graphs of fibers: a – used cigarette filter; b – filter after treatment by 75% ethanol

### 3.2.4 Optimization of cleaning process

In order to optimize the cleaning process, a further investigation was conducted into the effects of the following parameters: cleaning time, material-to-solvent ratio, and number of cycles. To determine optimal cleaning time, contaminated acetate cellulose fibers were treated with a 75% ethanol-water solution for 15 min, 30 min, 2 h and 5 h, respectively. As illustrated in the TGA graph (Fig. 3.16), the 15-minute washing period (black line) was found to be the least effective, with the remaining samples exhibiting a comparable degree of purification.
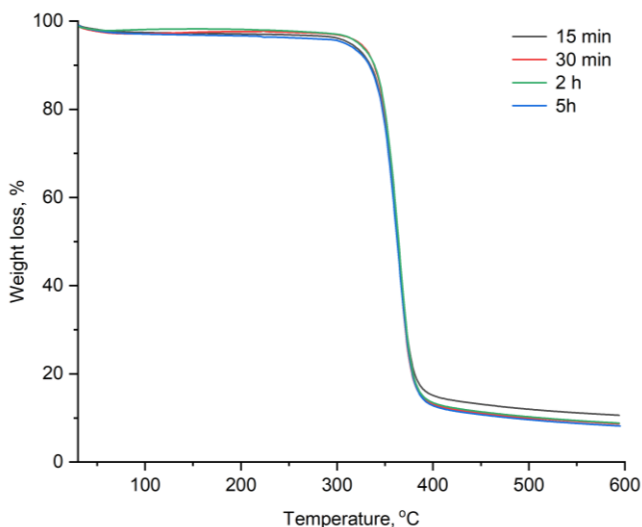


Fig. 3.16 TGA curves of samples after purification by 75% ethanol of varying treatment time

For the material to solvent volume ratio test, 500 mg of contaminated cellulose acetate fiber was cleaned for 30 minutes in 25, 50, and 100 mL of 75% ethanol solution, corresponding to ratios of 1:50, 1:100, and 1:200, respectively. The TGA curves (Fig. 3.17) shows that the quality of purification decreases significantly when the volume of solvent is halved (ratio 1:50) (black line) compared to the standard protocol (1:100) (red line).
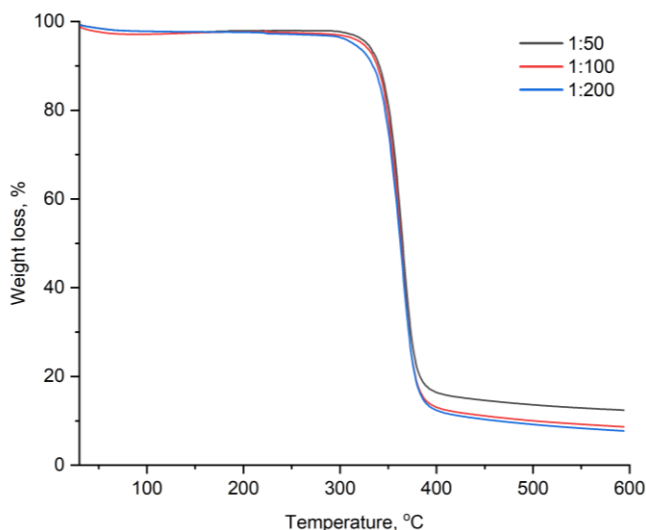


Fig. 3.17 TGA curves of samples after purification by 75% ethanol of varying material : solvent ratio

After determining the optimum cleaning time (30 min) and material : solvent ratio (1:100), these parameters were used to determine the number of wash turns with 75% ethanol. The visual effect is also noticeable after each cleaning cycle (Fig. 3.18). Thus, the maximum degree is observed after cycle 3, which is proposed to be the final cycle.



Figure 3.18 Cellulose acetate fiber after purification in 75% ethanol multiple cycles

To confirm the purification efficiency, samples of used CF, fresh CF, and CF after first and third cycle cleaning by 75% ethanol were dissolved in Dimethyl sulfoxide (DMSO) at 60°C and analyzed by nuclear magnetic resonance (NMR) spectroscopy.

With regard to the used CF (Fig. 3.19 a), an area in the range of 6.5 - 9 ppm is indicative of the presence of aromatic compounds formed during the combustion of tobacco. In the case of the fresh filter (Fig. 3.19 b) and samples after cleaning with 75% ethanol (Fig. 3.19 c, d), no peaks are observed in this region, thereby confirming the complete removal of organic pollutants during the cleaning process. Furthermore, the spectra of the filter after cleaning (Fig. 3.19 c, d) demonstrate the absence of glycerol peaks in the triacetin plasticizer, present at approximately 4 ppm, in comparison to both used (Fig. 3.19 a) and fresh CF(Fig. 3.19 b), thereby corroborating previous analyses which have indicated that the plasticizers are removed during the cleaning process.
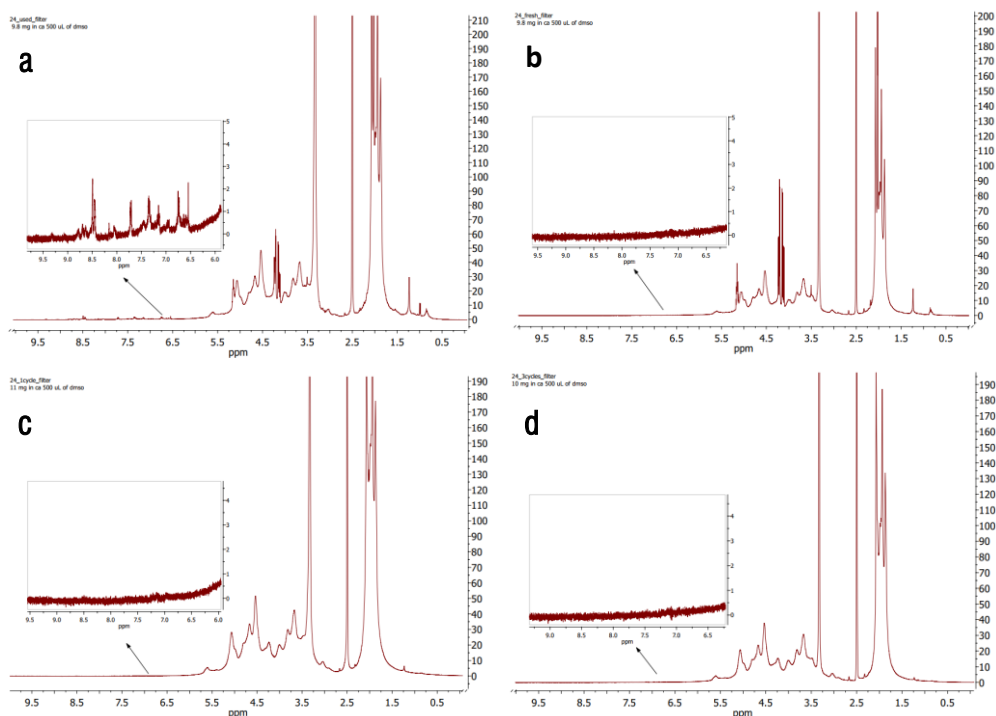


Fig. 3.19 NMR spectra of a – used CF, b – fresh CF, c – CF after first cycle cleaning by 75% ethanol, d – CF after third cycle cleaning by 75% ethanol

### 3.2.5 Solvent selection

To determine a suitable solvent, a solubility test was carried out with fresh cigarette filters, followed by the preparation of cellulose acetate films. For this purpose, 300 mg of fresh filters fiber was placed in 10 ml of solvent and stirred for 30 minutes at 25°C until a uniform solution was formed. The resulting solution was poured into a Petri dish (d = 90 mm) and dried at 25°C until the solvent completely evaporated.

The most common solvent for cellulose with acetate degree of substitution (DS) of 2–2.5 is acetone, while in the case of cellulose acetate used in cigarette filters, the degree of substitution is 2.35-2.55. However, due to the presence of various additives, including polylactic acid (PLA) and plasticizers, in cigarette filters, acetone was unable to completely dissolve the material. Upon hardening, an uneven film containing white PLA inclusions formed (Fig. 3.20a). To solve this problem, ethyl acetate and N,N-dimetilformammide (DMF) were chosen due to ability to dissolve well both components (cellulose acetate and PLA plastic). As can be seen in the image (Fig.3.20b), the cellulose acetate composite material is completely dissolved in ethyl acetate while was forming a dense transparent film during the hardening process. Artifacts on the film were obtained due to drying uneven air flow condition. In case of DMF as a solvent, the transparent solution formed a not transparent white matte film (Fig.3.20c). This matte film was softer and easier to tear compared to the previous sample.
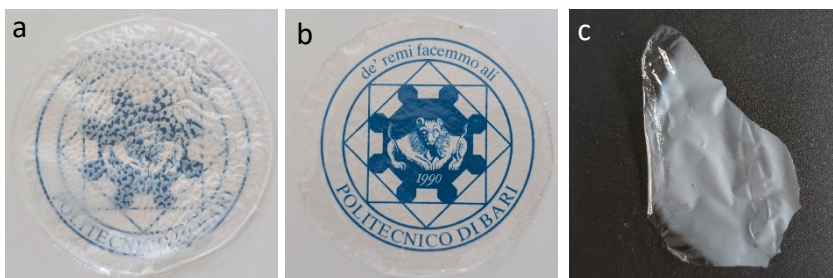


Fig. 3.20 Resulting films from fresh cellulose acetate filters in different solvents
(a) in acetone, (b) in ethyl acetate, (c) in DMF

Based on the above reported results, ethyl acetate was identified as the optimal solvent and used to obtain a film from the material after purification. The film obtained after cleaning (Fig.3.21b) according to the protocol described above has minor

differences in color (light yellow tint) and strength with respect to the fresh filters film (Fig.3.21c).
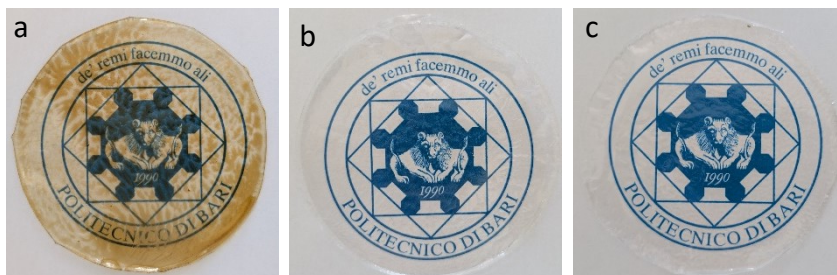


Fig. 3.21 Resulting cellulose acetate films from cigarette filters: a – dirty used filter, b – used filter after purification protocol, c – fresh filter

## 3.3. Conclusions

In order to valorize cigarette butt waste for the recovery of cellulose acetate polymer, a protocol for the cleaning of cigarette filters was developed and optimized. Water (with temperature variation), NaCl solution (with concentration variation) and ethanol (with concentration variation) were used as green solvents. The optimal parameters for each solvent were identified by FT-IR and TGA technics. Therefore, the highest degree of purification was observed for deionized water at temperatures of 60°C and 80°C. In the case of the NaCl solution, which is effective at removing heavy metals, increasing the concentration results in a reduction in the removal of organic pollutants. In the case of the ethanol-water solvent system, a 75% ethanol solution demonstrated the complete removal of tobacco combustion products. Furthermore, experiments were conducted to determine the optimal cleaning time, material-to-solvent ratio, and number of cleaning cycles. Furthermore, ethyl acetate was identified as the optimal solvent for the reduction of cellulose acetate, resulting in the production of a transparent polymer film.

# 4.    CELLULOSE EXTRACTION FROM TUNICATES

## 4.1. *Clavelina oblonga* tunicates characterization

*Clavelina oblonga* tunicates were sampled from a mussel farm on the western coast of the Istrian peninsula, in Lim Bay, situated in the northern Adriatic Sea, Croatia. Colonies of *Clavelina oblonga* were collected from the mussel farming ropes, washed and frozen at -86 °C. All tissues were processed in their entirety, freeze-dried for 72 hours and pulverized in the vibrational cryogenic mill to obtain tunicate powder (TP) (Fig. 4.1).



Washing
Freeze drying
Grinding

Tunicates powder (TP)

Clavelina Oblonga

Fig. 4.1 Preparation of tunicate powder (TP) from *Clavelina oblonga*

### 4.1.1 Proximate composition

Sample material primarily consisted of water (moisture) as the major constituent in their proximate body composition (Table 4.1). Despite rinsing the free water and drying the organisms using paper towels, there is a possibility of minimal residual water within the inner body tissues during analysis. *Clavelina oblonga* accordingly exhibited a moisture content of $95.44 \pm 0.0025\%$. The organic components, constituting proteins and lipids, were expressed on a dry basis.

Table 4.1. Proximate composition (% dry weight) of *Clavelina oblonga*

| Component | Content, $\%_w$ |
|-----------|-----------------|
| Moisture | $95.44 \pm 0.003$ |
| Ash | $29.06 \pm 1.71$ |
| Proteins | $39.23 \pm 0.65$ |
| Lipids | $8.64 \pm 0.52$ |

### *4.1.2 Fatty acid composition*

The major fatty acids in the entire tissues of *Clavelina oblonga* (Table 1S) were palmitic acid, PA (C16:0), stearic acid, SA (C18:0), and docosahexaenoic acid, DHA (C22:6n3), followed by docosanoic acid, DA (C22:0), elaidic acid, EA (C18:1 trans), linoleic acid, LA (C18:2 cis), and myristic acid, MA (C14:0) (Fig. 4.2, 4.3). The three groups of fatty acids (saturated - SFA, monounsaturated - MUFA, polyunsaturated - PUFA) accounted for 51.37 ± 0.27%, 15.41 ± 0.22%, and 26.96 ± 0.40% of total fatty acids, respectively. The total unsaturated fatty acid – UFA accounted for 42.37 ± 0.18%. The ω-3 PUFA ratio was 16.10 ± 0.38%, ω-6 PUFA ratio was 10.86 ± 0.01%, while ω-6/ ω-3 ratio amounted to 0.68 ± 0.01. The nonidentified fatty acids comprised 6.26 ± 0.12%.
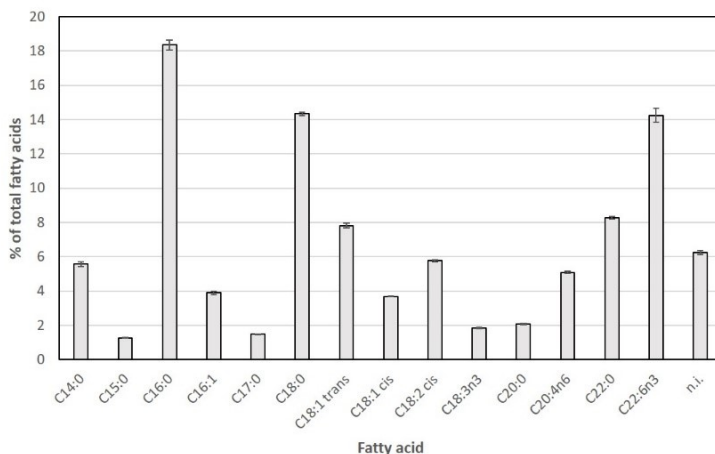


Fig. 4.2 Fatty acid composition of *Clavelina oblonga*
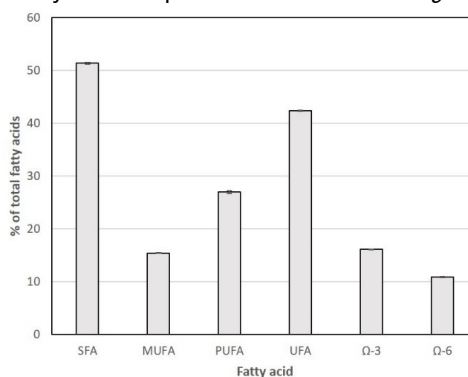


Fig. 4.3 Groups of fatty acids from *Clavelina oblonga*

### 4.1.3 Trace and macroelements

A total of 32 trace elements and 6 macroelements were measured in entire *Clavelina oblonga* tissues. Of trace elements, Al was predominant, the sequence of concentration being Al > Fe > Sr > Ti > Mn > V > Zn > Cu > Ba > As > Li > Rb > Ni > Cr > Pb > Mo > Se > Co > Y > Nb > Th > Sc > Cs > Sn > Ag > U > W > Be > Cd > Sb > Tl > Bi. The most common trace elements are shown in table 4.2.

Table 4.2. Trace elements concentration *Clavelina oblonga*

| Trace elements | Concentration, $\mu$g/g |
|:---:|:---:|
| Al | 1843 ± 676 |
| Fe | 1274 ± 467 |
| Sr | 140 ± 9 |
| Ti | 113 ± 40 |
| Mn | 50.8 ± 5.5 |
| V | 37.6 ± 5.5 |
| Zn | 35.8 ± 4.8 |
| Cu | 19.8 ± 4.5 |

Of macroelements, Na was predominant, the sequence of concentration being Na > S > Mg > Ca > K > P (Table 4.3).

Table 4.3. Macroelement composition of *Clavelina oblonga*

| Macroelement | Ca | K | Mg | Na | P | S |
|:---:|:---:|:---:|:---:|:---:|:---:|:---:|
| Concentration, mg/g | 11.1 ± 1.6 | 5.21 ± 0.6 | 17.6 ± 2.0 | 99.1 ± 11.7 | 2.06 ± 0.33 | 29.2 ± 2.1 |

### 4.1.4 Fourier Transform Infrared (FT-IR) analysis

The composite structure of *Clavelina oblonga* was verified also by FT-IR (Fig.4.4). The strong and wide peak centred at 3282 cm$^{-1}$ was assigned to the O-H and N-H stretching mode. The observed widening indicates a large expansion of the OH/NH group associated with the hydrogen bond. The peaks at 2923 cm$^{-1}$ and 2853 cm$^{-1}$ as

well as the slight shoulder at 3023 cm$^{-1}$ are to be attributed to C-H stretching in CH$_3$ and CH$_2$ of proteins and lipids [135, 136].
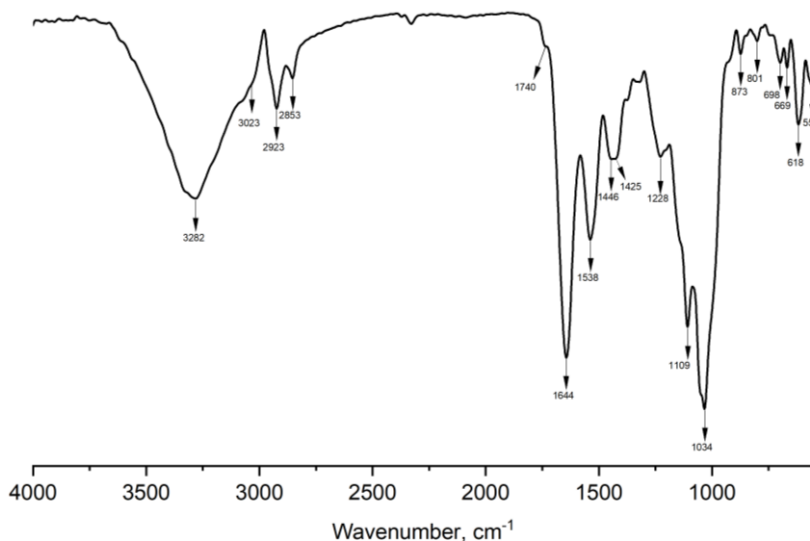


Fig. 4.4 FT-IR spectra of tunicate powder

The intense bands at 1644 and 1538 cm$^{-1}$ belong to Amide I and Amide II vibration modes of proteins, respectively [137]. We attributed also the peaks at 1446 and 1425 to the symmetric deformation of CH$_3$ and CH$_2$ of proteins [138, 139]. The peak at 1034 cm$^{-1}$ is related to the C-O-C vibration of the β-glycosilic bond in cellulose and the shoulder band at 1109 cm$^{-1}$ arises from C–O–C pyranose ring skeletal vibration of cellulose components. However, these bands may partly overlap with the bands originating C–N stretching (amid groups of proteins), suggesting an overlapping of adsorbing peaks from proteins and carbohydrates present in the tunicate mass. The adsorption peak at 1109 cm$^{-1}$ can also be attributed to the C–OH skeletal vibration [140]. As for the small peak at 873 cm$^{-1}$, it might correspond to the glycosidic –CH deformation with a ring vibration and –OH bending, which is characteristic of β-glycosidic linkages between glucose units in cellulose [140, 141, 142]. In addition, the band at 1228 cm$^{-1}$ might reveal a sulphate ester with a S=O band [141] and the signal at 1740 cm$^{-1}$ refers C=O stretching in lipid components.

### 4.1.5 Thermogravimetric analysis

Figure 4.5 shows the TGA-DSC-DTG curves of the dried *Clavelina oblonga* mass at a heating rate of 10°C min$^{-1}$, with the pyrolytic characteristics in an inert or N$_2$ environment, where the heating temperature ranged from 25°C to 1000°C. The whole pyrolytic process can be divided into four reactive stages. In the first stage (25-200°C), a slight weight loss is recorded (up to 10%), due to dehydration and loss of water and light volatiles release [141]. Thereafter, a significant mass loss (up to 39 wt%) is observed in the range of temperatures within 200-450°C, mainly stemming from the thermal decomposition of proteins and carbohydrates. In the temperature range of 450-600°C, the tunicate mass decays slightly, indicating the decomposition of lipids, which usually occurs at higher temperatures with respect to proteins and carbohydrates [143]. The last stage, at temperatures higher than 600°C, can be attributed to a continuous and slow weight loss of carbonates in the solid residue [144].
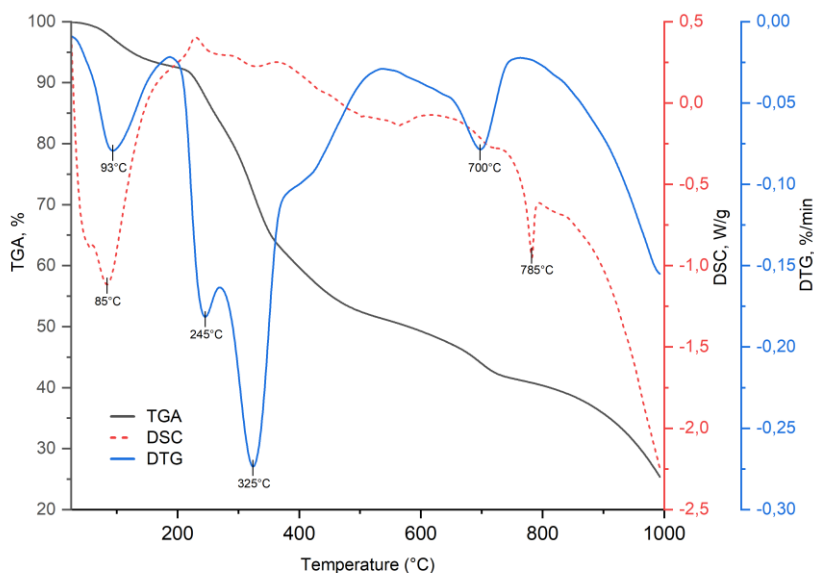


Fig. 4.5 TGA-DSC-DTG curves of tunicates powder

The TGA curves did not reach the final plateau, probably due to the different transition phases of salts and oxides in the ash content. Analyzing the DTG curves, we can clearly distinguish 5 peaks: one at 97°C that confirms the dehydration and loss of

volatile compounds; the two main peaks at 245°C and 325°C due to degradation of proteins and cellulose, respectively; a slight shoulder at 420°C due to lipid degradation; and the peak at 700°C, corresponding to the decomposition of carbonates in tunicates.

### 4.1.6 Solid-state NMR spectroscopy

The spectrum of $^{13}$C CP/MAS of TP confirms that the material is constituted of protein, lipids and cellulose. The NMR spectrum could be divided into five regions (Fig 4.6). Region 1 contains signals deriving from aliphatic residues of aminoacids of proteins and aliphatic chain of lipids. Region 2 contains the signals deriving from alpha carbon of aminoacids. In region 3 signals of carbohydrates are detected. Most deshielded signals which fall around 105 ppm are assigned to anomeric carbon of cellulose region. Interestingly, differing to common spectrum of cellulose in this case the sharpness of the cellulose signals indicates an ordered and well-defined structure. Region 4 contains signals belonging to aromatic compounds in aminoacids and finally region 5 is the part of spectrum containing signals of the carbonyl group of peptides bonds and fatty acids.
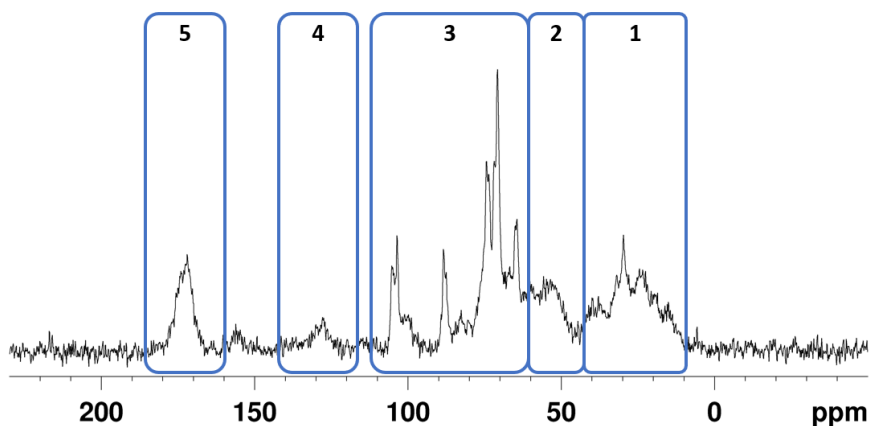


Fig. 4.6 $^{13}$C CP/MAS spectra of Tunicates Powder

## 4.2. Deep Eutectic Solvents (DES)

Abbott et al. [145] first introduced a deep eutectic solvent (DES), a mixture of choline chloride and urea, in 2003. Since then, DESs have garnered considerable attention due to their low toxicity, biodegradability, and ease of preparation. These solvents

80

represent a significant breakthrough in green chemistry, offering environmentally friendly alternatives to traditional solvents [146]. While DESs resemble ionic liquids (IL), they possess distinct characteristics that enhance their sustainability and versatility for various applications, including catalysis, electrochemistry, and material processing. Notably, DESs can be produced from readily available, low-cost starting materials [147].

DESs are formed by combining a hydrogen bond donor (HBD) and a hydrogen bond acceptor (HBA), typically an organic salt, as depicted on Fig. 4.7. Upon mixing at a specific molar ratio, these components create a eutectic mixture with a melting point significantly lower than that of either individual component [148].
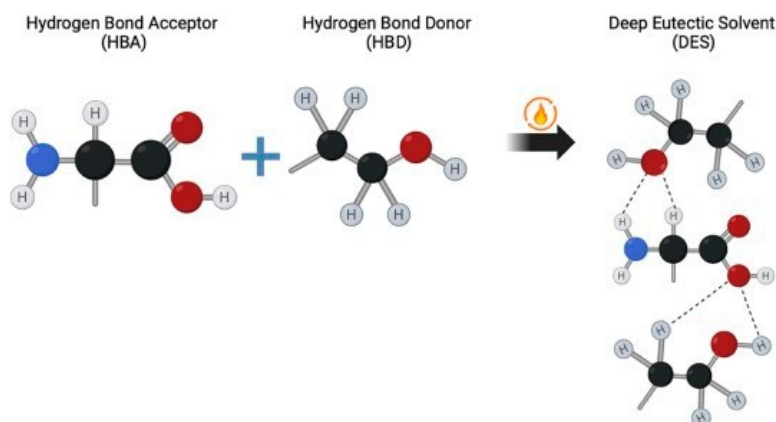


Fig. 4.7 The mixing principle of DES upon the addition of HBA with HBD [148]

The lower melting points of DESs are attributed to the formation of hydrogen bonds between the HBD and HBA, which reduces the lattice energy of the system. The phase diagram (Fig. 4.8) illustrates the formation of a eutectic solution, characterized by a minimum melting point significantly lower than that of its individual components. For example, choline chloride:urea DES prepared in a 1:2 molar ratio exhibits a melting point of 12 °C, significantly lower than that of choline chloride (302 °C) or urea (133 °C) [145].
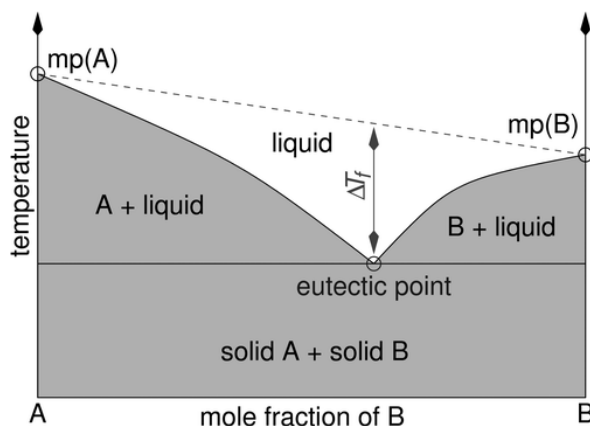
Fig. 4.8 Schematic representation of a eutectic point on a two-component phase diagram

The properties of DESs depend on the nature of the HBA/HBD combination, the molar ratio, water content, and temperature [149]. DESs are classified based on the type of HBD used, as shown in Table x. Four main types of DESs have been reported apart from fifth type of DES has also been mentioned in the literature [150]. The general formula used for DESs description:

$$R+A-xB,$$
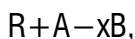
where R+ is ammonium, sulfonium, and phosphonium cation core. A and B are Lewis base with halide anion and Levis acid, respectively. The complex formation is observed between x and Lewis or Bronsted acid B (x defined as B number of molecules reacted with anion).

Table 4.4 General classification of DESs [150]

| Type of DES | General Formula | Terms | Example |
|---|---|---|---|
| I | $R^+ A^- + cMCl_x$ | M = In, Zn, Fe, Al, Sn | $ChCl + SnCl_2$ |
| II | $R^+A^- + cMCl_x.cH_2O$ | M = Ni, Cr, Fe, Cu | $ChCl + FeCl_3 \cdot 6H_2O$ |
| III | $R^+ A^- + cRW$ | W = OH, $CONH_2$, COOH | ChCl + Urea |
| IV | $MCl_x + cRW$ | M = Al, Zn and W = $CONH_2$, OH | $ZnCl_2$ + Urea |
| V | HBD + HBA | HBD = hydrogen bond donor HBA = hydrogen bond acceptor | Thymol + Menthol |

**Type I DESs** are formed by mixing quaternary ammonium salts, such as choline chloride, with anhydrous metal salts. The anhydrous nature of these salts ensures that the DES retains its ionic properties and maintains a relatively low melting point. Common metal salts used in Type I DESs include zinc chloride ($ZnCl_2$) and tin chloride ($SnCl_2$) [151].

**Type II DESs** are similar to Type I, but they differ in that the metal salts used in their formation are hydrated, meaning they contain water molecules in their crystalline structure [152]. Hydrated metal salts, such as $FeCl_3 \cdot 6H_2O$ and $ZnCl_2 \cdot 6H_2O$, introduce water into the DES, which can have a significant impact on the physical properties of the solvent, such as reducing the viscosity and altering the melting point.

In **Type III DESs**, a quaternary ammonium salt (HBA), such as choline chloride, is mixed with a neutral organic compound that serves as the hydrogen bond donor (HBD). The HBD is typically a small molecule like urea, glycerol, ethylene glycol, or carboxylic acids (e.g., lactic acid) [153]. The resulting DES is liquid at or below room temperature due to the strong hydrogen bonding between the HBA and the HBD, which disrupts the crystal lattice and lowers the melting point. This type of DES is the most widely studied and commonly used category of deep eutectic solvents.

**Type IV DES** involve metal salts combined with HBDs, such as urea, thiourea, or carboxylic acids. In this case, the metal salt itself acts as the hydrogen bond acceptor, and the hydrogen bond donor stabilizes the system through interactions with the metal cation.

Additional **Type V DES** relatively indicated as new class mixture of non-ionic molecular HBA and HBD [154]. Although it exhibits depression in melting points like DESs, there is no ionic contribution. Hydrogen bonding was especially predominant in this class of DESs.

In addition to the general classification, there is also a subtype of natural deep eutectic solvents (NADES), which consist of natural products such as organic acids, amino acids, sugars, choline or urea. [155].

## *4.3. Extraction by DES*

The extraction process with DES is affected by several factors: affinity between DES and the target compounds, the water content of samples, DES composition, the liquid/solid ratio between DES and sample, and the conditions of the extraction method.

After a deep analysis of the factors affecting the cellulose extraction from marine biomass, a microwave-assisted treatment of tunicates with an acidic DES formed by equimolar amounts of choline chloride (ChCl) and oxalic acid (OxAc) was selected [156]. Since the tunicate powder includes both the outer shell containing mainly cellulose and the internal organs, comprising proteins and lipids, carvacrol, a hydrophobic media, was used to separate neutral lipids from biological tissues [157]. In addition, microwave irradiation was exploited aiming to speed up the extraction process and to guarantee a uniform temperature distribution throughout the system. The extracted material (as a brown solid paste) was then characterized by TGA/DSC, FTIR-ATR and SEM.

Different experimental conditions were applied:

- Extraction medium:
    1) choline chloride and oxalic acid (DES);
    2) Carvacrol (CV);
    3) DES and Carvacrol (DES_CV),
- DES - MW treatment time (60 min, 30 min);
- DES - MW treatment temperatures: 80°C, 85°C, 90°C.

In Fig. 4.9 a schematic representation of the treatment of Tunicate Powder (TP) is reported.

## Route A
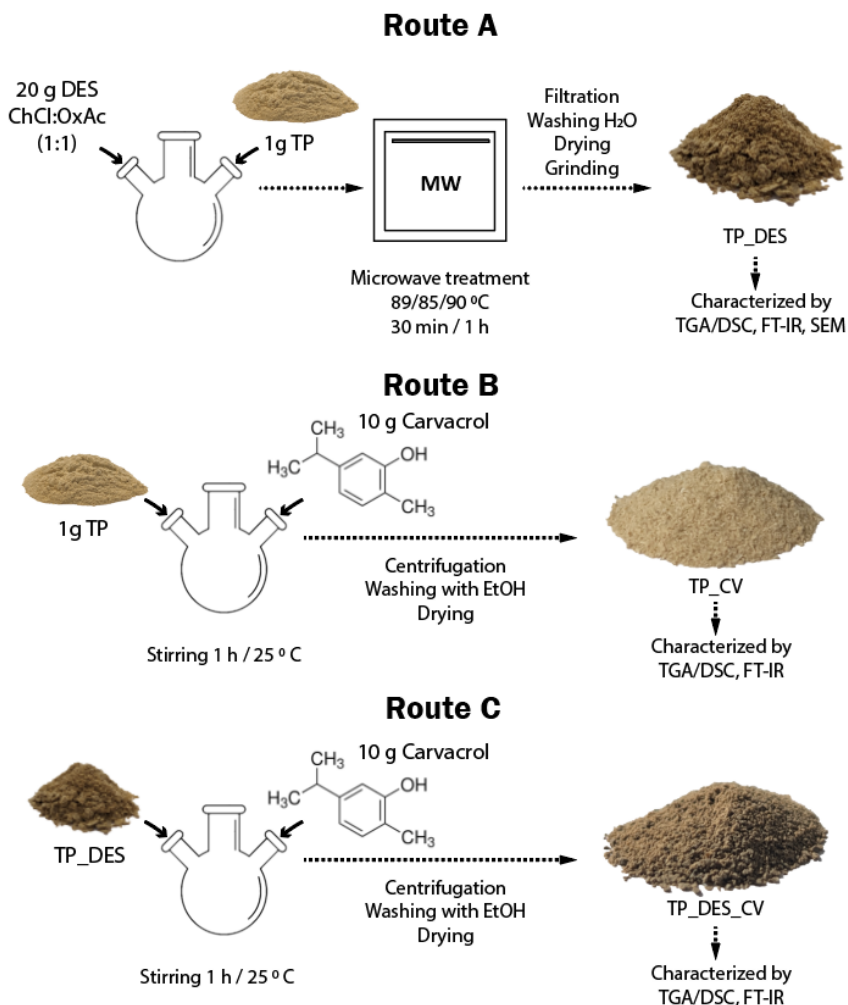


## Route B



## Route C



Fig. 4.9 Schematic representation of microwave DES treatment of tunicate powder

In route A, ChCl and OxAc (1:1) were mixed at 80°C until a transparent DES homogeneous solution was obtained. 1.0 g of TP was then added to DES and mixed under microwave irradiation. After cooling, 25 mL of deionized water was added, and the resulting suspension was filtrated off, washed twice with 50 mL of water, dried at 85°C and grounded to a homogeneous powder by mortar. Aiming at optimizing the DES treatment process, different conditions were tested (30 min and 60 min of microwave treatment time and different MW temperatures: 80°C, 85°C and 90°C).

Fig. 4.10 and fig. 4.11 reports TGA and DTG curves of pristine TP (black), Cellulose Reference (red), DES-treated TP under microwave irradiation for 30 minutes (blue) and 60 minutes (green). The TGA curve of the pristine TP (black) reveals different reactive phases. In the first stage (25-200°C, Fig. 4.10, with peak at 93°C, Fig. 4.11), a slight weight loss is registered (up to 8%), due to dehydration and/or elimination of water and light volatiles [157]; a significant mass loss (approximately 35 wt%) is observed in the range of temperatures of 200-450°C (Fig. 4.10), ascribed to the thermal decomposition of carbohydrates (including cellulose, 325°C, Fig. 4.11) and proteins (the two shoulder at 245°C and 415°C, Fig. 4.11). In the temperature range of 420-600°C, the tunicate mass decayed slightly, indicating the decomposition of lipids, which usually occurs at higher temperatures with respect to proteins and carbohydrates (Fig. 4.10). The last stage, at temperatures higher than 600°C, can be attributed to $CO_2$ loss from carbonates in the solid residue (Fig. 4.10). The TGA curves did not reach the final plateau, probably due to the different transition phases of salts and oxides in the ash content, that seems to reach approximately 15% of total weight. The high ash content for all ascidian species is attributed to the high salinity of the sea waters [158].
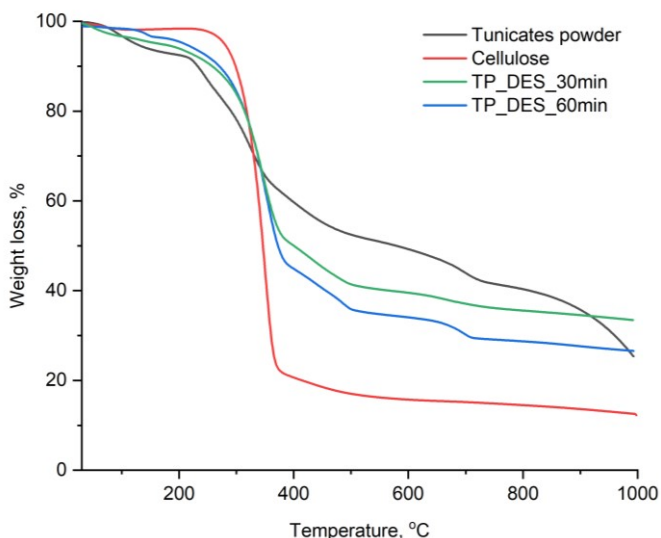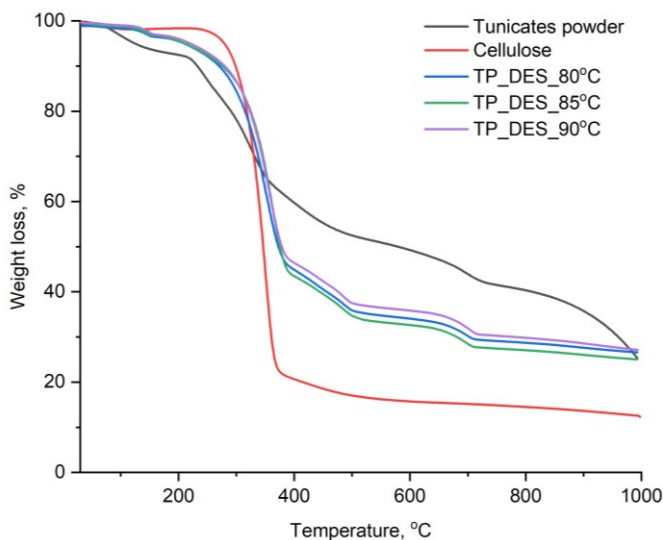


Fig.4.10 TGA curves of pristine TP, cellulose and TP treated with DES during 30 and 60 minutes
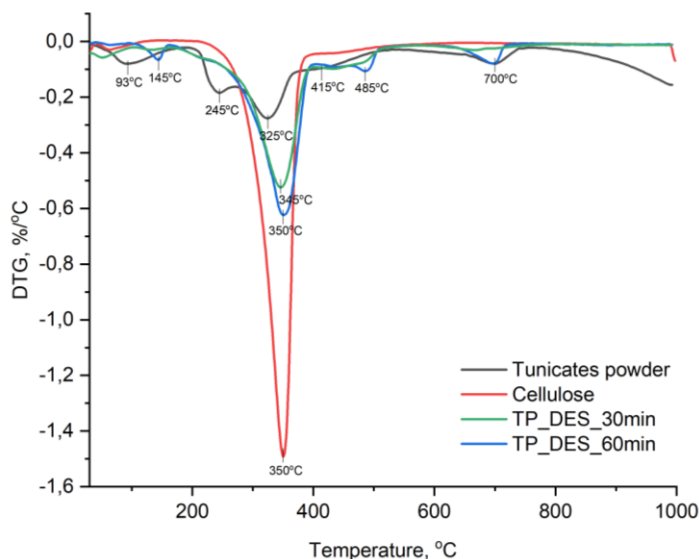
Fig.4.11 DTG curves of pristine TP, cellulose and TP treated with DES during 30 and 60 minutes

Fig. 4.10 a highlights that an increased MW irradiation time caused a slight increase (approx. 10%) of the efficiency of cellulose extraction. The DES treatment resulted in removal of proteins, as indicated by the disappearance of the peak at 245°C in the DTG curves of the extracted residues (Fig. 4.11). In addition, a slight shift of the temperature of decomposition of carbohydrates can be noticed in the TG curves of the treated TP, probably due to the different crystallinity and/or morphology of the cellulose extracted. Nevertheless, the extracted materials still contained residues of lipids (as revealed by the presence of the peak at 415°C, Fig. 4.11). In addition, the treatment for 60 minutes caused the formation of new peaks at 145°C and 485°C in the DTG curve of the solid residue. These two new peaks with the one at 700°C are indicative for the three stages of calcium oxalate decomposition [159] (blue curve, Fig. 4.11). The formation of calcium oxalate during DES treatment for 60 min. was confirmed also by IR analysis (vide infra).

$$CaC_2O_4 \cdot H_2O \leftrightarrow CaC_2O_4 + H_2O \qquad (4.1)$$
$$CaC_2O_4 \rightarrow CaCO_3 + CO \qquad (4.2)$$
$$CaCO_3 \leftrightarrow CaO + CO_2 \qquad (4.3)$$
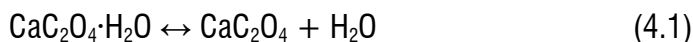
Then, the effect of the temperature increasing in the MW-assisted treatment was investigated. Fig. 4.12 and 4.13 report the TGA and DTG curves of DES-treated TP under MW irradiation at three different temperatures: 80°C (blue), 85°C (green) and 90°C (purple), respectively, indicating no significant differences in terms of proteins, lipids and carbonates removal from the extracted brown paste. In all three cases, the appearance of the peak at 485°C in the DTG curves (Fig. 4.13) was registered.



Fig.4.12 TGA curves of pristine TP, cellulose and TP treated with DES at three different temperatures
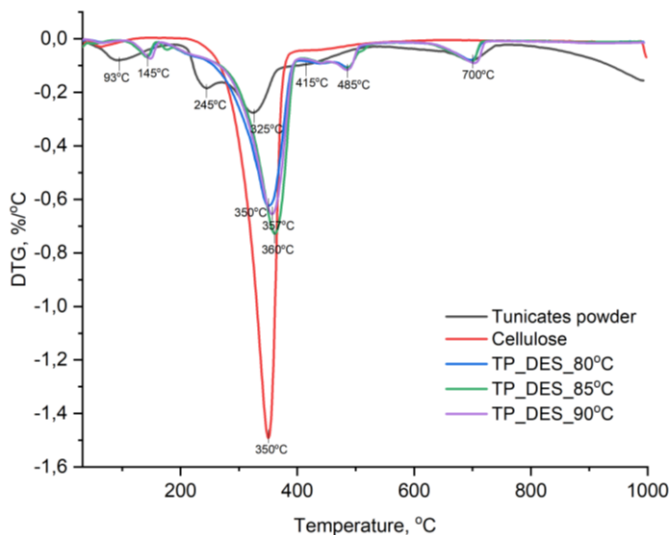
Fig.4.13 DTG curves of pristine TP, cellulose and TP treated with DES at three different temperatures

Aiming at testing the efficiency of the purification of the cellulose residue, two additional procedures were developed: treatment with carvacrol, a hydrophobic organic compound (Fig. 4.9, Route B) and MW-assisted treatment with DES followed by carvacrol washing (Fig. 4.9, Route C). In both cases, a microwave treatment time of 60 min at 85°C was used.

Fig. 4.14 and 4.15 reports TGA and DTG curves of the relevant solid residues. A close inspection of Fig. 4.14 highlights that the use of carvacrol (CV) alone or in combination with DES had no effect on the extraction process compared to the use of DES, which gives the best results in terms of cellulose extraction. However, the peak at 485°C and the slight shoulder at 145°C appear only in the DTG curve of TP treated with DES (Fig. 4.15), confirming the presence of calcium oxalate as by-product formation during DES treatment process.
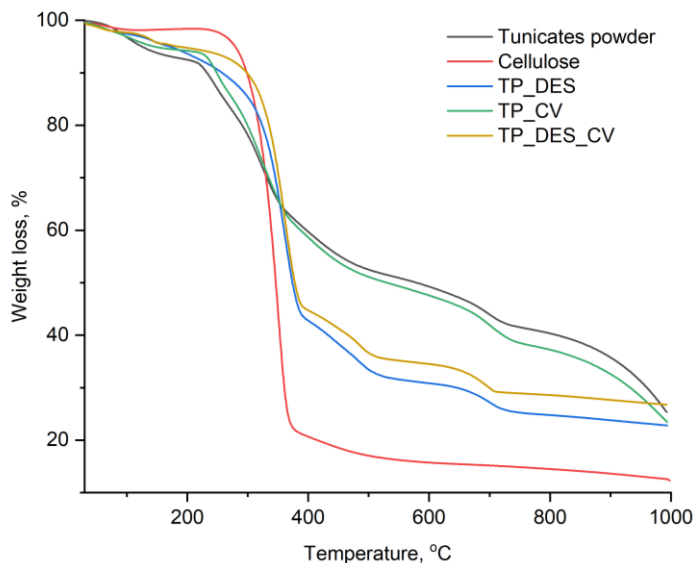
Fig.4.14 TGA curves of TP, cellulose and TP treated with different solvents
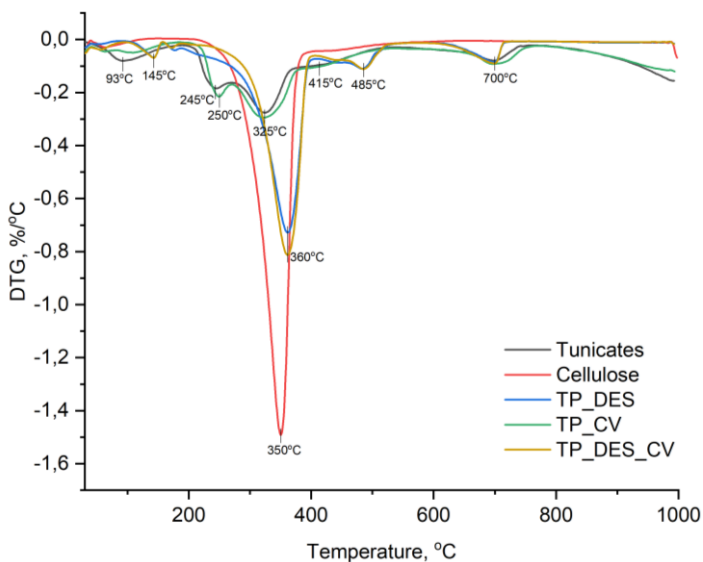


Fig.4.15 TGA curves of TP, cellulose and TP treated with different solvents

Fig. 4.16 shows the FTIR spectra of the pristine tunicate powder (TP) and the residues analysed with the three different extraction routes (DES, CV, and DES+CV).

90

The FTIR spectra of cellulose reference material is also reported. Different characteristic peaks of cellulose are visible: the peak at 1027 cm$^{-1}$ (due to the asymmetric stretching of the of C—O—C) is the most intense band. In addition, the absorption band at 1158 cm$^{-1}$ belongs to the C—O—C group, while the slight shoulder at 1740 cm$^{-1}$ is referred to C=O in lipid esters.

The spectra of DES-treated material showed in both cases (either with or without CV treatment) new peaks at 1620, 1316, and 778 cm$^{-1}$, characteristic of calcium oxalates, which precipitated as insoluble salts during DES treatment with oxalic acid and choline chloride. Further tests with different DES compositions will be tested to avoid the formation of insoluble oxalate salts in the cellulose extracted by DES.
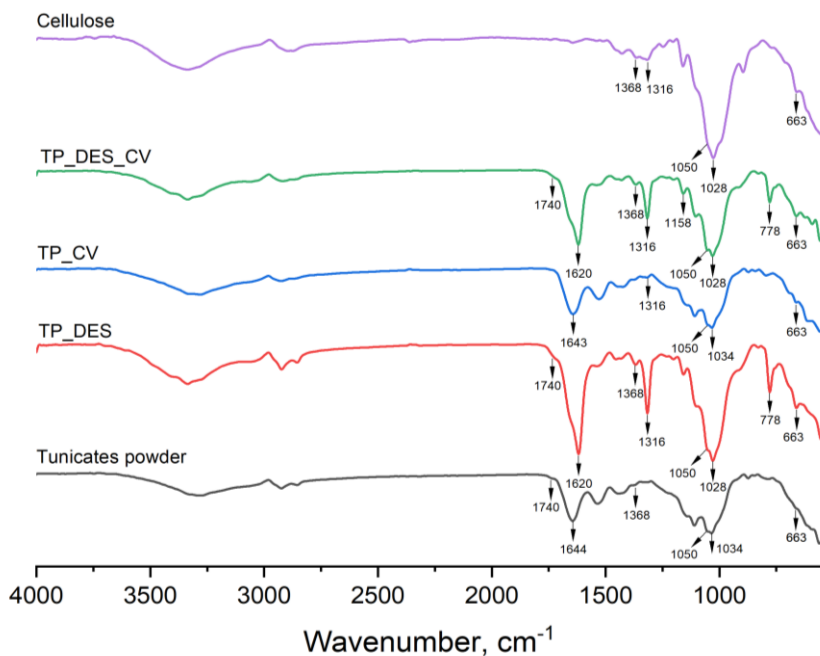


Fig.4.16 FT-IR spectra of TP (black), cellulose reference (magenta) and TP treated with DES (red), CV (blue) and DES+CV (green)

The samples after treatment with DES and carvacrol were also investigated by Solid-state NMR spectroscopy (Fig. 4.17).
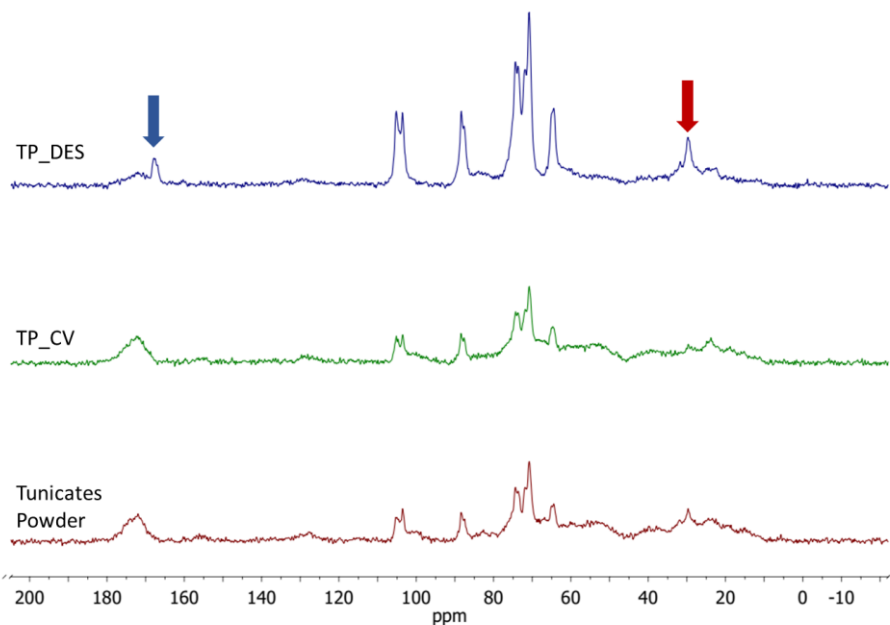
Fig. 4.17 $^{13}$C CP/MAS spectra of TP (red), TP treated with carvacrol (green), TP treated with DES (blue)

The $^{13}$C CP/MAS spectrum of the TP after treatment with carvacrol, (Fig. 4.17 green) shows only the disappearance of the signal at 30 ppm, which is usually assigned to the methylene carbon of aliphatic chains. The 13C CP/MAS spectrum of the TP after DES treatment (Fig. 4.17 blue) shows signals related only to cellulose and a small amount of lipids, besides traces of oxalate (blue arrow) and choline (red arrow).

To investigate the morphological structure of pristine TP and TP after the MW-assisted DES treatment at 85°C for 60 min, SEM analyses were performed (Fig.4.18). SEM image of the material recovered after DES treatment revealed the presence of the extracted cellulosic material as long fibrils (Fig. 4.18b-c). The presence of long cellulose fibrils and a reticular structure indicated the presence of a small residual lipid content that gave to the extracted material a film-like consistency. The fibril length obtained from tunicates was between 100 mm and 1000 mm, with a cross-sectional diameter of about 10-30 mm (Fig. 4.18c). In addition, Fig. 4.18c shows the presence of granular inorganic salts besides cellulose fibrils.
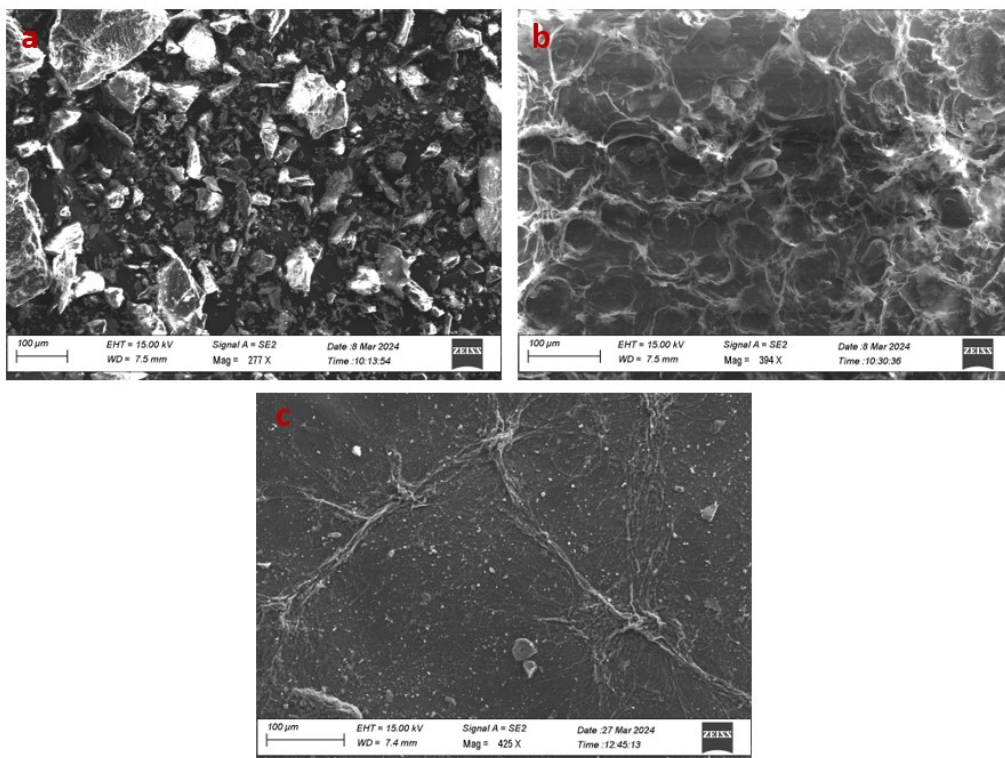
Fig.4.18 SEM micrographs of: (a) pristine TP; (b) TP after DES treatment process analyzed as solid paste; (c) TP after DES treatment process analyzed as diluted water suspension after homogenizing process (the SEM specimen was dried before analysis)

## 4.4. Extraction of cellulose from tunicates with traditional methods

At present, the main extraction methods of cellulose in tunicate are alkali treatment and the kraft paper process [75]. However, all the extraction examples reported in literature have been carried out on tunicates that previously removed of the internal organs. To compare the efficiency of cellulose extraction using DES and the standard method, cellulose was extracted from TP according to the methodology reported by Dunlop [85], with some modifications. The treatment was carried out in two steps, as detailed in the experimental part. The first step was deproteinization of TP in 5% NaOH solution at 80°C for 24 hours. The second stage was bleaching in an aqueous solution of sodium chlorite and acetic acid at 60°C.

TGA and DTG curves of tunicate powder before treatment, after step 1 extraction and after step 2 extraction are reported in Fig.4.19 and Fig.4.20 respectively. Since a different instrument with lower nitrogen flow was used for TGA of the standard extraction samples, the main peaks were shifted in contrast to the above samples. The TGA curve of the sample after the step 1 of treatment (Fig.4.19 blue line) shows a mass loss of approximately 40% within 300-400°C. In contrast, the sample after two subsequent steps of treatment (Fig.4.19 green line) exhibits a mass loss of over 60%.
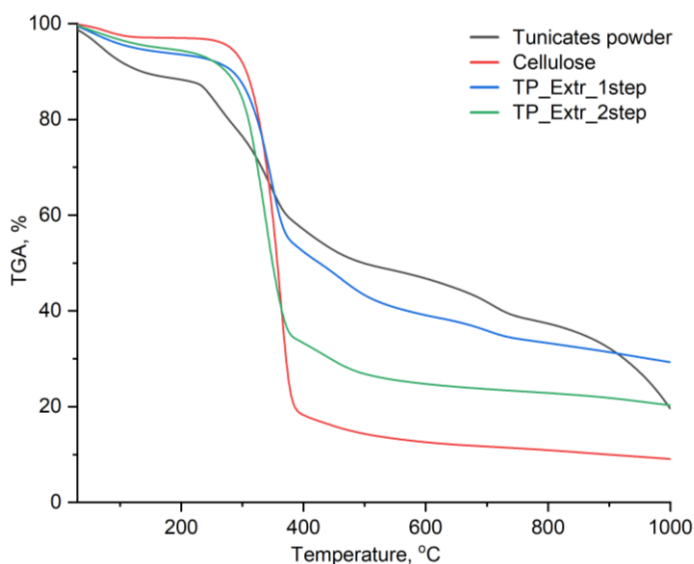


Fig.4.19 TGA curves of pristine TP, cellulose and TP after first and second step of extraction

The purification first step shows complete removal of proteins, but it is not effective in removing lipids and carbonates, as shown by the DTG peaks at 467°C and 707°C (Fig. 4.20, blue). After the second step of extraction, these peaks are absent (Fig. 4.20, green), indicating the effectiveness of treatment with a mixture of sodium chlorite and acetic acid in lipids and carbonates removal.
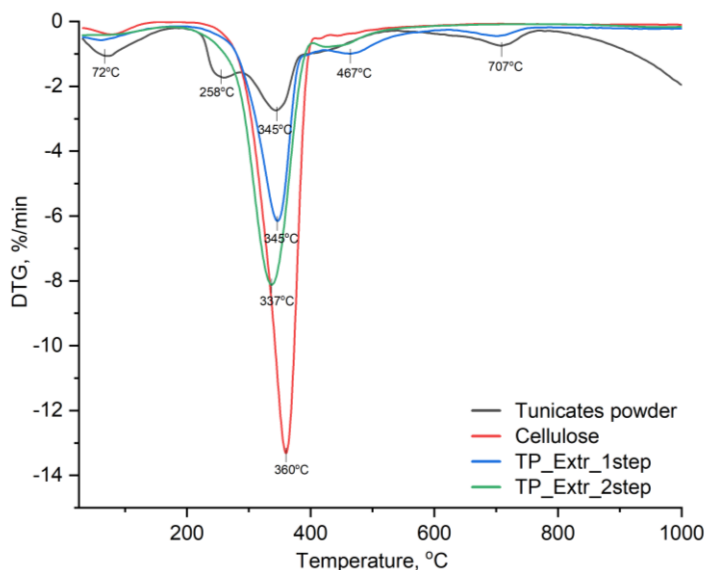
Fig.4.20 DTG curves of pristine TP, cellulose and TP after first and second step of extraction

Comparison of the extraction methods by conventional two-step method and DES extraction are shown in Fig. 4.21 and 4.22. As illustrated by the thermogravimetric analysis curves (Fig. 4.21), the efficiency of the two-stage extraction of cellulose from tunicates is comparatively higher than that of the DES extraction. However, the long extraction time, energy and reagents cost consumed, are significantly higher than the advantage in cellulose yield.
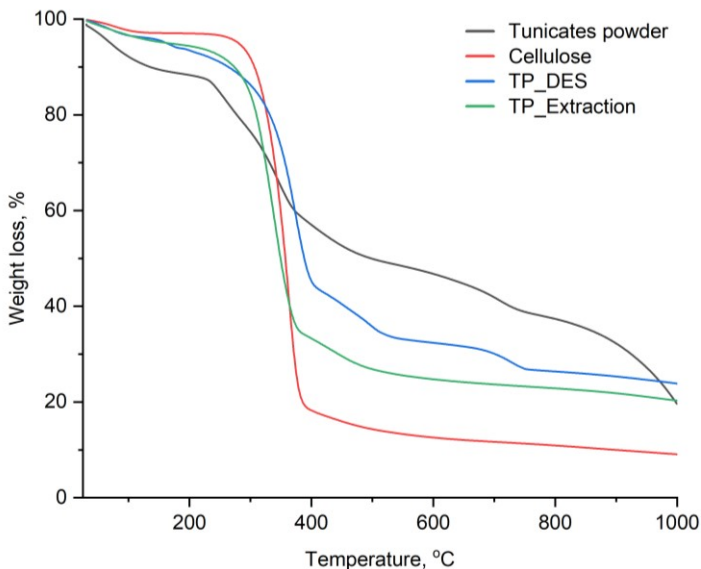
Fig.4.21 TGA curves of pristine TP, cellulose and TP after extraction by DES and standard extraction
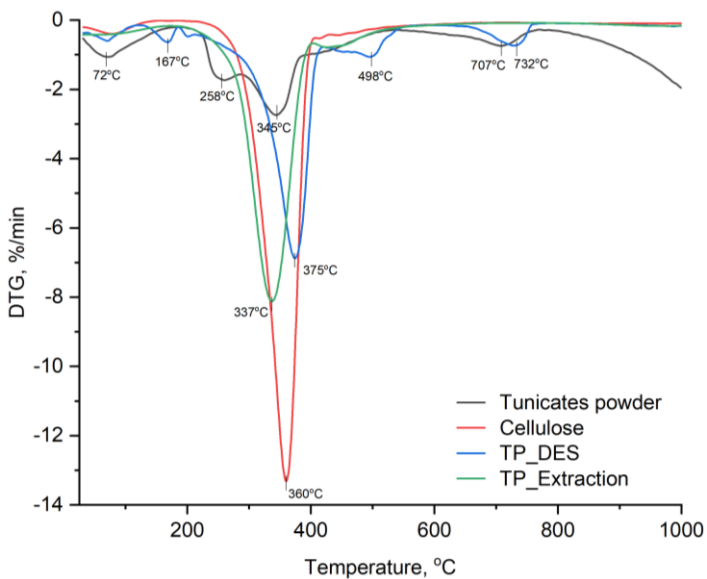


Fig.4.22 DTG curves of pristine TP, cellulose and TP after extraction by DES and standard extraction

## 4.5. Conclusions

The innovative extraction system based on the use of an acidic DES (choline chloride and oxalic acid in 1:1 molar ratio) under microwave irradiation at 85°C seems to be promising for obtaining cellulose from tunicates. TGA, FTIR, NMR and SEM analyses were used to characterize the extracted cellulosic material obtained from the DES treatment process. However. the properties of the cellulosic residue suggest the need for further investigation to identify the best purification process. Extracted tunicate cellulose may be of great interest for applications in various fields such as biomedicine, energy and electronics, polymer reinforced materials, food packaging, paper and environmental engineering, therefore the proposed protocol using DES for cellulose extraction could be of interests for the valorisation of waste products from the aquaculture sector.

# 5. EXPERIMENTAL PART

## 5.1. Cu/Steel Slags catalysts

### 5.1.1 Synthesis of Cu /Steel Slags catalysts

#### 10% Cu/Steel Slags precursor

0.786 g (3.14 mmol) of copper sulphate pentahydrate ($CuSO_4 \cdot 5H_2O$) was dissolved in 50 ml of $H_2O$ in round bottom flask, and then added of 1.8 g of Steel Slags and 50 ml of $H_2O$. The flask was placed in an oil bath at $40^{o}C$ for 2 hours under magnetic stirring. Afterwards, the solid material was separated by centrifugation and washed 3 times with water (3 x 25 mL). The obtained grey paste was dried at $80^{o}C$ in oven overnight. Yield = 1.955 g of 10%Cu/Steel Slags precursor was obtained.

#### 10%Cu/Steel Slags catalyst reduced by $H_2$

Reduction copper particles from $Cu^{2+}$ to $Cu^{0}$ was performed by calcination of 1.5 g of 10% Cu/Steel Slags precursor in steel reactor under 5.0 bar of $H_2$ at $300^{o}C$ for 1 hour. Yield = 1.43 g

#### 10%Cu/Steel Slags catalyst reduced by $NaBH_4$

0.786 g (3.14 mmol) of copper sulphate pentahydrate ($CuSO_4 \cdot 5H_2O$) was dissolved in 50 ml of $H_2O$ in round bottom flask, and then added of 1.8 g of Steel Slags and 50 ml of $H_2O$. The flask was placed in an oil bath at $40^{o}C$ for 2 hours under magnetic stirring. Afterwards, a 1 M $NaBH_4$ solution was added dropwise until the color of the suspension changed from grey to black. The resulting mixture was left at room temperature overnight until bubbling ended. Subsequently, the black solid part was separated by centrifugation and washed 3 times with water (3 x 25 mL). The obtained dark grey paste was dried at $80^{o}C$ in an oven overnight. Yield = 1.864 g of 10%Cu/Steel Slags catalyst reduced by $NaBH_4$ was obtained.

#### 15% Cu/Steel Slags precursor

1.777 g (4.72 mmol) of copper sulphate pentahydrate ($CuSO_4 \cdot 5H_2O$) was dissolved in 50 ml of $H_2O$ in round bottom flask, and then added of 1.7 g of Steel Slags

and 50 ml of $H_2O$. The flask was placed in an oil bath at 40°C for 2 hours under magnetic stirring. Afterwards, the solid part was separated by centrifugation and washed 3 times with water (3 x 25 mL). The obtained grey paste was dried at 80°C in an oven overnight. Yield = 2.024 g of 15%Cu/Steel Slags precursor was obtained.

### 15%Cu/SteelSlags catalyst reduced by $H_2$

Reduction copper particles from $Cu^{2+}$ to $Cu^0$ was performed by calcination of 1.0 g of 15% Cu/Steel Slags precursor in steel reactor under 5.0 bar of $H_2$ in 300°C during 1 hour. Yield = 0.95 g

### 15%Cu/SteelSlags catalyst reduced by $NaBH_4$

1.777 g (4.72 mmol) of copper sulphate pentahydrate ($CuSO_4 \cdot 5H_2O$) was dissolved in 50 ml of $H_2O$ in round bottom flask. After complete dissolving and 1.7 g of Steel Slags and 50 ml of $H_2O$ were added. Flask was placed in oil bath in 40°C for 2 hours with magnet stirrer mixing. After 2 hours 1 M $NaBH_4$ solution was added dropwise until color changing from gray to black. The resulted mixture was at room temperature during night until bubbling ended. After black solid part was separated by centrifugation and washed 3 times with water (3 x 25 mL). Washed dark grey paste was dried in 80°C oven during night. Yield = 1.696 g of 15%Cu/SteelSlags catalyst reduced by $NaBH_4$ was obtained.

### 20% Cu/Steel Slags precursor

1.571 g (6.29 mmol) of copper sulphate pentahydrate ($CuSO_4 \cdot 5H_2O$) was dissolved in 50 ml of $H_2O$ in round bottom flask. After complete dissolving, 1.6 g of Steel lags and 50 ml of $H_2O$ were added. The flask was placed in oil bath at 40°C for 2 hours with magnet stirrer mixing. Then, the solid part was separated by centrifugation and washed 3 times with water (3 x 25 mL). The obtained grey paste was dried at 80°C in oven overnight. Yield = 2.318 g of 20%Cu/SteelSlags precursor was obtained.

*20%Cu/SteelSlags catalyst reduced by H₂*

Reduction copper particles from $Cu^{2+}$ to $Cu^0$ was performed by calcination of 2.0 g of 20% Cu/Steel Slags precursor in steel reactor under 5.0 bar of $H_2$ in 300°C during 1 hour. Yield = 1.95 g

*20%Cu/SteelSlags catalyst reduced by NaBH₄*

1.571 g (6.29 mmol) of copper sulphate pentahydrate ($CuSO_4 \cdot 5H_2O$) was dissolved in 50 ml of $H_2O$ in round bottom flask, and then added of 1.6 g of Steel Slags and 50 ml of $H_2O$ were added. The flask was placed in an oil bath at 40°C for 2 hours under magnetic stirring. Afterwards, a 1 M $NaBH_4$ solution was added dropwise until the color of the suspension changed from grey to black. The resulted mixture was left at room temperature overnight until bubbling ended. Then, the black solid part was separated by centrifugation and washed 3 times with water (3 x 25 mL). The obtained dark grey paste was dried at 80°C in an oven overnight. Yield = 1.56 g of 20%Cu/SteelSlags catalyst reduced by $NaBH_4$ was obtained.

*15%Cu/SteelSlags precursor with mixing time 15h*

2.223 g (9.44 mmol) of copper sulphate pentahydrate ($CuSO_4 \cdot 5H_2O$) was dissolved in 100 ml of $H_2O$ in round bottom flask, and then added of 3.4 g of Steel Slags and 100 ml of $H_2O$. The flask was placed in an oil bath at 40°C for 15 hours under magnetic stir. Afterwards, the solid part was separated by centrifugation and washed 3 times with water (3 x 25 mL). The resulting grey paste was dried at 80°C in an oven overnight. Yield = 4.470 g of 15%Cu/SteelSlags precursor with mixing time 15h was obtained.

*15%Cu/SteelSlags precursor with ultrasonic pretreatment*

3.4 g of Steel Slags and 100 ml of $H_2O$ were mixed in round bottom flask for 10 min and ultrasonicated for 10 min. At the same time 2.223 g (9.44 mmol) of copper sulphate pentahydrate ($CuSO_4 \cdot 5H_2O$) was dissolved in 100 ml of H2O and then added to the first mixture. The flask was placed in an oil bath at 40°C for 2 hours under magnetic stirring. Afterwards, the solid part was separated by centrifugation and washed 3 times with water (3 x 25 mL). The obtained grey paste was dried at 80°C in an oven

overnight. Yield = 4.379 g of 15%Cu/SteelSlags precursor with ultrasonic pretreatment was obtained.

## 5.1.2 Catalytical tests

### General procedure for reduction of nitroarenes

0.5 mmol (61.55 mg) of nitrobenzene, 3.0 mmol (113.4 mg) of NaBH$_4$, 50 mg of Cu/SS catalyst and deionized water (5 mL) were added in a round-bottom flask (25 mL) equipped by a gas bubbler to discharge the hydrogen excess produced during reaction. The mixture was stirred at room temperature (25$^o$C) for 2h. After reaction completion the product was extracted with ethyl acetate (5 mL) and analyzed by GS-MS with the internal standard method (diphenyl).

### Recycling test

2.0 mmol (246.22 mg) of nitrobenzene, 6.0 mmol (113.4 mg) of NaBH$_4$, 200 mg of Cu/SS catalyst and deionized water (10 mL) were added in a round-bottom flask (25 mL) equipped by a gas bubbler and the mixture was stirred at room temperature (25$^o$C) for 2h. After reaction completion the product was extracted with ethyl acetate (5 mL) and analyzed by GS-MS with the internal standard method (diphenyl). After each cycle of reaction, the catalyst was washed with deionized water (3 x 15 mL) and methanol (15 mL), dried at 80°C and used for a subsequent run.

## 5.2. Tunicates

### 5.3.1 Sample preparation and analysis

Colonies of *C. oblonga* were collected from the mussel farming ropes. Colonial zooids were manually detached from the mussels and ropes, washed with seawater, and frozen at -86 °C until further analyses. Prior to the laboratory analyses, all samples were thawed and first rinsed with tap water and then with deionized water in order to remove seawater and impurities. For analyses, all tissues of *C. oblonga* were processed in their entirety, freeze-dried for 72 hours in the CoolSafe lyophilizer (55-9 PRO model, Labogene, Denmark) and pulverized in the vibrational cryogenic mill (SPEX SamplePrep Freezer/Mill 6875, USA).

**Proximate composition.** Moisture (water) content was determined gravimetrically after drying to constant weight at 103 ± 2°C as recommended by Official Methods (AOAC, 1995). Mineral content (ash) was determined by combusting 5 g of sample at 550°C and weighing the ash after cooling (AOAC, 1995). Crude protein was analysed by Kjeldahl method and calculated from nitrogen content using conversion factor N × 6.25 (AOAC, 1995). Crude fat content was determined by the two step extraction with cyclohexane and propan-2-ol mixtures as solvents (Smedes, 1999). After extraction, solvents were evaporated under vacuum, extracted lipids were dried for 3 hours at 103 ± 2°C and weighed.

### 5.3.2 Cellulose extraction procedures

**Extraction by DES (TP_DES).** 10.5 g of Choline Chloride and 9.5 g of Oxalic Acid were placed in oil bath at 80°C until homogeneous transparent solution was obtained. Afterwards, 1.0 g of tunicate powder (TP) was added to DES solution and treated in Microwave reactor at 80/85/90 °C for 30 min or 1 h. After cooling, deionized water (25 mL) was added, and the resulting mixture was filtrated by glass filter and washed 2 times with 50 ml of deionized water. The obtained wet brown paste was removed from the filter surface, dried overnight at 85 °C and ground to a homogeneous powder by mortar.

**Extraction by carvacrol (TP_CV).** 0.5 g of tunicates powder (TP) and 5.0 g of carvacrol were mixed at room temperature for 1 hour. The mixture obtained was centrifugated and the solid part was washed with 96% Ethanol (4 times, 10 ml) until obtaining a colorless washing liquid. Next, the solid part was dried overnight at 85 °C in an oven.

**2 step extraction by DES and carvacrol (TP_DES_CV).** 0.247 g of TP_DES powder (obtained at treating temperature of 85°C) and 2.5 g of carvacrol were mixed at room temperature for 1 hour. The mixture obtained was centrifugated and the solid part was washed with 96% Ethanol (4 times, 10 ml) until obtaining a colorless washing liquid. Next, the solid part was dried overnight at 85 °C in oven.

102

**2 step extraction.** 3.0 g of tunicates powder and 45 mL of 5% sodium hydroxide solution were placed in a round bottom flask, covered and mixed intensively with a magnetic stirrer at 80 °C for 24 hours. The resulting solution was filtered through a paper filter, the solid precipitate was washed with deionized water until the filtrate was below a pH of 10. The resulting paste was placed in 50 mL of deionized water and mixed at 60 °C. The pH of the solution was then adjusted to 5.5 by adding glacial acetic acid dropwise. Under strong stirring, 100 mg of 80% purity $NaClO_2$ powder and 0.5 mL of glacial acetic acid were added to the reaction mixture. The reaction was covered and allowed to react for 1 hour at 60 °C with periodic stirring. Then a second addition of 100 mg $NaClO_2$ and 0.5 mL of glacial acetic acid was added and stirred for 1 hour. Three more additions of $NaClO_2$ and glacial acetic acid were made in the same fashion. The product was then allowed to cool and settle overnight, followed by filtering through a paper filter, washing with deionized water and drying at 80 °C.

## 5.3. Analysis

### X-ray fluorescence analysis (XRF)

Elemental analysis was provide using a portable energy dispersive XRF spectrometer NITON™ XL3t, Thermo Scientific (Waltham, USA) with Ag collimator source (spot size ∼ 6 mm) operating at 50 kV and 40 μA, and is equipped with a large area SDD detector (160 eV resolution @ Mn Kα). Each sample was analyzed in triplicate for 120 s (live time) and the results averaged. Quantitative data were obtained using the Thermo-NITON instrument proprietary software (NDTR version 6.5.2).

### Fourier-transform infrared spectroscopy (FT-IR)

Fourier Transform Infrared FT-IR spectra of samples were recorded on a Jasco FT/IR 4200 spectrophotometer in ATR (Attenuated Total Reflectance) mode with diamond crystal as focusing component in wavenumber range 4000-400 $cm^{-1}$.

### X-ray diffraction (XRD)

X-ray powder diffraction data were collected in air using a PANalytical Empyrean X-ray diffractometer with Bragg-Brentano geometry, large beta filter-Nickel, detector (PIXcel3D) and CuKα radiation, operating at 40 kV/40 mA. The powder was deposited on a PANalytical powder sample holder for the flat-plate Bragg-Brentano geometry. The X-ray data were collected in the 2θ range 10-85° (step size 0.026°, Counting time (s): 330.990). The diffraction patterns were processed using the PANalytical B.V. software HIGHScore Plus version 3.0e.

### Thermogravimetric Analysis (TGA) and Differential Scanning Calorimetry (DSC)

Thermogravimetric Analysis (TGA) and Differential Scanning Calorimetry (DSC) were performed in a nitrogen flow (100 mL $min^{-1}$) with a SDT Q600 TA Instruments in the range from 30 to 1000°C with a heating rate of 10°C min

### Field-emission scanning electron microscopy (FESEM)

A Field-emission scanning electron microscopy FESEM Zeiss Σigma 300 VP (Zeiss Oberkochen, Germany) equipped with an energy dispersive spectrometer (EDS) C-MaxN SDD (Oxford Instruments, Oxford, U.K.) with an active area of 20 $mm^2$ (Oxford Instruments, Oxford, U.K.) was used to perform analysis on the selected samples.

### Nuclear magnetic resonance (NMR)

NMR experiments were conducted using a Bruker Avance 400 spectrometer equipped with a 5 mm inverse broadband (BBI) probe. All acquisitions were carried out at 298 K using the following parameters: 32 scans, a time domain of 64 k data points, an acquisition time of 4,08 s, a spectral width of 20 ppm centered at 4,7 ppm, a recycle delay of 10 seconds. The spectra were calibrated at 0 ppm using the signal of TMS as primary standard reference and the solvent residual peak as secondary standard which are respectively 2.50 ppm for DMSO-$d_5$ and 7.26 ppm for chloroform.

### Solid-state nuclear magnetic resonance (Solid-state NMR)

Solid-state NMR analyses were performed on a Avance I 400 spectrometer (Bruker Biospin GMBH, Rheinstetten, Germany) (operating at a frequency of 100.6 MHz for $^{13}$C) using a 4.0 mm HX MAS probe at 298 K. For the MAS experiments, the samples were packed into zirconia rotors. The chemical shifts for $^{13}$C were referenced against SiMe$_4$ (0 ppm) by using the methylene signal of adamantane ($\delta$ 38.48) as a secondary reference. The $^1$H-$^{13}$C CP/MAS NMR experiments were acquired using an acquisition time of 30 msec, a spectral width of 50 kHz (500 ppm) centered at 100 ppm, a 3.25 μs proton $\pi/2$ pulse length, an nCP of 55.0 kHz, a contact time of 1.0 ms, a dec of 76.9 kHz, and a recycle delay of 6.0 s. For all samples the number of scans were 512. The spinning rate for the $^1$H-$^{13}$C CP/MAS NMR spectra was 9 kHz. A two-pulse phase modulation (TPPM) decoupling scheme was used for the $^1$H decoupling.

### Fatty acid composition

Lipids for determination of fatty acid composition were extracted according to Smedes (1999). In order to preserve unsaturated fatty acids form oxidation, the final step of the Smedes method i.e., drying at 103 °C was excluded from the protocol. Fatty acid methyl esters were prepared by transesterification with methanol according to ISO 5509:2000 method (ISO, 2000). Briefly, 60 mg of extracted lipids was dissolved in 4 mL of isooctane and 200 μL of potassium hydroxide in methanol (2 mol/L) were added. Mixture was vortexed for 30 s and left for a few minutes at room temperature to react. Afterwards, 1 g of sodium hydrogen sulphate monohydrate was added, mixed, and clear supernatant containing methyl esters was transferred into the vial.

For gas chromatographic analysis, 1 μL of prepared methyl esters was injected into the Agilent Technologies 6890N Network GC system (Santa Clara, CA, USA) equipped with flame ionization detector. Fatty acid methyl esters (FAME) were separated on a DB-23 capillary column (60 m × 0.25 mm × 0.25 μm, Agilent Technologies). Helium was used as a carrier gas with a constant flow of 1.5 mL/min. The injector temperature was set at 250 °C and detector at 280 °C. The oven temperature was programmed to increase by 7 °C/min from initial 60 °C to final temperature of 220 °C where it was held for 17 min. The split ratio was 30:1. Fatty acids were identified by comparing

their retention times with the retention times of 37 Component FAME Mix (Supelco, Sigma-Aldrich, St. Louis, Missouri, USA). The surface normalization method was used to determine the quantitative composition of fatty acids expressed as the percentage of total fatty acids.

Saturated fatty acids (SFA) were calculated as the sum of C:14, C:15, C:16, C:17, C:18, C:20 and C:22. Monounsaturated fatty acids (MUFA) were calculated as the sum of C16:1, C18:1 trans, and C18:1 cis. Polyunsaturated fatty acids (PUFA) were calculated as the sum of C18:2 cis, C18:3n3, C20:4n6, and C22:6n3. Unsaturated fatty acids (UFA) were calculated as the sum of MUFA an PUFA. $\omega$-3 fatty acids were calculated as the sum of C18:3n3 and C22:6n3. $\Omega$-6 fatty acids were calculated as the sum of C20:4n6 and C18:2 cis.

Prior to analysis, subsamples (0.1 g) of lyophilized tunicates were subjected to a total digestion in the microwave oven (Multiwave ECO, Anton Paar, Graz, Austria) in a one-step procedure consisting of digestion with a mixture of 6 mL nitric acid ($HNO_3$) and 0.1 mL hydrofluoric acid (HF). After digestion, samples were acidified with 2% (v/v) HNO3 without further dilution.

### Multielement analysis

Multielement analysis was performed by triple quadrupole inductively coupled plasma mass spectrometer (ICP-QQQ, 8900, Agilent, USA). All prepared solutions of lyophilized *C. oblonga* were analysed for total concentration of 32 trace elements (Ag, Al, As, Ba, Be, Bi, Cd, Co, Cr, Cs, Cu, Fe, Li, Mn, Mo, Nb, Ni, Pb, Rb, Sb, Sc, Se, Sn, Sr, Th, Ti, Tl, U, V, W, Y, and Zn) and 6 macroelements (Ca, K, Mg, Na, P, and S). Indium (In, 1 mg/L) was used as an internal standard. Quality control of analytical procedure used for element analysis was performed by simultaneous analysis of the blank and certified reference material Mussels (NCS ZC 78005, also known as GBW- 08571, China National Analysis Centre for Iron and Steel, Peking, China).

# CONCLUSIONS

The present work focused on the possibilities of converting three distinct categories of wastes (industrial, municipal, and natural wastes) into valuable resources following the circular economy principles, and solving at the same time the problems connected to their correct disposal. This kind of valorization can be achieved through the production of sustainable advanced materials and catalysts. The studied industrial wastes were steel slags, the municipal ones were spent cigarette butts, and the natural ones were invasive tunicates, dangerous for aquicultural activities.

Concerning the industrial steel slags, a series of copper and iron oxide catalysts supported onto them were synthesized. The Cu/Steel Slags catalysts showed high activity in the reduction of nitroarenes in water, in the presence of sodium borohydride as the reducing agent at room temperature. The catalyst precursor did not require any pre-reduction and the conversion of $Cu^{2+}$ to $Cu°$ in the active form occurred "in situ" under reaction conditions. Moreover, the catalytic system was active and selective for at least five subsequent cycles. The FeOx/Steel Slags catalysts were employed in the catalytic transfer hydrogenation of nitrobenzene in the presence of isopropanol as the hydrogen source, without adding any external base. This kind of reaction presents a significant challenge due to its reliance on a green hydrogen source, which often necessitates the addition of toxic sodium or potassium hydroxide. However, the use of steel slags as support allowed to successfully catalyze the reaction without the requirement for an external base, due to their high basicity features.

In the case of cigarette butts, the extraction of cellulose acetate in a unconventional and ecosustainable way was exploited. To facilitate the recovery of cellulose acetate polymer from cigarette butt waste, a protocol for the efficient cleaning of cigarette filters was systematically developed and optimized. Various green solvents, including water (with controlled temperature variation), NaCl solutions (with variable concentration), and ethanol (with varying concentration), were tested to establish optimal purification conditions. 75% ethanol-water solvent mixture achieved comprehensive removal of tobacco combustion products.

The valorization of aquaculture waste, in particular the invasive tunicate species *Clavelina oblonga*, for the production of cellulose has also been considered. Extracted tunicate cellulose is of great interest for applications in various fields such as biomedicine, energy and electronics, etc. An innovative extraction system consisting of acid DES (choline chloride and oxalic acid in molar ratio of 1:1) under microwave irradiation at 85°C for 60 min was used for cellulose extraction. The material properties after DES treatment are comparable to conventional alkali and acid purification, demonstrating the potential of using DES for cellulose extraction from tunicates. Simultaneously, we worked on enhancing the efficiency of the conventional two-stage extraction of cellulose from tunicates, by substituting with the use of DES, avoiding time-energy-reagent consuming protocols.

# LIST OF FIGURES

## Chapter 3

## Chapter 4

Fig.4.21 TGA curves of pristine TP, cellulose and TP after extraction by DES and standard extraction

Fig.4.22 DTG curves of pristine TP, cellulose and TP after extraction by DES and standard extraction

# LIST OF TABLES

# ACKNOWLEDGEMENTS

# BIBLIOGRAPHY

1. Geissdoerfer, M., Savaget, P., Bocken, N.M. and Hultink, E.J., 2017. The Circular Economy–A new sustainability paradigm?. *Journal of cleaner production*, 143, pp.757-768. DOI: 10.1016/j.jclepro.2016.12.048

2. MacArthur, E., 2013. Towards the circular economy. *Journal of Industrial Ecology*, 2(1), pp. 23-44.

3. Geng, Y. and Doberstein, B., 2008. Developing the circular economy in China: Challenges and opportunities for achieving 'leapfrog development'. *The International Journal of Sustainable Development & World Ecology*, 15(3), pp.231-239. DOI: 10.3843/SusDev.15.3:6

4. Stahel, W.R., 2016. The circular economy. *Nature*, 531(7595), pp.435-438. DOI: 10.1038/531435a

5. UNECE. (2024) 'Circular Economy. Trade and Economic Cooperation for Circular Economy'. Available at: https://unece.org/trade/CircularEconomy (Accessed: 01 October 2024).

6. Kabongo, J.D.б 2013. Design for Environment. In: Idowu, S.O., Capaldi, N., Zu, L., Gupta, A.D. (eds) *Encyclopedia of Corporate Social Responsibility*. Springer, Berlin, Heidelberg. DOI: 10.1007/978-3-642-28036-8_40

7. Bosmans, A., Vanderreydt, I., Geysen, D. and Helsen, L., 2013. The crucial role of Waste-to-Energy technologies in enhanced landfill mining: a technology review. *Journal of Cleaner Production*, 55, pp.10-23. DOI: 10.1016/j.jclepro.2012.05.032.

8. Barragan, J.A., Ponce de León, C., Alemán Castro, J.R., Peregrina-Lucano, A., Gómez-Zamudio, F. and Larios-Durán, E.R., 2020. Copper and antimony recovery from electronic waste by hydrometallurgical and electrochemical techniques. *ACS omega*, *5*(21), pp.12355-12363. DOI: 10.1021/acsomega.0c01100

9. Gumisiriza, R., Hawumba, J.F., Okure, M. and Hensel, O., 2017. Biomass waste-to-energy valorisation technologies: a review case for banana processing in Uganda. *Biotechnology for biofuels*, 10, pp.1-29. DOI: 10.1186/s13068-016-0689-5

10. Energy, Climate change, Environment. (2023) 'Waste Framework Directive'. Available at: https://environment.ec.europa.eu/topics/waste-and-recycling/waste-framework-directive_en (Accessed: 04 October 2024).

11. Baras, A., Li, J., Ni, W., Hussain, Z. and Hitch, M., 2023. Evaluation of potential factors affecting steel slag carbonation. *Processes*, 11(9), p.2590. DOI: 10.3390/pr11092590

12. Shi, C., 2004. Steel slag—its production, processing, characteristics, and cementitious properties. *Journal of materials in civil engineering*, 16(3), pp.230-236. DOI: 10.1061/(ASCE)0899-1561(2004)16:3(230)

13. Chandel, S.S., Singh, P.K., Katiyar, P.K. and Randhawa, N.S., 2023. A Review on Environmental Concerns and Technological Innovations for the Valorization of Steel Industry Slag. *Mining, Metallurgy & Exploration*, 40(6), pp.2059-2086. DOI: 10.1007/s42461-023-00886-z

14. Pasetto, M., Baliello, A., Giacomello, G. and Pasquini, E., 2023. The use of steel slags in asphalt pavements: A state-of-the-art review. *Sustainability*, 15(11), p.8817. DOI: 10.3390/su1511

15. Dell'Anna, M. M., et al, 2020. Assessing environmental impacts in using waste steel slags as construction materials in a highly industrialized area. *Aquatic Ecosystem Health & Management*, 23(4), pp. 474-482. DOI: 10.1080/14634988.2020.1827820

16. Wang, et al., 2021. A review of the application of steel slag in $CO_2$ fixation. *ChemBioEng Reviews*, 8(3), pp.189-199. DOI: 10.1002/cben.202000021

17. Wang, F.P., Liu, T.J., Cai, S., Gao, D., Yu, Q., Wang, X.M., Wang, Y.T., Zeng, Y.N. and Li, J.G., 2021. A review of modified steel slag application in catalytic pyrolysis, organic degradation, electrocatalysis, photocatalysis, transesterification and carbon capture and storage. *Applied Sciences*, 11(10), p.4539. DOI: 10.3390/app11104539

18. Dimitrova, S., Ivanov, G. and Mehandjiev, D., 2004. Metallurgical slag as a support of catalysts for complete oxidation in the presence of ozone. *Applied Catalysis A: General*, 266 (1), pp.81-87. DOI: 10.1016/j.apcata.2004.01.029

19. Yu, H., Ma, T., Shen, Y. and Chen, D., 2017. Experimental study on catalytic effect of biomass pyrolysis volatile over nickel catalyst supported by waste iron

slag. *International Journal of Energy Research*, 41(14), pp.2063-2073. DOI: 10.1002/er.3767

20. Kabir, G., Din, A.M. and Hameed, B.H., 2018. Pyrolysis of oil palm mesocarp fiber catalyzed with steel slag-derived zeolite for bio-oil production. *Bioresource technology*, 249, pp.42-48. DOI: 10.1016/j.biortech.2017.09.190

21. Kholkina, E., Kumar, N., Ohra-aho, T., Lehtonen, J., Lindfors, C., Perula, M., Peltonen, J., Salonen, J. and Murzin, D.Y., 2020. Transformation of industrial steel slag with different structure-modifying agents for synthesis of catalysts. *Catalysis Today*, 355, pp.768-780. DOI: 10.1016/j.cattod.2019.04.033

22. Kar, Y. and Gürbüz, Z., 2016. Application of blast furnace slag as a catalyst for catalytic cracking of used frying sunflower oil. *Energy Exploration & Exploitation*, 34(2), pp.262-272. DOI: 10.1177/0144598716630160

23. Okoye, P.U., Abdullah, A.Z. and Hameed, B.H., 2017. Stabilized ladle furnace steel slag for glycerol carbonate synthesis via glycerol transesterification reaction with dimethyl carbonate. *Energy Conversion and Management*, 133, pp.477-485. DOI: 10.1016/j.enconman.2016.10.067

24. Liu, G., Yang, J. and Xu, X., 2020. Synthesis of hydrotalcite-type mixed oxide catalysts from waste steel slag for transesterification of glycerol and dimethyl carbonate. *Scientific Reports*, 10(1), p.10273. DOI: 10.1038/s41598-020-67357-z

25. Guo, F., Liang, S., Zhao, X., Jia, X., Peng, K., Jiang, X. and Qian, L., 2019. Catalytic reforming of biomass pyrolysis tar using the low-cost steel slag as catalyst. *Energy*, 189, p.116161. DOI: 10.1016/j.energy.2019.116161

26. Chen, A., Tian, Z., Han, R., Wei, X., Hu, R. and Chen, Y., 2021. Preparation of Ni-based steel slag catalyst by impregnation method for sludge steam gasification. *Sustainable Energy Technologies and Assessments*, 47, p.101553. DOI: 10.1016/j.seta.2021.101553

27. Fusco, C., Casiello, M., Pisani, P., Monopoli, A., Fanelli, F., Oberhauser, W., Attrotto, R., Nacci, A. and D'Accolti, L., 2022. Steel slag as low-cost catalyst for artificial photosynthesis to convert $CO_2$ and water into hydrogen and methanol. *Scientific Reports*, 12(1), p.11378. DOI: 10.1038/s41598-022-15554-3

28. Santos, J., Jahangiri, H., Bashir, M.A., Hornung, A. and Ouadi, M., 2020. The upgrading of bio-oil from the intermediate pyrolysis of waste biomass using steel slag as a catalyst. *ACS Sustainable Chemistry & Engineering*, 8(50), pp.18420-18432. DOI: 10.1021/acssuschemeng.0c05536

29. Casiello, M., Losito, O., Aloia, A., Caputo, D., Fusco, C., Attrotto, R., Monopoli, A., Nacci, A. and D'Accolti, L., 2021. Steel slag as new catalyst for the synthesis of fames from soybean oil. *Catalysts*, 11(5), p.619. DOI: 10.3390/catal11050619

30. Roushdy, M.H., 2022. Heterogeneous biodiesel catalyst from steel slag resulting from an electric arc furnace. *Processes*, 10(3), p.465. DOI: 10.3390/pr10030465

31. Slaughter, E., Gersberg, R.M., Watanabe, K., Rudolph, J., Stransky, C. and Novotny, T.E., 2011. Toxicity of cigarette butts, and their chemical components, to marine and freshwater fish. *Tobacco control*, 20, pp.25-i29. DOI: 10.1136/tc.2010.040170

32. Green, A.L.R., Putschew, A. and Nehls, T., 2014. Littered cigarette butts as a source of nicotine in urban waters. *Journal of hydrology*, 519, pp.3466-3474. DOI: 10.1016/j.jhydrol.2014.05.046

33. Serbruyns, L., Van de Perre, D. and Hölter, D., 2024. Biodegradability of cellulose diacetate in aqueous environments. *Journal of Polymers and the Environment*, 32(3), pp.1326-1341. DOI: 10.1007/s10924-023-03038-y

34. Dobaradaran, S., Schmidt, T.C., Lorenzo-Parodi, N., Kaziur-Cegla, W., Jochmann, M.A., Nabipour, I., Lutze, H.V. and Telgheder, U., 2020. Polycyclic aromatic hydrocarbons (PAHs) leachates from cigarette butts into water. *Environmental Pollution*, 259, p.113916. DOI: 10.1016/j.envpol.2020.113916

35. Lucia, G., Giuliani, M.E., d'Errico, G., Booms, E., Benedetti, M., Di Carlo, M., Fattorini, D., Gorbi, S. and Regoli, F., 2023. Toxicological effects of cigarette butts for marine organisms. *Environment International*, 171, p.107733. DOI: 10.1016/j.envint.2023.107733

36. Ghasemi, A., Golbini Mofrad, M.M., Parseh, I., Hassani, G., Mohammadi, H., Hayati, R. and Alinejad, N., 2022. Cigarette butts as a super challenge in solid waste management: a review of current knowledge. *Environmental Science and Pollution Research*, 29(34), pp.51269-51280. DOI: 10.1007/s11356-022-20893-9

37.  Torkashvand, J., Farzadkia, M., Sobhi, H.R. and Esrafili, A., 2020. Littered cigarette butt as a well-known hazardous waste: a comprehensive systematic review. *Journal of hazardous materials*, 383, p.121242. DOI: 10.1016/j.jhazmat.2019.121242

38.  Everaert, S., Schoeters, G., Lardon, F., Janssens, A., Van Larebeke, N., Raquez, J.M., Bervoets, L. and Spanoghe, P., 2023. Protecting public health and the environment: towards a general ban on cellulose acetate cigarette filters in the European Union. *Frontiers in Public Health*, 11, p.1282655. DOI: 10.3389/fpubh.2023.1282655

39.  Guang-yuan, Y.A.N.G., Lei, H.A.N., Shao-peng, D.E.N.G., Qiang, L.I.U. and Wen, W.A.N.G., 2022. On-site Rapid Determination of Content of Glycerol Triacetate in Cigarette Filter. *Journal of Instrumental Analysis*, 41(5), pp.792-796. DOI: 10.19969/j.fxcsxb.21082702

40.  Novotny, T.E., Lum, K., Smith, E., Wang, V. and Barnes, R., 2009. Cigarettes butts and the case for an environmental policy on hazardous cigarette waste. *International journal of environmental research and public health*, 6(5), pp.1691-1705. DOI: 10.3390/ijerph6051691

41.  Sassi, J.F. and Chanzy, H., 1995. Ultrastructural aspects of the acetylation of cellulose. *Cellulose*, *2*, pp.111-127. DOI: 10.1007/BF00816384

42.  Pang, J., Liu, X., Yang, J., Lu, F., Wang, B., Xu, F., Ma, M. and Zhang, X., 2016. Synthesis of highly polymerized water-soluble cellulose acetate by the side reaction in carboxylate ionic liquid 1-ethyl-3-methylimidazolium acetate. *Scientific reports*, 6(1), p.33725. DOI: 10.1038/srep33725

43.  Fischer, S., Thümmler, K., Volkert, B., Hettrich, K., Schmidt, I. and Fischer, K., 2008, January. Properties and applications of cellulose acetate. In *Macromolecular symposia* (Vol. 262, No. 1, pp. 89-96). Weinheim: WILEY-VCH Verlag. DOI: 10.1002/masy.200850210

44. Kamide, K., Okajima, K., Kowsaka, K. and Matsui, T., 1987. Solubility of cellulose acetate prepared by different methods and its correlationships with average acetyl group distribution on glucopyranose units. *Polymer journal*, 19(12), pp.1405-1412. DOI: 10.1295/polymj.19.1405

45. Azhar, O., Jahan, Z., Sher, F., Niazi, M.B.K., Kakar, S.J. and Shahid, M., 2021. Cellulose acetate-polyvinyl alcohol blend hemodialysis membranes integrated with dialysis performance and high biocompatibility. *Materials Science and Engineering: C*, 126, p.112127. DOI: 10.1016/j.msec.2021.112127

46. Xu, L., He, H., Du, Y., Zhang, S., Yu, D.G. and Liu, P., 2023. Electrosprayed core (cellulose acetate)–shell (polyvinylpyrrolidone) nanoparticles for smart acetaminophen delivery. *Pharmaceutics*, 15(9), p.2314. DOI: 10.3390/pharmaceutics15092314

47. Huang, H. and Dean, D., 2020. 3-D printed porous cellulose acetate tissue scaffolds for additive manufacturing. *Additive manufacturing*, 31, p.100927. DOI: 10.1016/j.addma.2019.100927

48. Abdullatif, K.G., Guirguis, M.N. and Moussa, R.R., 2020. Analyzing the structural properties of Fire Clay bricks after adding cigarette filters. DOI: 10.37394/232015.2020.16.69

49. Rahman, M.T., Mohajerani, A. and Giustozzi, F., 2020. Possible use of cigarette butt fiber modified bitumen in stone mastic asphalt. *Construction and Building Materials*, 263, p.120134. DOI: 10.1016/j.conbuildmat.2020.120134

50. Gómez Escobar, V., Moreno González, C., Arévalo Caballero, M.J. and Gata Jaramillo, A.M., 2021. Initial conditioning of used cigarette filters for their recycling as acoustical absorber materials. *Materials*, 14(15), p.4161. DOI: 10.3390/MA14154161

51. de Lima Vielmo, A.S., Rodrigues, A.B., da Rosa, E.V., Domingos, D.G., Schallemberger, J.B. and Nagel-Hassemer, M.E., 2022. Nonwoven from cigarette butt applied in pre-treatment of surface water. *Anuário do Instituto de Geociências*, 45, pp.1-13. DOI: 10.11137/1982-3908_2022_45_44159

52. Polarz, S., Smarsly, B. and Schattka, J.H., 2002. Hierachical porous carbon structures from cellulose acetate fibers. *Chemistry of materials*, 14(7), pp.2940-2945. DOI: 10.1021/cm011271r

53. Masoudi Soltani, S., Yazdi, S.K. and Hosseini, S., 2014. Effects of pyrolysis conditions on the porous structure construction of mesoporous charred carbon from

used cigarette filters. *Applied Nanoscience*, 4, pp.551-569. DOI: 10.1007/s13204-013-0230-0

54.  Janković, B., Kojić, M., Milošević, M., Rosić, M., Waisi, H., Božilović, B., Manić, N. and Dodevski, V., 2023. Upcycling of the used cigarette butt filters through pyrolysis process: Detailed kinetic mechanism with bio-char characterization. *Polymers*, 15(14), p.3054. DOI: 10.3390/polym15143054

55.  Mahto, A., Halakarni, M.A., Maraddi, A., D'Souza, G., Samage, A.A., Thummar, U.G., Mondal, D. and Nataraj, S.K., 2022. Upcycling cellulose acetate from discarded cigarette butts: Conversion of contaminated microfibers into loose-nanofiltration membranes for selective separation. *Desalination*, 535, p.115807. DOI: 10.1016/j.desal.2022.115807

56.  Gohain, M.B., Karki, S. and Ingole, P.G., 2024. Cellulose acetate, a source from discarded cigarette butts for the development of mixed matrix loose nanofiltration membranes for selective separation. *International Journal of Biological Macromolecules*, p.132197. DOI: 10.1016/j.ijbiomac.2024.132197

57.  Laurenza, A.G., Losito, O., Casiello, M., Fusco, C., Nacci, A., Pantone, V. and D'Accolti, L., 2021. Valorization of cigarette butts for synthesis of levulinic acid as top value-added chemicals. *Scientific* reports, 11(1), p.15775. DOI: 10.1038/s41598-021-95361-4

58.  Ogundare, S.A., Moodley, V. and Van Zyl, W.E., 2017. Nanocrystalline cellulose isolated from discarded cigarette filters. *Carbohydrate polymers*, 175, pp.273-281. DOI: 10.1016/j.carbpol.2017.08.008

59.  Benavente, M.J., Caballero, M.J.A., Silvero, G., López-Coca, I. and Escobar, V.G., 2019, February. Cellulose acetate recovery from cigarette butts. In *Proceedings* (Vol. 2, No. 20). MDPI. DOI: 10.3390/proceedings2201447

60.  De Fenzo, A., Giordano, M. and Sansone, L., 2020. A clean process for obtaining high-quality cellulose acetate from cigarette butts. *Materials*, 13(21), p.4710. DOI: 10.3390/ma13214710

61. Arroyo, F.D., Castro-Guerrero, C.F. and León-Silva, U., 2020. Thin films of cellulose acetate nanofibers from cigarette butt waste. *Progress in Rubber, Plastics and Recycling Technology*, 36(1), pp.3-17. DOI: 10.1177/1477760619895024

62. De Cesaris, M.G., Felli, N., Antonelli, L., Francolini, I., D'Orazio, G., Dal Bosco, C. and Gentili, A., 2024. Recovery of cellulose acetate bioplastic from cigarette butts: realization of a sustainable sorbent for water remediation. *Science of The Total Environment*, 929, p.172677. DOI: 10.1016/j.scitotenv.2024.172677

63. Ramesh, C., Tulasi, B.R., Raju, M., Thakur, N. and Dufossé, L., 2021. Marine natural products from tunicates and their associated microbes. *Marine drugs*, 19(6), p.308. DOI: 10.3390/md19060308

64. Wawrzyniak, M.K., Serrato, L.A.M. and Blanchoud, S., 2021. Artificial seawater based long-term culture of colonial ascidians. *Developmental Biology*, 480, pp.91-104. DOI: 10.1016/j.ydbio.2021.08.005

65. Järnegren, J., Gulliksen, B., Husa, V., Malmstrøm, M., Oug, E., Berg, P.R., Bryn, A., Geange, S.R., Hindar, K., Hole, L.R. and Kausrud, K.L., 2023. Assessment of risk and risk-reducing measures related to the introduction and dispersal of the invasive alien carpet tunicate Didemnum vexillum in Norway. Available at: https://hdl.handle.net/11250/3102529

66. Ramsay, A., Davidson, J., Landry, T. and Arsenault, G., 2008. Process of invasiveness among exotic tunicates in Prince Edward Island, Canada. *Biological Invasions*, 10, pp.1311-1316. DOI: 10.1007/s10530-007-9205-y

67. Clavelina oblonga. (2020) 'Description of Clavelina oblonga. Available at: https://www.european-marine-life.org/32/clavelina-oblonga.php (Accessed: 15 October 2024).

68. De Souza Lima, M.M., Wong, J.T., Paillet, M., Borsali, R. and Pecora, R., 2003. Translational and rotational dynamics of rodlike cellulose whiskers. *Langmuir*, 19(1), pp.24-29. DOI: 10.1021/la020475z

69. Song, G., Delroisse, J., Schoenaers, D., Kim, H., Nguyen, T.C., Horbelt, N., Leclère, P., Hwang, D.S., Harrington, M.J. and Flammang, P., 2020. Structure and composition of the tunic in the sea pineapple Halocynthia roretzi: A

complex cellulosic composite biomaterial. *Acta Biomaterialia*, 111, pp.290-301. DOI: 10.1016/j.actbio.2020.04.038

70.  Kimura, S. and Itoh, T., 1996. New cellulose synthesizing complexes (terminal complexes) involved in animal cellulose biosynthesis in the tunicate Metandrocarpa uedai. *Protoplasma*, 194, pp.151-163. DOI: 10.1007/BF01882023

71.  Ordóñez, V., Pascual, M., Fernández-Tejedor, M. and Turon, X., 2016. When invasion biology meets taxonomy: Clavelina oblonga (Ascidiacea) is an old invader in the Mediterranean Sea. *Biological Invasions*, 18, pp.1203-1215. DOI: 10.1007/s10530-016-1062-0

72.  Majnarić, N., Pavičić-Hamer, D., Jaklin, A. and Hamer, B., 2022. Susceptibility of invasive tunicates Clavelina oblonga to reduced seawater salinities. *Aquaculture reports*, *27*, p.101402. DOI: 10.1016/j.aqrep.2022.101402

73.  Matthysse, A.G., Deschet, K., Williams, M., Marry, M., White, A.R. and Smith, W.C., 2004. A functional cellulose synthase from ascidian epidermis. *Proceedings of the National Academy of Sciences*, 101(4), pp.986-991. DOI: 10.1073/pnas.030362310

74.  Gao, P., Khong, H.Y., Mao, W., Chen, X., Bao, L., Wen, X. and Xu, Y., 2023. Tunicates as sources of high-quality nutrients and bioactive compounds for food/feed and pharmaceutical applications: a review. *Foods*, 12(19), p.3684. DOI: 10.3390/foods12193684

75.  Lv, X., Han, J., Liu, M., Yu, H., Liu, K., Yang, Y., Sun, Y., Pan, P., Liang, Z., Chang, L. and Chen, J., 2023. Overview of preparation, modification, and application of tunicate-derived nanocellulose. *Chemical Engineering Journal*, 452, p.139439. DOI: 10.1016/j.cej.2022.139439

76.  Zhang, D., Zhang, Q., Gao, X. and Piao, G., 2013. A nanocellulose polypyrrole composite based on tunicate cellulose. *International Journal of Polymer Science*, 2013(1), p.175609. DOI: 10.1155/2013/175609

77.  Huang, Y., Zhan, H., Li, D., Tian, H. and Chang, C., 2019. Tunicate cellulose nanocrystals modified commercial filter paper for efficient oil/water separation. *Journal of Membrane Science*, 591, p.117362. DOI: 10.1016/j.memsci.2019.117362

78.  Huang, D., Li, D., Mo, K., Xu, R., Huang, Y., Cui, Y., Zhang, Q. and Chang, C., 2021. Top-down fabrication of biodegradable multilayer tunicate cellulose films with controlled mechanical properties. *Cellulose*, 28, pp.10415-10424. DOI: 10.1016/j.memsci.2019.117362

79.  Kjesbu, J.S., Zaytseva-Zotova, D., Sämfors, S., Gatenholm, P., Troedsson, C., Thompson, E.M. and Strand, B.L., 2022. Alginate and tunicate nanocellulose composite microbeads–Preparation, characterization and cell encapsulation. *Carbohydrate Polymers*, 286, p.119284. DOI: 10.1016/j.carbpol.2022.119284

80.  Cui, Y., Li, D., Gong, C. and Chang, C., 2021. Bioinspired shape memory hydrogel artificial muscles driven by solvents. *ACS nano*, 15(8), pp.13712-13720. DOI: 10.1021/acsnano.1c05019

81.  Yuan, H., Nishiyama, Y., Wada, M. and Kuga, S., 2006. Surface acylation of cellulose whiskers by drying aqueous emulsion. *Biomacromolecules*, *7*(3), pp.696-700. DOI: 10.1021/bm050828j

82.  Shanmuganathan, K., Capadona, J.R., Rowan, S.J. and Weder, C., 2010. Stimuli-responsive mechanically adaptive polymer nanocomposites. *ACS applied materials & interfaces*, 2(1), pp.165-174. DOI: 10.1021/am9006337

83.  Zhang, T., Cheng, Q., Ye, D. and Chang, C., 2017. Tunicate cellulose nanocrystals reinforced nanocomposite hydrogels comprised by hybrid cross-linked networks. *Carbohydrate polymers*, 169, pp.139-148. DOI: 10.1016/j.carbpol.2017.04.007

84.  Darpentigny, C., Molina-Boisseau, S., Nonglaton, G., Bras, J. and Jean, B., 2020. Ice-templated freeze-dried cryogels from tunicate cellulose nanocrystals with high specific surface area and anisotropic morphological and mechanical properties. *Cellulose*, 27, pp.233-247. DOI: 10.1007/s10570-019-02772-8

85.  Dunlop, M.J., Clemons, C., Reiner, R., Sabo, R., Agarwal, U.P., Bissessur, R., Sojoudiasli, H., Carreau, P.J. and Acharya, B., 2020. Towards the scalable isolation of cellulose nanocrystals from tunicates. *Scientific reports*, 10(1), p.19090. DOI: 10.1038/s41598-020-76144-9

86.  Zhao, Y. and Li, J., 2014. Excellent chemical and material cellulose from tunicates: diversity in cellulose production yield and chemical and morphological structures from different tunicate species. *Cellulose*, 21, pp.3427-3441. DOI: 10.1007/s10570-014-0348-6

87.  Dunlop, M.J., Acharya, B. and Bissessur, R., 2018. Isolation of nanocrystalline cellulose from tunicates. *Journal of Environmental Chemical Engineering*, 6(4), pp.4408-4412. DOI: 10.1016/j.jece.2018.06.056

88.  Crouzet, C., et al., 2017. Hydrothermal steel slag valorization—Part II: Hydrogen and nano-magnetite production. *Frontiers in Earth Science*, *5*, p.86. DOI 10.3389/feart.2017.00086

89.  Thomas, C., Rosales, J., Polanco, J. A., & Agrela, F., 2019. Steel slags. In: New Trends in Eco-efficient and Recycled Concrete, pp. 169-190. DOI: 10.1016/B978-0-08-102480-5.00007-5

90.  Nunes, V.A.,  et al., 2022. Influence of Activation Parameters on the Mechanical and Microstructure Properties of an Alkali-Activated BOF Steel Slag. *Applied Sciences*, 12(23), pp.12437. DOI: 10.3390/app122312437

91.  Navarro, C., Díaz, M., & Villa-García, M. A., 2010. Physico-chemical characterization of steel slag. Study of its behavior under simulated environmental conditions. *Environmental science & technology*, 44(14), pp. 5383-5388. DOI: 10.1021/es100690b

92.  Galván-Ruiz, M., et al., 2009. Characterization of calcium carbonate, calcium oxide, and calcium hydroxide as starting point to the improvement of lime for their use in construction. *Journal of Materials in civil Engineering*, 21(11), pp.694-698. DOI: 10.1061/(ASCE)0899-1561(2009)21:11(694).

93.  Phung, Q. T., Maes, N., and Seetharam, S., 2019. Pitfalls in the use and interpretation of TGA and MIP techniques for Ca-leached cementitious materials. *Materials & Design*, 182, pp.108041. DOI: 10.1016/j.matdes.2019.108041

94.  Xu, B., Yi, Y., 2022. Treatment of ladle furnace slag by carbonation: Carbon dioxide sequestration, heavy metal immobilization, and strength enhancement. *Chemosphere*, 287, pp. 132274. DOI: j.chemSphere.2021.132274

95.  Santos, A., et al., 2009. Larnite powders and larnite/silica aerogel composites as effective agents for $CO_2$ sequestration by carbonation. *Journal of hazardous materials*, 168(2-3), pp.1397-1403. DOI: 10.1016/j.jhazmat.2009.03.026

96.  Sulimai, N. H., et al., 2021. Synthesis of nanostructured calcite thin film by additive-free carbonation reaction via thermal chemical vapor deposition method. *Journal of Materials Science: Materials in Electronics*, 32(3), pp. 3072-3082. DOI: 10.1007/s10854-020-05057-0

97.  Qi, F. et al., 2021. Effect of calcium to silica ratio on the synthesis of calcium silicate hydrate in high alkaline desilication solution. *Journal of the American Ceramic Society*, 104(1), pp.535-547. DOI:10.1111/jace.17440

98.  Dang, T. M. D., Le, T. T. T., Fribourg-Blanc, E., & Dang, M. C., 2011. Synthesis and optical properties of copper nanoparticles prepared by a chemical reduction method. *Advances in Natural Sciences: Nanoscience and Nanotechnology*, 2(1), pp. 015009. DOI:10.1088/2043-6262/2/1/015009

99.  Liu, Q. M., et al., 2012. Preparation of Cu nanoparticles with NaBH4 by aqueous reduction method. *Transactions of Nonferrous Metals Society of China*, 22(1), pp.117-123. DOI:10.1016/S1003-6326(11)61149-7

100. Travis, A. S., 2007. Manufacture and uses of the anilines: a vast array of processes and products. The chemistry of Anilines, pp.715-782. DOI:10.1002/9780470871737.ch13

101. Song, J., et al., 2018. Review on selective hydrogenation of nitroarene by catalytic, photocatalytic and electrocatalytic reactions. *Applied Catalysis B: Environmental*, 227, pp.386-408. DOI: 10.1016/j.apcatb.2018.01.052

102. Kadam, H. K., and Tilve, S. G., 2015. Advancement in methodologies for reduction of nitroarenes. RSC advances, 5(101), pp.83391-83407. DOI:10.1039/C5RA10076C

103. Zhang, K., et al., 2019. Recent advances in the nanocatalyst-assisted $NaBH_4$ reduction of nitroaromatics in water. *ACS omega*, 4(1), pp. 483-495. DOI: 10.1021/acsomega.8b03051

104.Andrade, M. A., and Martins, L. M., 2020. Supported palladium nanocatalysts: recent findings in hydrogenation reactions. *Processes*, 8(9), pp.1172. DOI:10.3390/pr8091172

105.Dell'Anna, M. M., et al., 2014. Polymer supported palladium nanocrystals as efficient and recyclable catalyst for the reduction of nitroarenes to anilines under mild conditions in water. *Journal of Molecular Catalysis A: Chemical*, 395, pp. 307-314. DOI: 10.1016/j.molcata.2014.08.033

106.Dell'Anna, M. M., Gallo, V., Mastrorilli, P., and Romanazzi, G., 2010. A recyclable nanoparticle-supported rhodium catalyst for hydrogenation reactions. *Molecules*, 15(5), pp.3311-3318. DOI: 10.3390/molecules15053311

107.Wei, Y., et al., 2014. Highly Efficient Rhodium-Catalyzed Transfer Hydrogenation of Nitroarenes into Amines and Formanilides. *Synlett*, 25(09), pp.1295-1298. DOI: 10.1055/s-0033-1341250

108.Formenti, D., Ferretti, F., Scharnagl, F. K., and Beller, M., 2018. Reduction of nitro compounds using 3d-non-noble metal catalysts. *Chemical reviews*, 119(4), pp.2611-2680. DOI: 10.1021/acs.chemrev.8b00547

109.Jagadeesh, R. V., et al., 2011. Efficient and highly selective iron-catalyzed reduction of nitroarenes. Chemical Communications, 47(39), pp.10972-10974. DOI:10.1039/C1CC13728J

110.Romanazzi, G., et al., 2018. Polymer supported Nickel nanoparticles as recyclable catalyst for the reduction of nitroarenes to anilines in aqueous medium. *Molecular Catalysis*, 446, pp. 31-38. DOI:10.1016/j.mcat.2017.12.015

111.Petrelli, V., et al., 2023. N-doped resin supported cobalt nanoparticles for the catalytic reduction of nitroarenes to corresponding anilines in aqueous medium. *Molecular Catalysis*, 544, pp.113050. DOI:10.1016/j.mcat.2023.113050

112.Kottappara, R., Pillai, S. C., and Vijayan, B. K., 2020. Copper-based nanocatalysts for nitroarene reduction-A review of recent advances*. Inorganic Chemistry Communications*, 121, pp.108181. DOI: 10.1016/j.inoche.2020.108181

113.Tang, J., et al., 2023. Highly Efficient Catalytic Reduction of Nitrobenzene Using Cu@C Based on a Novel Cu–MOF Precursor. *Catalysts*, 13(6), pp. 956. DOI: 10.3390/catal13060956

114.Moran, M. J., et al., 2020. Tuneable copper catalysed transfer hydrogenation of nitrobenzenes to aniline or azo derivatives. *Advanced Synthesis & Catalysis*, 362(13), pp.2689-2700. DOI: 10.1002/adsc.202000127

115.Dang, T. M. D., Le, T. T. T., Fribourg-Blanc, E., and Dang, M. C., 2011. Synthesis and optical properties of copper nanoparticles prepared by a chemical reduction method. *Advances in Natural Sciences: Nanoscience and Nanotechnology*, 2(1), pp.015009. DOI: 10.1088/2043-6262/2/1/015009

116.Markin, A. V., and Markina, N. E., 2019. Experimenting with plasmonic copper nanoparticles to demonstrate color changes and reactivity at the nanoscale. *Journal of Chemical Education*, 96(7), pp.1438-1442. DOI: 10.1021/acs.jchemed.8b01050.

117.Hass, M., and Sutherland, G. B. B. M., 1956. The infra-red spectrum and crystal structure of gypsum. *Proceedings of the Royal Society of London. Series A. Mathematical and Physical Sciences*, 236(1207), pp. 427-445.DOI:10.1098/rspa.1956.0146

118.Guan, Q., et al., 2017. A facile method of transforming FGD gypsum to alpha-CaSO4 ·0.5 $H_2O$ whiskers with cetyltrimethylammonium bromide (CTAB) and KCl in glycerol-water solution. *Scientific reports*, 7. DOI: 10.1038/s41598-017-07548-3

119.Nayak, R., et al., 2020. Fabrication of CuO nanoparticle: An efficient catalyst utilized for sensing and degradation of phenol. *Journal of Materials Research and Technology*, 9(5), pp. 11045-11059. DOI: 10.1016/j.jmrt.2020.07.100

120.Paul, C. A., Kumar, E. R., Suryakanth, J., and Abd El-Rehim, A. F., 2023. Analysis and characterization of structural, morphological, thermal properties and colloidal stability of CuO nanoparticles for various natural fuels. *Ceramics International*, 49(19), pp.31193-31209. DOI: 10.1016/j.ceramint.2023.07.065

121.Wang, F. P., et al. 2021. A review of modified steel slag application in catalytic pyrolysis, organic degradation, electrocatalysis, photocatalysis, transesterification and carbon capture and storage. *Applied Sciences*, 11(10), pp.4539. DOI:10.3390/app11104539

122.Zehfuß, J., and Sander, L., 2021. Gypsum plasterboards under natural fire— Experimental investigations of thermal properties. *Civil engineering design*, 3(3), pp.62-72. DOI: 10.1002/cend.202100002

123.Krejsová, J., et al., 2024. New insight into the phase changes of gypsum. *Materials and Structures*, 57(5), pp.128. DOI: 10.1617/s11527-024-02404-z.

124.Carnes, C. L., Stipp, J., Klabunde, K. J., and Bonevich, J., 2002. Synthesis, characterization, and adsorption studies of nanocrystalline copper oxide and nickel oxide. *Langmuir*, 18(4), pp.1352-1359. DOI: 10.1021/la010701p

125.Khadivi, A. H., Vahdati, K. J., and Haddad, S. M., 2015. Facile synthesis of copper oxide nanoparticles using copper hydroxide by mechanochemical process. pp. 37-44. DOI: 10.7508/jufgnsm.2015.01.006

126.Yu, J. C., et al., 2004. Synthesis and characterization of porous magnesium hydroxide and oxide nanoplates. *The Journal of Physical Chemistry B*, 108(1), pp. 64-70. DOI: 10.1021/jp035340w

127.Suárez-Campos, G., et al., 2019. Controlled synthesis of Mg (OH) 2 thin films by chemical solution deposition and their thermal transformation to MgO thin films. *Ceramics International*, 45(8), pp. 10356-10363. DOI: 10.1016/j.ceramint.2019.02.093.

128.Wang, D., Deraedt, C., Ruiz, J., and Astruc, D., 2015. Sodium hydroxide-catalyzed transfer hydrogenation of carbonyl compounds and nitroarenes using ethanol or isopropanol as both solvent and hydrogen donor. *Journal of Molecular Catalysis A: Chemical*, 400, pp.14-21. DOI: doi.org/10.1016/j.molcata.2015.01.024

129.Sonavane, S. U., et al., 2007. Chemoselective transfer hydrogenation reactions over nanosized $\gamma$-$Fe_2O_3$ catalyst prepared by novel combustion route. *Catalysis Communications*, 8(11), pp.1803-1806. DOI: 10.1016/j.catcom.2007.01.037

130.Sharma, A., and Sharma, V., 2023. Forensic analysis of cigarette filter using non-destructive ATR-FTIR spectroscopy and chemometric methods. *Forensic Chemistry*, 32, pp.100465. DOI: 10.1016/j.forc.2023.100465

131. Barud, H. S.,et al., 2008. Thermal behavior of cellulose acetate produced from homogeneous acetylation of bacterial cellulose. *Thermochimica acta*, 471(1-2), pp.61-69. DOI: 10.1016/j.tca.2008.02.009

132. Božilović, B., et al., 2024. Thermo-chemical conversion of cigarette butt filters waste through pyrolysis process using thermal analysis techniques. *Thermal Science*, 28(1 Part B), pp. 513-527. DOI: 10.2298/TSCI230520153B

133. Afroz, F., Mahmud, R. U., and Islam, R., 2023. Green approach to recover the cellulose acetate fiber from used cigarette butts, and characterize the filter fiber. *AATCC Journal of Research*, 10(5), pp. 311-320. DOI:10.1177/24723444231175209

134. Li, A., and Yalkowsky, S. H., 1994. Solubility of organic solutes in ethanol/water mixtures. *Journal of pharmaceutical sciences*, 83(12), pp.1735-1740. DOI: 10.1002/jps.2600831217

135. Forfang, K., et al. 2017. FTIR spectroscopy for evaluation and monitoring of lipid extraction efficiency for oleaginous fungi. *PloS one*, 12(1), pp. e0170611. DOI: 10.1371/journal.pone.0170611

136. Shurvell, H. F., 2006. Spectra–structure correlations in the mid-and far-infrared. *Handbook of vibrational spectroscopy*. DOI: 10.1002/0470027320.s4101

137. Pancake, S.J., Karnovsky, M.L., 1971. The isolation and characterization of a mucopolysaccharide secreted by the snail, Otella lactea. *J. Biol. Chem.* 246, pp. 253–262

138. Giordano, M., et al., 2001. Fourier transform infrared spectroscopy as a novel tool to investigate changes in intracellular macromolecular pools in the marine micro-alga Chaetoceros muellerii (Bacillariophyceae). *Journal of phycology*, 37(2), pp.271-279. DOI: 10.1046/j.1529-8817.2001.037002271.x

139. Rinaudo, M., 2006. Chitin and chitosan: Properties and applications. *Progress in polymer science*, 31(7), pp.603-632. DOI: 10.1016/j.progpolymsci.2006.06.001

140. Nakashima, K., Sugiyama, J., and Satoh, N., 2008. A spectroscopic assessment of cellulose and the molecular mechanisms of cellulose biosynthesis in the ascidian Ciona intestinalis. *Marine genomics*, 1(1), pp.9-14. DOI: 10.1016/j.margen.2008.01.001

141. Zhao, Y., and Li, J., 2014. Excellent chemical and material cellulose from tunicates: diversity in cellulose production yield and chemical and morphological structures from different tunicate species. *Cellulose*, 21, pp.3427-3441.  DOI: 10.1007/s10570-014-0348-6

142. Stehfest, K., Toepel, J., and Wilhelm, C., 2005. The application of micro-FTIR spectroscopy to analyze nutrient stress-related changes in biomass composition of phytoplankton algae. *Plant Physiology and biochemistry*, 43(7), pp.717-726. DOI: 10.1016/j.plaphy.2005.07.001

143. Chen, W. H., Chu, Y. S., Liu, J. L., and Chang, J. S., 2018. Thermal degradation of carbohydrates, proteins and lipids in microalgae analyzed by evolutionary computation. *Energy Conversion and Management*, 160, pp.209-219. DOI: 10.1016/j.enconman.2018.01.036

144. Rizzo, A. M., et al., 2013. Characterization of microalga Chlorella as a fuel and its thermogravimetric behavior. *Applied energy*, 102, pp. 24-31. DOI: 10.1016/j.apenergy.2012.08.039

145. Abbott, A. P., et al., 2003. Novel solvent properties of choline chloride/urea mixtures. *Chemical communications*, (1), pp.70-71. DOI: 10.1039/b210714g

146. Smith, E. L., Abbott, A. P., and Ryder, K. S., 2014. Deep eutectic solvents (DESs) and their applications. *Chemical reviews*, 114(21), pp.11060-11082. DOI: 10.1021/cr300162p

147. Zhu, Z., Lü, H., Zhang, M., and Yang, H., 2021. Deep eutectic solvents as non-traditionally multifunctional media for the desulfurization process of fuel oil. Physical *Chemistry Chemical Physics*, 23(2), pp.785-805. DOI: 10.1039/d0cp05153e

148. Elhamarnah, Y., Qiblawey, H., and Nasser, M., 2024. A review on deep eutectic solvents as the emerging class of green solvents for membrane fabrication and separations. *Journal of Molecular Liquids*, pp.124250. DOI: 10.1016/j.molliq.2024.124250

149. Hansen, B. B., et al., 2020. Deep eutectic solvents: A review of fundamentals and applications. *Chemical reviews*, 121(3), pp.1232-1285. DOI: 10.1021/acs.chemrev.0c00385

150. Ijardar, S. P., Singh, V., and Gardas, R. L., 2022. Revisiting the physicochemical properties and applications of deep eutectic solvents. *Molecules*, 27(4), pp.1368. DOI:10.3390/molecules27041368

151. Abbott, A. P., Capper, G., Davies, D. L., and Rasheed, R., 2004. Ionic liquids based upon metal halide/substituted quaternary ammonium salt mixtures. Inorganic chemistry, 43(11), pp.3447-3452. DOI:10.1021/ic049931s

152. Abbott, A. P., Capper, G., Davies, D. L., and Rasheed, R. K. 2004. Ionic liquid analogues formed from hydrated metal salts. *Chemistry–A European Journal*, 10(15), pp.3769-3774. DOI: 10.1002/chem.200400127

153. Tan, Y. T., Chua, A. S. M., and Ngoh, G. C., 2020. Deep eutectic solvent for lignocellulosic biomass fractionation and the subsequent conversion to bio-based products–A review. *Bioresource Technology*, 297, pp.122522. DOI: 10.1016/j.biortech.2019.122522

154. Abranches, D. O., et al., 2019. Phenolic hydrogen bond donors in the formation of non-ionic deep eutectic solvents: the quest for type V DES. *Chemical Communications*, 55(69), pp.10253-10256. DOI: 10.1039/C9CC04846D

155. Dai, Y., et al., 2013. Natural deep eutectic solvents as new potential media for green technology. *Analytica chimica acta*, 766, pp. 61-68. DOI: 10.1016/j.aca.2012.12.019

156. Colella, M., et al. Microwave-assisted treatment of waste wood biomass with deep eutectic solvents. *Macromolecular Symposia*. 404 (1), pp.2100284. DOI: 10.1002/masy.202100284

157. Topal, T., et al., 2024. Hydrophobic natural deep eutectic solvents for marine lipid extraction. *Journal of the American Oil Chemists' Society*, 101(3), pp.361-367. DOI: 10.1002/aocs.12757

158. Mandal, A., and Chakrabarty, D., 2011. Isolation of nanocellulose from waste sugarcane bagasse (SCB) and its characterization. *Carbohydrate polymers*, 86(3), pp.1291-1299. DOI: 10.1016/j.carbpol.2011.06.030

159. Curetti, N., et al., 2021. Thermal stability of calcium oxalates from $CO_2$ sequestration for storage purposes: an in-situ HT-XRPD and TGA combined study. *Minerals*, 12(1), pp.53. DOI: doi.org/10.3390/min12010053